Gravitation and Multimessenger Astrophysics

by

Imre Bartos

Submitted in partial fulfillment of the
requirements for the degree of

Doctor of Philosophy

in the Graduate School of Arts and Sciences

COLUMBIA UNIVERSITY

2012

Abstract

Gravitation and Multimessenger Astrophysics

by

Imre Bartos

Gravitational waves originate from the most violent cosmic events, which are often hidden from traditional means of observation. Starting with the first direct observation of gravitational waves in the coming years, astronomy will become richer with a new messenger that can help unravel many of the yet unanswered questions on various cosmic phenomena.

The ongoing construction of advanced gravitational wave observatories requires disruptive innovations in many aspects of detector technology in order to achieve the sensitivity that lets us reach cosmic events. We present the development of a component of this technology, the Advanced LIGO Optical Timing Distribution System. This technology aids the detection of relativistic phenomena through ensuring that time, at least for the observatories, is absolute.

Gravitational waves will be used to look into the depth of cosmic events and understand the engines behind the observed phenomena. As an example, we examine some of the plausible engines behind the creation of gamma ray bursts. We anticipate that, by reaching through shrouding blastwaves, efficiently discovering off-axis events, and observing the central engine at work, gravitational wave detectors will soon transform the study of gamma ray bursts. We discuss how the detection of gravitational waves could revolutionize our understanding of the progenitors of gamma ray bursts, as well as related phenomena such as the properties of neutron stars.

One of the most intriguing directions in utilizing gravitational waves is their combination with other cosmic messengers such as photons or neutrinos. We discuss the strategies and ongoing efforts in this direction. Further, we present the first observational constraints on joint sources of gravitational waves and high energy neutrinos, the latter of which is created in relativistic plasma outflows, e.g., in gamma ray burst progenitors.

High energy neutrinos may be created inside a relativistic outflow burrowing its way out of a massive star from the star's collapsed core. We demonstrate how the detection of high energy neutrinos can be used to extract important information about the supernova/gamma-ray burst progenitor structure. We show that, under favorable conditions, even a few neutrinos are sufficient to probe the progenitor structure, opening up new possibilities for the first detections, as well for progenitor population studies.

We present the science reach and method of an ongoing search for common sources of gravitational waves and high energy neutrinos using the initial LIGO/Virgo detectors and the partially completed IceCube detector. We also present results on the sensitivity of the search. We argue that such searches will open the window onto source populations whose electromagnetic emission is hardly detectable.

Contents

List of Figures

List of Tables

Acknowledgement

I am greatly indebted to my advisor, Szabolcs Márka, for his continuous help and guidance ever since we first met eight years ago. Not only had he shown me the way forward, but he also gave me the opportunity to, through his example, learn to appreciate sharing my experience with the next generation. I am grateful to my parents for teaching me, through their own example, to appreciate knowledge, curiosity and hard work, providing guidance along my journey. I am grateful to Zsuzsa Márka for her support in good and bad times, and for helping with the simple things in life that are the hardest to keep in order. I am grateful to Imre Jánosi for my first experiences with research, for helping me on my first steps towards becoming a scientist. I would like to thank Zsolt Bihary, Péter Gnädig, and Anna Részeg who guided my curiosity towards the sciences and physics. I am thankful to Péter Raffai with whom we shared the joy and the burden on our was towards understanding Nature throughout our academic life. I am grateful to Kristine Langhorn for her tremendous help with the manuscript. It is my pleasure to acknowledge the help of Daniel Sigg and Paul Schwinberg for their unwavering support during our joint work on the Advanced LIGO Timing System. I would like to thank Keita Kawabe, Michael Landry, Brian O'Reilly, Fred Raab, Keith Thorne, and many others at the LIGO observatories in Hanford, WA and Livingston, LA, for their tremendous help with letting me better understand the detectors through first hand experience. I would like to thank Laura Cadonati for her help during my first summer internship and my first encounter with LIGO. I am indebted to Chad Finley who has been cardinal in my involvement with IceCube and everything neutrino. I am grateful to Sergey Klimenko for his help with obtaining and better understanding gravitational wave triggers. I am also thankful to the CWb team, including Marco Drago, Giovanni Prodi, Virginia Re, Francesco Salemi, and Gabriele Vedovato, for their help with getting from raw data to statistically quantifiable results. I would like to express my gratitude towards the GW+HEN

Working Group who transformed the original idea of GW+HEN multimessenger searches into reality. Finally, I would like to thank the LIGO, Virgo, and IceCube collaborations for constructing such cutting edge observatories that let us open new windows onto the universe in a friendly and social work environment.

"The truth is often hidden below the surface.
One has to go deep below the skin to find it."
– Carl von Rokitansky

Chapter 1

Introduction

Comprehending Nature often necessitates learning about phenomena at their extremes. Exploring our environment in the greatest or smallest scales may teach us about the middle as well. Astrophysics, in many senses, is set to take on this journey to the extremes: to the farthest, most energetic, most violent phenomena in the Universe.

We can learn about extreme phenomena in galaxies far, far away via cosmic messengers that travel through vast distances to tell us their tales of origin. Gravitational waves are special kinds of such messengers: They are produced in the very core of violent cosmic events, at the highest densities and most volatile motion of matter. These cores are often engines driving hosts of other mechanisms that in turn will be observable via other messengers.

Understanding the connection between the engine behind these violent events and the set of processes they initiate is one of the most intriguing challenges in astrophysics. To achieve this goal one needs to combine the information available through different cosmic messengers that convey different aspects of the story.

Multimessenger astrophysics with gravitational waves aims to reach towards this goal. Beyond combining the available information channels, it also utilizes the different messengers to reach farther into space by increasing the distinction between the signal from an astrophysical source and the unavoidable noise that could obscure our view. Such additional information can be crucial, especially since the detection of gravitational waves is complicated by gravitation's extremely weak interaction with matter. The electromagnetic force is $\sim 10^{20}\times$ stronger than gravitation. On the other hand, this weak interaction is responsible for letting gravitational waves escape from the densest environments where they are created, without being sidetracked by matter.

To observe gravitational waves from large distances requires the construction of ever more sophisticated detectors that can sense the minute ripples in spacetime, with sensitivities beyond our imagination. For typical sources of interest, one needs to detect distortions that are 1000-times smaller than the tiniest atomic nuclei. Such a futuristic goal has been achieved through a series of scientific and engineering breakthroughs, leading to the construction of interferometric gravitational wave detectors, such as the Laser Interferometer Gravitational-wave Observatory (LIGO).

We are advancing towards the first direct detection of gravitational waves through developing advanced interferometers that can reach out to the cosmic phenomena producing gravitational waves. We contributed to the development and construction of advanced interferometers that hold the promise of first detection. A part of this work will be presented in this dissertation.

Reaching farther in our search for cosmic phenomena requires not only the advance of interferometer technology, but also the sophisticated use of information from gravitational-wave and other detectors. In order to present the progress in such use of information, we outline the different directions within the gravitational-wave community. We discuss different astrophysical messengers, search techniques, and recent searches.

The present dissertation describes a novel multimessenger search technique that was developed to combine information from gravitational waves and high energy neutrinos, as well as the anticipated direction of cosmic events of interest based on the local distribution of galaxies. The presented technique sets a new direction in multimessenger searches, where none of the combined messengers is, by itself, certain evidence of a cosmic event. We further present the first observational constraints on common sources of gravitational waves and high energy neutrinos based on existing observational results, as well as projected constraints from advanced detectors.

One of the most enigmatic phenomena in the distant universe are gamma ray bursts: short, catastrophic events emitting copious amounts of very energetic, narrowly beamed photons. In the dissertation we review plausible mechanisms that can drive gamma ray bursts, aiming to explore the gravitational wave signature of such mechanisms. We further explore how such signatures can be used to gain understanding of extreme physical phenomena that are otherwise virtually impossible to observe.

To better understand the information encoded in various cosmic messengers, we examine some of the information carried in high energy neutrinos about their source. We demonstrate how even a few neutrinos, under favorable conditions, can constrain the progenitor of the emission. This case is of special importance, as the expected flux of high energy neutrinos will likely be very low for most detected sources.

The dissertation is organized as follows. In Section 1.1 we give a brief description of gravitational waves, their generation, and their detection, in order to facilitate our discussion on gravitational wave observatories and searches.

In Section 1.2, we review possible gravitational wave emission mechanisms from gamma ray bursts. While many other astrophysical phenomena can result in the emission of gravitational waves, gamma ray bursts are probably the most intriguing targets of multimessenger astronomy with gravitational waves, especially in the frequency range accessible with earth-based interferometers. Gamma ray bursts are also interesting targets because there are many unanswered questions about their central engine, which is responsible for driving the burst. These central engines can be directly probed via gravitational waves. Beyond the presentation of plausible scenarios of gravitational wave emission, we further discuss some of the various physical phenomena that could be better understood by the detection of gravitational waves from gamma ray bursts.

In Section 1.3 we present some of the most important elements of gravitational wave interferometry. We briefly introduce the LIGO observatory, and some of the recent developments towards advanced detectors.

In Section 1.4 we discuss potential common sources of gravitational waves and high energy neutrinos.

Section 1.5 describes search strategies for gravitational wave sources, with special emphasis on utilizing other astrophysical messengers in aiding the search. We discuss different messengers that are being used in multimessenger searches with gravitational waves, and present a short outline of the targeted astrophysical sources of interest. We further outline ongoing and past searches with respect to the different strategies and messengers.

In Chapter 2 we introduce the Advanced LIGO Optical Timing Diagnostic System, also discussing the role of timing information from the perspective of astrophysical measurements and data analysis. In general, upon the detection of gravitational waves, the (astro-)physical results should not be limited by the precision of timing. The Advanced LIGO Timing System is designed to provide UTC-synchronized timing information for the Advanced LIGO detectors that satisfies the above criterion. We further demonstrate the precision and robustness of the Timing System through testing results.

In Chapter 3 we derive a conservative coincidence time window for the two messengers from gamma ray bursts. Further, we present observational constraints on their population for current measurements, and projected constraints achievable with advanced observatories in the near future.

In Chapter 4 we examine the information encoded in observed high energy neutrinos about their sources. We demonstrate that important information can be recovered, under favorable conditions, even with a few observed neutrinos.

In Chapter 5 we present a search method, and preliminary result, for common sources of gravitational waves and high energy neutrinos. The search for common sources of these two messengers presents a new direction in gravitational wave astronomy, in which one combines different messengers which by themselves would not be sufficient to discover a cosmic event.

Finally, we shortly summarize our discussion in the Conclusion.

1.1 Gravitational Radiation

We start our discussion in this dissertation by introducing gravitational radiation. We briefly discuss its interaction with matter, which makes gravitational radiation observable, as well as its generation. Finally, we note that gravitational radiation has been indirectly observed. Below we use the works of Einstein & Rosen [15], Landau & Lifshitz [16], Misner et al. [17] and Hraskó [18] in our discussion.

1.1.1 Ripples in spacetime

According to Einstein's General Theory of Relativity [19], gravitation is a consequence of the curvature of space and time (or *spacetime*). Since information cannot propagate faster than the speed of light [20], a sudden, local change in the curvature will also propagate at a finite speed. This finite propagation speed of the gravitational interaction necessitates the existence of waves in the fabric of spacetime. We refer to such waves as *gravitational waves* [21, 22].

The existence of gravitational waves was predicted by Einstein soon after the completion of the General Theory of Relativity. We start with the Einstein field equations [15]:

$$R_{\mu\nu} - \frac{1}{2} g_{\mu\nu} R = \frac{8\pi G}{c^4} T_{\mu\nu}, \tag{1.1}$$

where $R_{\mu\nu}$ is the Ricci curvature tensor, $g_{\mu\nu}$ is the metric tensor, $R = g^{\mu\nu} R_{\mu\nu}$ is the scalar curvature, $T_{\mu\nu}$ is the stress-energy tensor, and c and G are the speed of light and Newton's gravitational constant, respectively. We adopted Einstein's summation convention. Here and below, Greek indices will refer to four-coordinates, while Latin indices will denote spatial coordinates only. We consider a weak gravitational field that will represent a small perturbation in the spacetime metric. We can write the metric tensor in the form

$$g_{\mu\nu} = \eta_{\mu\nu} + h_{\mu\nu}, \tag{1.2}$$

where $\eta_{\mu\nu}$ is the Minkowski tensor of flat spacetime

$$\eta_{ik} = \delta_{ik}, \;\; \eta_{i0} = 0, \;\; \eta_{00} = -1, \tag{1.3}$$

and $h_{\mu\nu}$ is a small perturbation term. In the linear approximation, in which we consider $h_{\mu\nu}$ only to first order, the Riemann tensor will assume the form

$$R_{\mu\nu} = \partial_\alpha \Gamma^\alpha_{\mu\nu} - \partial_\nu \Gamma^\alpha_{\mu\alpha} = \frac{1}{2} \left(\partial_\mu \partial_\alpha h^\alpha_\nu + \partial_\nu \partial_\alpha h^\alpha_\mu - \partial_\mu \partial_\nu h - \Box^2 h_{\mu\nu} \right), \tag{1.4}$$

where $\Box^2 = \partial_k \partial^k$ is the D'Alembertian operator, and $h = g^{\mu\nu} h_{\mu\nu}$. We introduce the transverse-traceless quantity

$$\overline{h}_{\mu\nu} = h_{\mu\nu} - \frac{1}{2}\eta_{\mu\nu}h \tag{1.5}$$

We can choose the coordinate system such that it satisfies the Lorentz gauge

$$\partial^{\mu}\overline{h}_{\mu\nu} = 0. \tag{1.6}$$

With such choice, expressing Eq. 1.4 with $\overline{h}_{\mu\nu}$, one arrives at the simple form

$$\Box^2\overline{h}_{\mu\nu} = -\frac{16\pi G}{c^4}T_{\mu\nu}. \tag{1.7}$$

If no matter is present, then $T_{\mu\nu} = 0$ and $\overline{h}_{\mu\nu}$ satisfies the relativistic wave equation in vacuum. For the vacuum solutions of Eq. 1.7, one can utilize the additional gauge freedom[1] in $\overline{h}_{\mu\nu}$ to reduce it to transverse-traceless (TT) form, in which

$$\overline{h} = h = 0. \tag{1.11}$$

In this gauge $h_{\mu\nu}$ also satisfies the vacuum wave equation:

$$\Box h_{\mu\nu} = 0. \tag{1.12}$$

---

[1] Given the Lorentz gauge, $\overline{h}_{\mu\nu}$ is ambiguous to the extent of an infinitesimal coordinate transformation [17]

$$x^{\mu} \to \xi_{\mu} + \xi^{\mu} \tag{1.8}$$

for which

$$\Box\xi^{\mu} = 0. \tag{1.9}$$

For this transformation $\overline{h}_{\mu\nu}$ changes as

$$\overline{h}_{\mu\nu} \to \overline{h}_{\mu\nu} - \partial_{\mu}\xi_{\nu} - \partial_{\nu}\xi_{\mu} + \eta_{\mu\nu}\partial_{\alpha}\xi^{\alpha} \tag{1.10}$$

The simplest solution of Eq. 1.12 is a monochromatic plane wave

$$h_{\mu\nu}(z,t) = \begin{pmatrix} 0 & 0 & 0 & 0 \\ 0 & -h_+ & h_\times & 0 \\ 0 & h_\times & h_+ & 0 \\ 0 & 0 & 0 & 0 \end{pmatrix} \sin(k_z z - \omega t),$$

where h_+ and $h_\times$ are the amplitudes of the two independent gravitational wave polarizations, ω and $k_z = \omega/c$ are the frequency and wave vector of the plane wave, respectively, and the wave's direction of propagation was chosen to align with the z coordinate axis.

1.1.2 Interaction of gravitational waves with matter

Here we examine the effect of a passing gravitational wave on test particles. We consider two test particles, A and B. Let us use A's proper reference frame in which A is at the spatial origin ($x_A^{\widehat{j}} = 0$) and B is at $x_B^{\widehat{j}}$. For a passing gravitational wave, the separation $x_B^{\widehat{j}} - x_A^{\widehat{j}} = x_B^{\widehat{j}}$ varies as [17]

$$\frac{d^2 x_B^{\widehat{j}}}{dt^2} = -R_{j0k0}\, x_B^{\widehat{j}} = \frac{1}{2}\frac{\partial^2 h_{jk}}{\partial t^2} x_B^{\widehat{j}} \tag{1.13}$$

where we used the transverse traceless gauge. This can be integrated to yield

$$x_B^{\widehat{j}} = x_{B(0)}^{\widehat{k}}(\delta_{jk} + \frac{1}{2}h_{jk}), \tag{1.14}$$

where $x_{B(0)}^{\widehat{k}}$ is the position of B when no gravitational wave is present.

It is useful to look at the phase shift of a plane wave of light during a round trip traveling from A to B and then back to A. If the wavelength of the gravitational wave is much greater than $|x_{B(0)}^{\widehat{k}}|$, then for the travel time we can approximate the gravitational wave to have constant h_+ and $h_\times$ polarization components. If the gravitational wave is traveling along the z axis and $x_{B(0)}^{\widehat{k}} = L\widehat{x}$ is along the x axis, then the phase shift experienced by the light beam will be

$$\phi_x = 2\frac{2\pi L}{\lambda}(1 - \frac{1}{2}h_+). \tag{1.15}$$

For a direction towards the y axis, the phase shift due to the same gravitational wave will be $\phi_y = -\phi_x$. The gravitational wave polarizations h_+ and $h_\times$ are therefore related to the relative change in the distances between test particles

$$\frac{\Delta L}{L} = \frac{1}{2} h_+ \tag{1.16}$$

Due to this simple geometrical analogy, the effect of gravitational waves on distances, as well as the polarization amplitudes themselves, are sometimes referred to as *strain*.

1.1.3 Generation of gravitational waves

In linear approximation, the generation of gravitational waves is connected to the stress-energy tensor $T_{\mu\nu}$ through Eq. 1.7. Integrating this equation over the volume where $T_{\mu\nu} \neq 0$, we obtain a retarded solution familiar from electromagnetism [18]:

$$\overline{h}_{\mu\nu}(\overrightarrow{x}, t) = -\frac{4G}{c^4 r} \int d^3x' \cdot T_{\mu\nu}\left(\overrightarrow{x}', t - |\overrightarrow{x} - \overrightarrow{x}'|\right), \tag{1.17}$$

where we considered the far-field case when the distance $r \equiv |\overrightarrow{x}|$ is much greater than the size of the source.

For the simple case of nearly Newtonian masses, gravitational radiation is similar to electromagnetic radiation (with $e^2 \rightarrow -m^2$), although there are quantitative differences due to gravitation being a spin-two (tensor) field. The striking difference, however, is that for gravity, dipole radiation vanishes because a closed system has zero gravitational dipole momentum. Similarly, gravitational magnetic dipole momentum is also zero due to the conservation of angular momentum. The smallest non-vanishing order is therefore gravitational quadrupole radiation. The power of gravitational quadrupole radiation is [17]

$$L_{\mathrm{GW}} = \frac{G}{5c^5} \langle \dddot{\text{Ɨ}}_{jk} \dddot{\text{Ɨ}}^{jk} \rangle, \tag{1.18}$$

$$\dddot{\text{Ɨ}}^{jk} \equiv \int \rho \left(x_j x_k - \frac{1}{3} \delta_{jk} r^2 \right) d^3x, \tag{1.19}$$

where ρ is matter density.

1.1.4 Indirect evidence for the existence of gravitational waves

While we are advancing towards their first direct detection, gravitational waves have already been indirectly detected. In 1974, Hulse & Taylor [23] discovered the pulsar PSR 1913+16 in a binary system, and detected that its pulsation period varies over the binary's period of $\sim 8\,\mathrm{h}$. Measuring this cycle (that is due to the binary's rotation) over a longer period, they could measure the slow drift in the rotation period, which is consistent with the expected angular momentum loss due to gravitational radiation. Other pulsar systems (e.g. [24]) also show agreement with the emission of gravitational waves as predicted by General Relativity.

1.2 Astrophysical Sources of Gravitational Waves

In the previous section, we introduced gravitational radiation. Here, we discuss some of the astrophysical phenomena that are sources of observable gravitational wave emission.

Gravitational waves (GWs) are detectable from sources with very large, changing quadrupole moment. As the interaction of GWs with matter is extremely weak, only the most energetic cosmic events can produce a GW signal that is strong enough to be observed with currently existing and planned detectors.

Various cosmic sources are interesting potential GW sources that may be observed in the near future, after the completion of advanced interferometers such as Advanced LIGO and Virgo. Such sources include black hole (BH) and neutron star (NS) binaries coalescences, core collapse supernovae (CCSN), gamma ray bursts (GRBs), giant flares from magnetars, eccentric binary coalescences, pulsars, and others.

Below, we review in more detail perhaps the most interesting and mysterious astrophysical sources of GWs: gamma ray bursts. GRBs, discovered only about 50 years ago, are still poorly understood in many respects, even though significant progress has been made in the last two decades. By reaching through shrouding blastwaves, efficiently discovering off-axis events, and observing the central engine at work, GW detectors will soon revolutionize the study of gamma ray bursts.

In this section we examine the three main astrophysical phenomena that are thought to be progenitors of GRBs: compact binary coalescence, the core collapse of massive stars, and magnetars. In Section 1.2.1 we review the suggested emission processes of these progenitors. In Section 1.2.2 we review some of the interesting astrophysical questions that could be answered via the detection of GWs from gamma ray bursts.

1.2.1 Gravitational wave emission processes in GRBs

Here we survey different GRB models, focusing on their expected GW signature. The aim of this survey is to outline the range of possible GW emission from GRBs, which vary widely with respect to predicted signal strength and characteristic frequency, as well as model assumptions.

Compact binary coalescences

Compact binary coalescences, i.e. NS-NS/BH-NS mergers, are thought to power the majority of the short-hard GRBs [25, 26, 27, 28]. As EM observations provide only limited information on these mergers, and due to the complexity of the process, an important tool in better understanding their properties is through analytical and numerical methods.

Numerical simulations performed to model NS-NS or BH-NS binaries have aimed to reproduce an increasing portion of the physics involved in the merger, such as general relativity (GR), detailed microphysics, realistic equation of state (EoS), spin, and magnetic fields. See Refs. [29, 26, 30] for reviews. Fig. 1-1 shows a schematic diagram of the main steps of binary evolution, illustrating similarities and differences between NS-NS and BH-NS binaries. Fig. 1-2 summarizes the main features of GW emission in a schematic spectrum of the GW effective amplitude.

Inspiral phase

The inspiral phase occurs when the two objects are significantly farther from each other than their respective radii. For the early inspiral phase, the bodies can be described essentially like point masses. The finite size of the NSs, their precession and magnetic fields play little role [31, 30].

As the two objects approach each other, these properties become increasingly important. For instance, the tidal deformation of NSs in a binary system can slightly affect the rotation

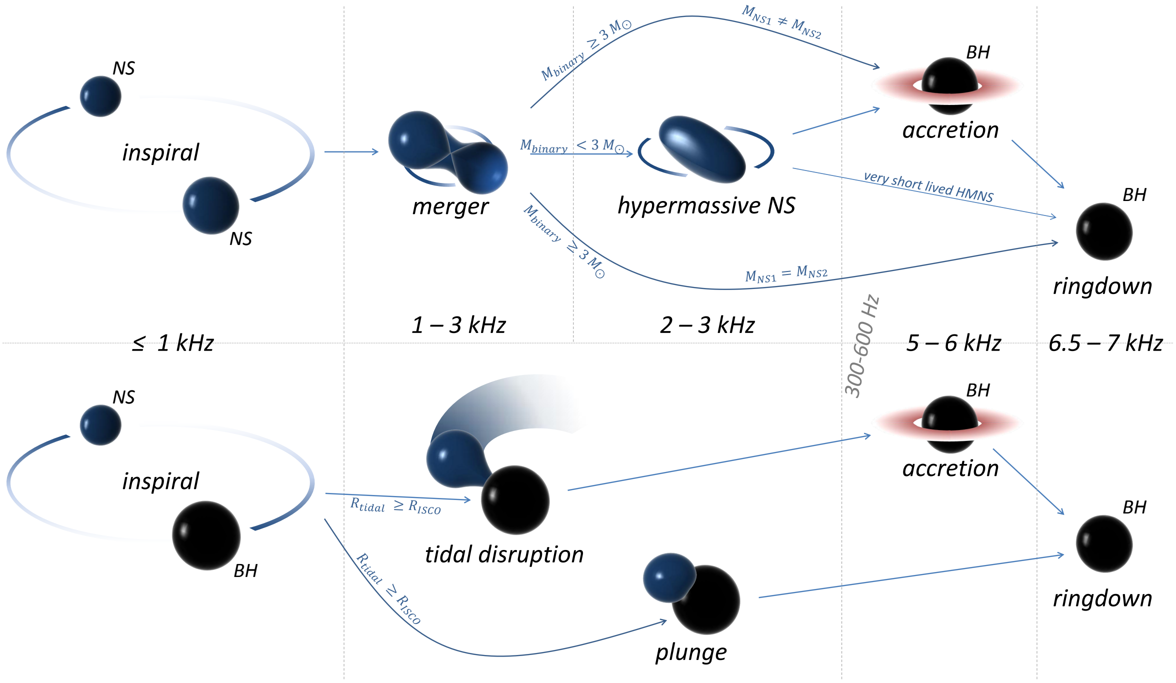

Figure 1-1: Schematic diagram of the evolution of compact binary coalescences. While the inspiral phase is observable for a few seconds, the merger and ringdown phases last only a few milliseconds. If a hypermassive NS is formed during the merger, it can survive potentially for up to a second before collapsing into a BH.

period (and therefore the GW waveform) in the late inspiral phase [32, 33, 34]. If any of the objects is rapidly rotating, general relativistic spin-orbit or spin-spin coupling can cause the binary's orbital plane to precess, significantly affecting the binary's evolution and GW emission [35, 36, 37]. Magnetized NS-NS binaries have an extended inspiral phase compared to non-magnetized binaries [31]. This delayed merger of magnetized NSs results in a much stronger GW signal during this phase because a few more inspiral periods are added to the waveform. For BH-NS binaries, increasing the BH spin (prograde) can also prolong the inspiral phase and increase the mass of the final accretion disk [38, 39], as the radius of the BH's innermost stable circular orbit (ISCO) is smaller for prograde Kerr BHs than for non-spinning BHs.

Binary early inspirals are of special interest for the detection of GWs. As the binary's orbital frequency increases, for some time during the binary evolution it will emit GWs in the most sensitive frequency band ($\sim 150\,\mathrm{Hz}$) of earth-based interferometers, reaching relatively high signal-to-noise ratios compared to later, higher-frequency phases. The Advanced LIGO-Virgo network will be able to detect a NS-NS inspiral up to $\sim 450\,\mathrm{Mpc}$, while BH-NS inspiral will be detectable up to $\sim 950\,\mathrm{Mpc}$ (for optimal source orientation) [40]. This corresponds to potentially tens of NS-NS and a few BH-NS binaries detected with advanced detectors each year [40]. Third generation detectors are expected to reach 10× farther than advanced detectors, to several Gpc, and thus will be able to observe tens of thousands of events a year (e.g. [41]).

The effective amplitude of GW signals in the early inspiral phase scales approximately with $h_{eff} = h(f)f \sim f^{-1/6}$ [42, 1], up to the cutoff frequency $f_{cut} \sim 1-3\,\mathrm{kHz}$ [42, 43, 1], with $\lesssim 1\,\mathrm{kHz}$ and $1-3\,\mathrm{kHz}$ traditionally considered the inspiral and early merger phases, respectively (for $f \lesssim f_{cut}$ the merger retains a binary-like structure) [1].

Merger phase

Depending on the binary system, the merger phase can progress in distinct directions with qualitatively different GW and gamma-ray emission. For the creation of GRBs, it is probably crucial that a massive accretion disk is formed [26]. Disk formation requires the tidal disruption of a NS at some point in the merger [44, 38, 39]. Whether tidal disruption occurs

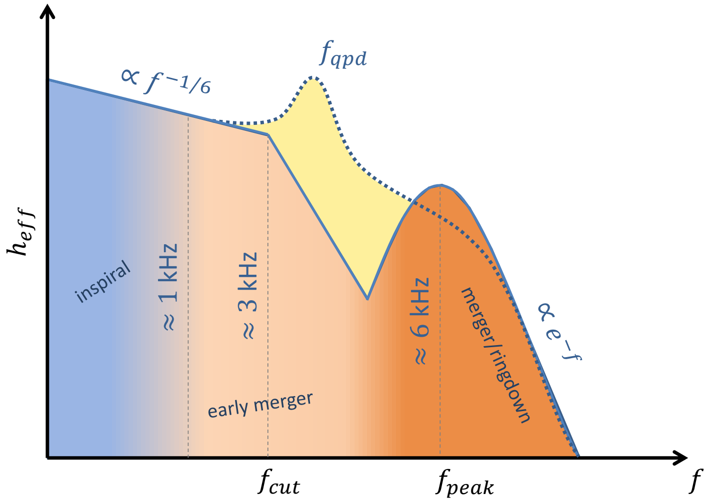

Figure 1-2: Schematic spectrum of effective amplitude h_{eff} for compact binary coalescences. During the inspiral phase up to $\approx 1\,\text{kHz}$ and the early-merger phase up to $f_{cut} \sim 3\,\text{kHz}$, the system retains its binary-like structure and h_{eff} scales as $f^{-1/6}$. If a BH is present or is promptly formed, matter quickly falls in the BH, losing angular momentum through emitting GWs around a peak frequency $f_{peak} \sim 5-6\,\text{kHz}$. If a HMNS is formed from a NS-NS binary, it will radiate GWs through its quasiperiodic rotation at $f_{qpd} \sim 2-3\,\text{kHz}$. As the HMNS loses substantial angular momentum before collapsing into a BH, its GW emission at f_{peak} will be smaller. After matter falls into the BH, the BH rings down, emitting GWs at $\approx 6.5-7\,\text{kHz}$ with exponentially decaying amplitude. (Inspired by Fig. 2 of Ref. [1]).

depends on the binary properties (mass, spin, etc.), as well as the NS EoS. A disk mass of $\sim 0.01\,\mathrm{M}_\odot$ is probably sufficient to supply the energy for the creation of a short GRB [1]. According to accretion disk simulations, the observed variability in gamma-ray luminosity can also originate from accretion [45].

Here we list the possible outcomes of a merger and outline the scenarios that can lead to them.

- **Prompt BH formation with no accretion disk** — for BH-NS binaries if the ISCO radius R_{ISCO} is greater than the tidal disruption radius R_{tidal}, the NS plunges into the BH before it could be tidally disrupted, resulting in a BH with no accretion disk. This will be the case for binaries with relatively high BH-NS mass ratio ($\gtrsim 5:1$) [38, 39, 26]. For spinning BHs, the mass ratio above which no disruption occurs is higher [46].

  For NS-NS binaries with equal masses, if the binary mass exceeds a threshold M_{thr}, the NSs will promptly collapse to a BH upon merger [47], leaving essentially no accretion disk behind [44, 47]. Kiuchi et al. [34] find, in a full GR simulation with hybrid EoS, that a BH is promptly formed if total mass of the binary system is $\gtrsim 2.9\,\mathrm{M}_\odot$. In this scenario, GWs are emitted around a peak amplitude $f_{peak} \sim 5-6\,\mathrm{kHz}$, corresponding to matter falling into the central BH [1]. At such high frequency, the detection of this GW component is difficult with current interferometers. This scenario is not a good candidate for the creation of GRBs.

- **Prompt BH formation with accretion disk** — For BH-NS binaries with relatively low mass ratio ($\lesssim 4:1$), the NS will be tidally disrupted before falling into the BH, which leads to the formation of a massive accretion disk [48, 38, 39, 26]. For spinning BHs, the mass ratio below which disruption occurs is even higher [46], and the mass of the formed disk can greatly depend on BH spin and spin-alignment [49]. For NS-NS binaries with unequal NS masses and sufficiently large total mass ($\gtrsim 3\,\mathrm{M}_\odot$ [34, 50]), the smaller NS will be tidally disrupted followed by the larger NS's prompt collapse into a BH, leaving a potentially massive accretion disk behind [51].

  In this scenario, GWs are emitted around a peak amplitude $f_{peak} \sim 5-6\,\mathrm{kHz}$ (similar to the previous case), corresponding to matter falling into the central BH [1]. At such high frequency, the detection of this GW component is difficult with current interferometers. This scenario is a good candidate for the creation of accretion-powered GRBs.

- **Hypermassive NS formation** — NS-NS binaries with total mass $\lesssim 3\mathrm{M}_\odot$, [34, 47, 50] will not promptly collapse into a BH, but will first form a so-called hypermassive NS (HMNS) supported by differential rotation and thermal pressure [26, 1, 50]. The collapse of the HMNS into a BH is delayed ($\gg 10\,\mathrm{ms}$) until enough angular momentum and temperature is lost through GWs, magnetic processes and neutrino emission [50, 52].

  A rapidly rotating HMNS with stiff EoS will assume an ellispoidal shape, this being energetically favorable over a spheroid [26]. Such an ellipsoidal HMNS will emit a strong GW signal at its (quasiperiodic) rotational frequency $f_{qpd} \sim 2-3\,\mathrm{kHz}$ [43, 34, 47, 50].

  HMNS rotation is differential, its core rotating faster than its surface. For a HMNS with large magnetic fields, its core loses angular momentum due to magnetorotational instability (e.g. [53]) or magnetic winding (e.g. [54, 31]), eventually collapsing into a BH with a massive accretion disk. Losing angular momentum through magnetic effects, however, decreases GW emission, which is the competing mechanism through which the system would lose angular momentum.

  HMNSs may leave a massive accretion disk behind after collapsing into a BH [44, 47, 55]. It seems that the outcome gradually depends on the binary mass. As the total binary mass decreases, the livetime of the HMNS increases, resulting in stronger GW emission and a more massive accretion disk. This gradual change is suggested by the intermediate step found by Hotokezaka et al. [47], who found that with total masses just below prompt BH formation, a very short-lived HMNS is formed with likely suppressed accretion disk formation.

  In this scenario, a significant amount of GW energy is emitted from the HMNS at around its quasiperiodic rotation frequency. Quasiperiodic GW emission from a HMNS may be detectable with advanced detectors from $\sim 20\,\mathrm{Mpc}$ [56, 50], especially because it will be accompanied by an inspiral phase with significantly higher SNR. This scenario is a good candidate for the creation of accretion-powered GRBs.

Accretion disks themselves may contribute to the GW emission of binaries [57]. BH-torus systems can be unstable to non-axisymmetric perturbations [58] that may give rise to non-axisymmetric torus structure, resulting in quasiperiodic GW emission at a few-hundred Hz. While this contribution is weaker than GWs from the inspiral phase, it may be detectable from up to 100 Mpc [57].

Ringdown phase

Above $\sim f_{peak}$ at $\approx 6.5 - 7\,\mathrm{kHz}$, the GW spectrum is qualitatively independent of the properties of the binary. It decays exponentially due to the $m = 2$ quasinormal mode oscillation of the final black hole [42, 26]. For solar-mass binaries, GW radiation from the BH ringdown is undetectable due to its high frequency.

For NS-NS binaries in which a long-lived HMNS is formed, a significant fraction of the angular momentum is lost before the HMNS collapses into a BH. This decreases the angular momentum that remains for the ringdown phase, substantially reducing the ringdown amplitude.

Collapsars

Collapsars emit GWs through various mechanisms [59]. Below we focus on the mechanisms producing GWs that may be sufficiently strong to be detected on scales relevant to GRBs, i.e. that are detectable from $\gg 10\,\mathrm{Mpc}$ with 2^{nd} or 3^{rd} generation GW interferometers. A schematic diagram of these emission processes are shown in Fig. 1-3. For recent reviews on GW emission mechanisms that are relevant for galactic and nearby sources ($< 10\,\mathrm{Mpc}$), see, e.g., [60, 41, 61].

Rotational instabilities in protoneutron stars

For massive stars with initial stellar masses $10\,\mathrm{M}_\odot \lesssim M \lesssim 30\,\mathrm{M}_\odot$, the collapsing core is expected to form a NS [62]. The resulting rotating protoneutron star (PNS) can be unstable to non-axisymmetric deformations, giving rise to copious GW emission [63, 64, 65, 66]. The onset of rotational instabilities depends on the rotational rate of the star, which can be conveniently parameterized by $\beta \equiv T_{rot}/|W|$, i.e. the ratio of the star's rotational kinetic (T_{rot}) and gravitational potential (W) energies [67]. The resulting non-axisymmetric structure is

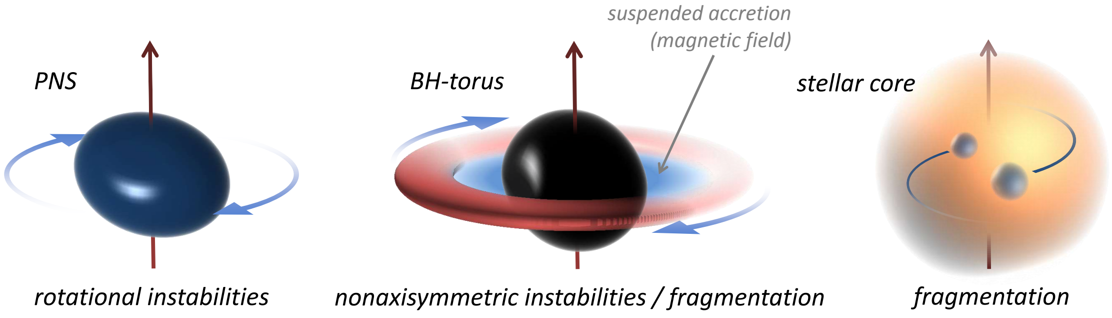

Figure 1-3: Schematic diagram of GW emission scenarios of collapsars.

typically dominated by a growing bar-like $m = 2$ mode, giving rise to a characteristic GW emission at twice the rotational frequency. While there are still various uncertainties in the evolution and role of rotational instabilities (e.g., non-linear mode coupling effects [66] or the role of viscosity and neutrino cooling), the emerging picture is that rotational instabilities are likely viable and strong emitters of GWs and may play an important role in the future detection and understanding of GRBs through their GW signature.

The energy available for GW emission is abundant. The rotational energy of a typical NS with 1 kHz rotational frequency is $\sim 10^{-2}\mathrm{M}_\odot\,\mathrm{c}^2$ (e.g. [68]). Even a fraction of this energy, if radiated away in GWs, could be detectable to large distances ($\gg 10\,\mathrm{Mpc}$) with advanced detectors. The PNS may also accrete supernova fallback material or material from a companion star [69, 70, 28]. Such an accretion further increases the angular momentum and energy that can be radiated away in GWs [71, 72].

The amplitude of a GW signal emitted by a rotating bar scales as $h \sim MR^2 f^2/d$, where M, R, f and d are the mass, radius, rotational frequency, and distance of the NS, respectively [28]. The energy radiated away in GWs, in the Newtonian quadrupole approximation, can be estimated as

$$E_{GW} \approx 10^{-3} M_\odot c^2 \left(\frac{\epsilon}{0.2}\right)^2 \left(\frac{f}{1\,\mathrm{kHz}}\right)^6 \left(\frac{M}{1.4\,M_\odot}\right) \left(\frac{R}{1.2\,\mathrm{km}}\right)^2 \left(\frac{\tau}{0.2\,\mathrm{s}}\right), \tag{1.20}$$

where ϵ is the ellipticity of the bar and τ is the duration of the presence of the instability.

- **Dynamical instabilities** – Rapidly rotating stars will be subject to dynamical instabilities driven by hydrodynamical and gravitational effects [63, 70, 66]. Approximating the PNS as a uniformly rotating, classical fluid body, dynamical instability will arise at a rotation rate $\beta \gtrsim 0.27 \equiv \beta_{dyn}$ [73]. Stability conditions are essentially the same for relativistic stars (for which $\beta_{dyn} \sim 0.24$ [66, 28]). Differentially rotating stars, however, are subject to non-axisymmetric instabilities even at much slower rotation with $\beta \lesssim 0.09$ [74, 75, 76, 77]. Such low-β instabilities in differentially rotating PNSs are probably analogous to the Papaloizou-Pringle instability [58]: the PNS core is surrounded by a fluid rotating at the frequency of a non-axisymmetric mode of the core, hence exciting this mode [70]. As numerical simulations have so far been too short to capture the long-term behavior of some dynamical instabilities, they are not conclusive in terms of the total energy emitted via GWs from dynamical instabilities. Nevertheless, GW emission seems to be fast relative to the cooling time of the PNS, or compared to energy loss due to viscosity. Consequently, if competing mechanisms that radiate away angular momentum (e.g. magnetic fields) are weak, then GWs can carry away a significant part of the PNS rotational energy, producing a signal that may be detectable from

$$D \gtrsim 60\,\mathrm{Mpc}\left(\frac{f}{10^{-2}\,\mathrm{M}_{\odot}\mathrm{c}^2}\right)^{1/2}\left(\frac{f}{1\,\mathrm{kHz}}\right)^{-1} \tag{1.21}$$

for narrow-band, circularly polarized GW signals from optimal source direction (given 10× sensitivity improvement for advanced detectors; based on the results of [78] that used only one GW detector – multiple detectors could see even farther). The frequency scaling of the distance only applies to $f \gtrsim 300\,\mathrm{Hz}$.

- **Secular instabilities** – Stars with lower rotation rates can be subject to secular (dissipation-driven) non-axisymmetric instabilities [79]. Dissipation can be driven by gravitational radiation [79] or fluid viscosity [63, 28]. GW emission drives frame-dragging (the so-called Chandrasekhar-Friedman-Schutz) instabilities to modes that are retrograde with respect to the star but prograde with respect to the observer [80, 81]. Among GW-driven instabilities, f-mode bar instabilities (buoyancy being the restoring force) have the shortest growth time for the relevant rotation rates, is $0.1\,s \lesssim \tau_{GW} \lesssim 7\times10^4$ for $0.27 \gtrsim \beta \gtrsim 0.15$ [82]. In the uniformly rotating approximation of a relativistic star, the PNS becomes unstable to GW-driven $m = 2$ f-mode instabilities for $\beta \gtrsim 0.06 - 0.09 \equiv \beta_{sec}$ depending on the EoS and stellar mass (compare with the Newtonian limit of $\beta \gtrsim 0.14$ [80, 82]) [83]. As angular momentum is radiated away through GWs, the PNS's rotation frequency and therefore the GW frequency decreases, sweeping through the most sensitive band of LIGO-like detectors. Analytical and numerical results indicate that such a GW signal may be detectable at distances up to $\sim 100\,\mathrm{Mpc}$ with advanced interferometers [82, 84, 85, 86]. Some recent, realistic numerical simulations are also promising, even though they only cover the first few milliseconds after core collapse and therefore cannot capture the longer term evolution of the bar mode [75, 76].

Rotating PNSs are also unstable to GW-driven r-mode oscillations (the restoring force being the Coriolis force) at any rotation rate [87, 28]. R-modes will be important if their growth time is greater than the damping time of viscous forces. GW signal from PNS r-modes may be detectable for several years after core collapse [88]. Given such a long duration, the emitted GW signal may be integrated for a measurement of $\sim 1\,\mathrm{yr}$ that would give a detectable signal to distances of $\sim 30\,\mathrm{Mpc}$ [88] (or to even farther if the PNS is a strange quark star [41, 89]). Other calculations (see [28] and references therein), however, suggest the emergence of other modes due to nonlinear coupling that may significantly decrease GW emission from r-modes.

- **Accreting neutron stars** – Some NSs accrete material from a companion star [69, 70, 28]. Some of these systems are observed as Low-Mass X-ray Binaries (LMXB) [28]. It is possible that NSs radiate away the angular momentum they gain from accretion through GWs. Such radiation can happen even at fairly low rotation rates due to r-mode instabilities, which can arise at any rotation rate (although may be damped by the star's viscosity) [71, 90]. Such accretion-induced GW emission is relatively weak, detectable only for galactic or nearby sources with advanced detectors [28]. Nevertheless, such a process can be ongoing for millions of years and therefore the source population is significantly higher than transient events present for shorter time scales.

Accretion disk non-axisymmetric instabilities

Upon the core-collapse of massive stars ($\gtrsim 30\,\mathrm{M}_{\odot}$; [62]), a plausible scenario is the formation of a central BH surrounded by an accretion disk [91]. Such a BH-torus system can be the source of copious GW emission if the disk assumes a finite quadrupole structure due to non-axisymmetric instabilities [59]. The emergence of such a non-axisymmetric structure on the time scales comparable to the life time of the accretion disk requires a stellar progenitor with sufficiently high angular momentum. A high rotation rate is also probably required for the creation of a GRB (e.g. [92]). Below we outline some of the possible scenarios through which non-axisymmetric instabilities in accretion disks may result in strong GW emission.

- **Non-axisymmetric structure via Papaloizou-Pringle instability** – Differentially rotating accretion disks can be subject to a global non-axisymmetric (so-called Papaloizou-Pringle, PP) instability [58, 93]. The PP instability gives rise to a ($m = 1$) non-axisymmetric structure, on a dynamical time scale (i.e. order of rotation period). Such non-axisymmetric structure can persist for much longer than the dynamical time scale, resulting in strong, quasiperiodic GW emission. The PP instability and the resulting non-axisymmetric structure have been observed in 3D relativistic simulations of BH-torus systems [94, 57]. These simulations indicate that BH-accretion disk systems subject to the PP instability emit GWs in the 100-1000 Hz frequency range that may be detectable from ~ 100 Mpc with Advanced LIGO/Virgo [57]. Strong magnetic fields present in the accretion disk can enhance the instability for thick disks (and may suppress it for thin disks) [95].

- **Disk fragmentation via gravitational instability** – Accretion disks with sufficiently large angular momentum are gravitationally unstable [96, 97, 98]. A gravitationally unstable disk will fragment if the disk cooling time is sufficiently short ($\lesssim$ orbital period) [99]. The resulting fragmented disk will emit a strong chirp-like GW signal [100]. Viscosity and GW emission drive the angular momentum loss of the disk. Consequently, low disk viscosity favors stronger GW emission, which may be detectable from ~ 100 Mpc with Advanced LIGO/Virgo [97]. GW frequency at its highest signal-to-noise ratio (SNR) is probably in the $10^2 - 10^3$ Hz range, depending on the strength of viscous forces. The duration of GW emission may be similar to that of gamma-ray emission. Further, the tidal disruption of fragments in the accretion disk may result in some of the X-ray flares observed in GRB afterglows [97]. Accretion disk fragmentation has been found in approximate numerical simulations [98].

- **Suspended accretion** – It has been speculated (e.g. [101]) that, in order for accretion around a central, rotating BH to continue for the time scales of long GRBs, accretion is "suspended" (i.e. slowed down). Such suspended accretion may be achieved through magnetic fields, which transfer some of the rotational energy of the BH to the disk. A significant fraction of this rotational energy can then be radiated away through GWs, making the central BH a large reservoir of energy transferable to GW emission. In order to emit GWs, the accretion disk needs to lose its axial symmetry, e.g., through fragmentation. GW radiation from suspended accretion has been estimated to carry away as much as $E_{GW} \sim 10^{-2}\,\mathrm{M}_\odot$ in the sensitive frequency band of LIGO/Virgo-like interferometers over a duration comparable to the duration of long GRBs ($\sim 30\,\mathrm{s}$) [101, 102]. Such a source may be detectable to $\sim 100\,\mathrm{Mpc}$ with advanced detectors. Suspended accretion may be present even for slower-rotating stellar progenitors, compared to other types of disk fragmentation.

- **Fragmentation of collapsing core** – In very rapidly rotating stars, infalling matter may fragment even before the formation of a BH-torus system. It has been suggested that, in analogy with observed phenomena in star formation, the collapsing core may fragment and form two or more compact objects [103, 104, 100]. Such fragmentation was observed in relativistic numerical simulations of approximate pre-supernova cores [105, 106, 107]. Such core fragmentation would give rise to strong, characteristic GW emission, similar to the case of binary mergers. Nevertheless, the rotation rate necessary for such fragmentation seems to be difficult to achieve with current stellar models [59].

Magnetars

Highly magnetized neutron stars (magnetars) are thought to be the engine behind soft gamma repeaters (SGRs) and anomalous X-ray pulsars (AXPs) [108, 109, 110, 111, 112]. Some magnetars occasionally produce so-called giant flares that resemble short GRBs ([113] and references therein). Giant flares are much less energetic than typical short GRBs at cosmological distances, hence they are only detectable from the Milky Way or nearby galaxies, up to $\lesssim 40\,\mathrm{Mpc}$ with current instruments [113]. The lack of excess short-GRB population from the direction of these galaxies indicates that magnetars may only be responsible for a small sub-population of short GRBs [114].

As magnetars can exhibit occasional flaring activity over a long period of time, giant flares are much more common (with much weaker gamma emission) than other types of GRBs, as indicated by the rate of observed galactic and nearby giant flares [115, 116, 117, 78, 118]. Due to their vicinity, they will be detectable with GW observatories even with much weaker GW emission compared to other, extragalactic GRBs.

Giant flares (as well as SGR activity or abrupt changes in the NS spin period; [119]) are thought to be the result of so-called starquakes: the tectonic activity (cracking) of the NS crust [119], which is followed by the reconfiguration of the NS's magnetic fields [114]. Starquakes induce seismic vibrations in the NS, causing the observed quasi-periodic oscillations (QPOs) in the X-ray tails of giant flares [120, 121, 122, 123, 124, 121]. It has been suggested [125, 126] that QPOs cannot be driven by oscillations in the NS crust due to the quick ($\sim 1\,\mathrm{s}$) dissipation of the vibration via Alfvén waves into the neutron star interior. Nevertheless, such models, at least for now, have difficulty explaining the stability of QPO frequencies over tens of seconds, or explaining the similar statistical properties of SGR events and earthquakes, the latter of which is known to be due to tectonic activity [114].

NS seismic vibrations result in the emission of GWs [127, 128, 129, 112]. In the optimal scenario for GW emission, magnetic reconfiguration can liberate $10^{48} - 10^{49}\,\mathrm{erg}$ of crustal elastic energy, which is the upper limit for the energy radiated away via GWs [129, 112]. This energy can be even higher if the NS is of strange quark matter [112].

A fraction of the energy from magnetic reconfiguration can excite NS fundamental f-modes. F-modes are damped by GWs on a very short time scale ($\sim 200\,\mathrm{ms}$; [112] and references therein), which is shorter than most other potential damping mechanisms. Therefore, most of the energy in the f-modes may be radiated away via GWs [112]. F-modes oscillate at $1 - 2\,\mathrm{kHz}$ (for stiff EoS), not too far from the most sensitive band of Advanced LIGO/Virgo [128]. Given the extreme case of 10^{49} being transferred into f-modes that oscillate at $\sim 1\,\mathrm{kHz}$, the resulting GW could be detected up to $\lesssim 2\,\mathrm{Mpc}$ with Advanced LIGO/Virgo (given $10\times$

sensitivity improvement compared to initial detectors) [78]. "Stacking" the GW signals from multiple events can extend this distance even farther [130, 118]. In a more realistic scenario in which the excitation energy is comparable to the observed giant flare energy ($\sim 10^{46}$ erg) and not all energy is lost through GWs, the GW signal is probably detectable from the Galaxy with advanced detectors.

Quasi-periodic oscillations (QPOs) with various frequencies from $\sim 10 - 10^3$ Hz and durations up to ~ 100 s have been observed in every giant flare X-ray afterglow so far [120, 121, 122, 123, 124, 121]. Some of these QPOs may be connected to the seismic modes of the NSs [120, 124]. These seismic oscillations may result in the emission of GWs ([117] and references therein), although some of them may be poor GW emitters [131]. Of special interest is the QPO around ~ 100 Hz, which falls in the most sensitive frequency band of LIGO/Virgo. Possible GW emission of $\sim 10^{44}$ erg at this frequency would be detectable out to ~ 10 kpc with Advanced LIGO/Virgo (given 10× sensitivity improvement compared to initial detectors) [78].

1.2.2 GRB astrophysics with gravitational waves

This section addresses the question: What can a GW signal add to our understanding of the physics of GRBs? Detectable electromagnetic radiation, our main source of information on GRBs, is emitted from relatively large distances ($\gtrsim 10^1 3$ cm) from the central engines responsible for the creation of GRBs. GWs are created right at the central engine, and can convey information about it without being distorted by matter on its way to the observer. Here we outline some of the questions of interest that could be answered through observing the GW signature of GRBs.

Binary mergers

- **Progenitors of short GRBs** – As compact binary mergers will be detectable from hundreds of Mpc with the Advanced LIGO-Virgo network [40], within these distances it will be possible to confirm or disprove binaries as GRB progenitors. GWs can be the ultimate tool in progenitor identification, as identification based on EM signals is not always straightforward [27]. By connecting each measured source with the presence or absence of emission, and by exploring the correlations between observed EM counterparts and their binary progenitors, we can therefore probe what drives the central engine.

- **Population prospects** – The populations of short GRBs [132], as well as compact binaries [40], are highly uncertain. The observation of GWs from compact binary coalescences could be an effective way of determining the source population. Due to the very large field-of-view of GW detectors, they can be used efficiently to locate practically all sources within their well-determined horizon distance of hundreds of megaparsecs. As source distances can also be determined using GWs (see next subsection), the binary coalescence population could also be mapped as a function of redshift.

- **Source distance and luminosity** – The detection of a presumably binary coalescence GW signal from an observed short GRB can be used to determine the distance and redshift of the source [133]. In fact, the determination can be done independently of the cosmological distance ladder. Distances of short GRBs can be reconstructed to a $\sim 10 - 30\%$ precision for $\gtrsim 500\,\mathrm{Mpc}$ for NS-NS, and for $\gtrsim 1.5\,\mathrm{Gpc}$ for BH-NS binaries using the Advanced LIGO-Virgo detector network [133]. Reconstructed source distance can then be used to accurately reconstruct the luminosity of short GRBs.

- **Jet angular structure** – The angular structure of relativistic jets from short GRBs is poorly constrained [52]. The rate of binary mergers detected through GWs, together with the rate of short GRBs for which a binary progenitor can be confirmed with GWs, could be used to determine the opening angle of short GRBs.

  Further, the polarization of the inspiral GW signals could be used to characterize the viewing angle of observed GRBs [134]. The GW polarization from a binary inspiral depends on the viewing angle compared to the rotational axis of the binary (e.g. [135]). Towards the rotational axis, the GW signal is circularly polarized, while the polarization becomes elliptical for off-axis observers, eventually becoming linear for observers in the equatorial plane. For sufficiently strong GW signals from the inspiral phase, reconstructing the eccentricity of the GW polarization could provide information on the opening angle. With a large number of measurements, the angular structure of the jet could be mapped as well [134].

- **Neutron Star Equation of State** – The EoS of high-density matter is poorly constrained at NS densities [32]. The observation of NSs with masses up to $\sim 2\,\mathrm{M}_{\odot}$ [136] presume a stiff EoS.

  The evolution of NS-NS/BH-NS binaries greatly depends on the NSs' nuclear EoS. Therefore, the GW signal from binary coalescences can be used to determine/constrain the EoS. The simplest case is the tidal disruption of a NS during the binary merger. The orbital frequency at which tidal disruption occurs can be used to determine the radius of the NS. This, together with the NS mass reconstructed from the inspiral GW waveform [137], can be used to constrain the nuclear EoS [138, 139, 140].

  The tidal deformation of NSs in a binary system can affect the GW waveform even prior to the merger phase. The GW energy spectrum during the last few orbits of a NS-NS binary prior to merger can be used to determine the compactness ratio (M/R) of the NSs [141]. For these last few orbits of the binary, the GW frequency is still reasonably close to the sensitive frequency band of LIGO-type detectors, making the analysis of these last few orbits feasible.

  The tidal deformation of a NS in the inspiral phase can be described by one parameter (the so-called Love number [32]), which is effectively the ratio of the star's induced quadrupole moment to the quadrupole moment of the perturbing tidal gravitational field of the binary companion. Flanagan & Hinderer [32] showed that the nuclear EoS of NSs can be constrained even through the early inspiral phase due to the effect of tidal deformation on the waveform. Read et al. simulated the inspiral phase of NS-NS binaries, showing that NS EoS can be constrained (to $10-40\%$ accuracy) with advanced GW detectors for a source at a distance up to 100 Mpc [33]. With the Einstein telescope, the EoS can be constrained from an order of magnitude farther [140].

  Further, it is possible that the inner part of a NS becomes strange quark matter at high densities. A star made of quark matter can be self-bound, a marked difference from hadronic NSs that are gravitationally bound [29]. The GW emission of a strange quark star is substantially different from that of hadronic NSs [139], hence GWs could be used to determine whether NS interiors may contain quark matter [142, 143, 144].

- **Magnetic fields in neutron stars** – Magnetic fields can play an important role in the evolution of binary mergers as well as in the formation of GRBs [26, 52]. The GW signature of binary mergers could be used to better understand their specific role and field strength in NSs and compact binaries. For instance, fast rotating HMNSs can lose their angular momentum through magnetic processes (e.g. [53, 54, 31]), leaving less angular momentum for GW emission. The attenuation of the quasiperiodic GW signal from an HMNS may be used to constrain the strength of magnetic fields in the HMNS.

  Further, the merger of magnetized NS-NS binaries shows substantial differences compared to the non-magnetized case. For example, aligned NS magnetic fields delay the merger of the stars, resulting in strong inspiral-like GW emission for a few more cycles [31]. As these additional cycles reduce the angular momentum of the system, the after-merger GW signal in the magnetized case will be suppressed. The detection of the merger phase GW emission from NS-NS binaries therefore carries information about NS magnetic fields and their alignment as they were present prior to merger. We note that the inspiral GW waveform shows essentially no dependence on the presence of magnetic fields, not even for very strong fields [51].

  Magnetic fields in NS-NS binaries can be significantly amplified via Kelvin-Helmholtz instabilities in the shear layer between the merging NSs [145, 51]. Even if magnetic fields are small prior to merger, the amplified fields can be strong enough to affect the evolution of the merger and therefore GW emission.

  By reconstructing the magnetic properties of a large number of NSs in binary mergers, one could answer questions such as [29]:

  - What is the highest achievable magnetic field frozen in a stationary neutron star?
  - How is the maximum neutron star mass affected by strong magnetic fields?

- **Accretion disks** – The accretion disk around a BH can be subject to non-axisymmetric (Papaloizou-Pringle) instabilities [58] that can result in the emission of GWs. The GW waveform depends on the mass and other properties of the accretion disk, such as its momentum profile, showing marked difference for different masses and profiles [57]. The large-amplitude, quasiperiodic GW emission from these instabilities will have characteristic frequency of a few hundred Hz, making this signal detectable at distances of up to 100 Mpc [57]. The detection of such a signal, probably together with the detection of the earlier inspiral phase from the binary, could be utilized to reconstruct properties of the accretion disk, even if no EM signal is observed from the source.

Collapsars

- **Progenitors of long GRBs** – One of the most important goals of GW astrophysics is to shed light onto the mechanism that creates long GRBs. It is anticipated that long-GRB progenitors are collapsars, which can be confirmed via the detection of the GW signature of long GRBs. Further, the internal evolution of a collapsar, which may largely depend on the specific progenitor, can also be examined. For example, the formation of a PNS or a BH-torus system, or the fragmentation of the collapsar core can be differentiated via GWs.

- **Neutron star equation of state** – The mass and radius of NSs have a profound effect on their potential GW emission through rotational instabilities. Detecting the GW signature of these instabilities can be used to constrain the mass-radius relation, and therefore the EoS, of NSs.

  Further, rotational instabilities in NSs result in qualitatively different GW emission for conventional and strange quark NSs [41, 89]. Whether a NS is composed of strange quark matter could be inferred from the detected GW signature of the NS's rotational instability.

- **Neutron star internal physics** – The evolution of the GW waveform from PNS rotational instabilities strongly depends on the internal physics of PNSs. Differential rotation inside a PNS [74, 75, 76, 77], temperature (e.g. [88]), viscosity and neutrino cooling [88] may all leave their mark on the evolution of rotational instabilities and the resulting GW emission.

- **Accretion physics** – For BH-torus systems, the occurrence of suspended accretion [101] can be confirmed or excluded, as for this model the GW frequency is much more stationary than in the case of other models. Also, for BH-torus systems the strength of viscosity (and possibly the strength of other processes through which the torus loses angular momentum) can be determined, as these are competing effects for angular momentum loss: The total loss of angular momentum can be inferred from the GW frequency, while the loss through GWs can be inferred from the GW signal amplitude.

Accretion of matter by the PNS results in extended GW emission due to the intake of angular momentum [71, 72]. As the time scale and nature of accretion is likely different for accretions from supernova fallback material or material from a companion star, the extended GW signal from rotational instabilities will carry important information on the accretion mechanism.

- **Magnetic fields in neutron stars** – Sufficiently strong magnetic fields inside a PNS can be competing with GWs in radiating angular momentum away. As NS spindown may be reflected in the GW frequency, measuring the GW amplitude and NS spindown can provide information on the strength and nature of magnetic fields present in the NS.

Magnetars

The detection of GWs in coincidence with a giant flare from a magnetar would confirm that the phenomenon is indeed connected to the tectonic activity of the NS. Further, the frequency of GWs from NSs excited by, e.g., starquakes, could be used to infer the NS mass, radius and EoS [127, 128, 146]. The GW signature of magnetar giant flares would also differentiate between baryonic and strange quark matter within the NS [112].

1.3 Gravitational Wave Detectors

As we saw in Section 1.1, a passing GW effectively varies (strains) the distance between two nearby test particles. This effect can be utilized to observe GWs. After introducing some of the detectable sources in the previous section, here we outline some of the most important elements of GW interferometry. We also briefly introduce the Laser Interferometer Gravitational-wave Observatory (LIGO).

Pioneering work towards the direct detection of GWs has been carried out by Joseph Weber, through the construction of resonant mass (bar) detectors [147] and a series of (controversial) measurements [148, 149]. A passing GW strains the bar detector that will oscillate at its resonance frequency. Bar detectors are therefore sensitive to GWs in a very narrow frequency band ($< 1\,\mathrm{Hz}$). Due to size limitations, bar detectors are typically sensitive to a frequency somewhere on the order of a kilohertz. Since Weber's work, bar detectors have been constructed with significantly improved sensitivity (e.g.[150]).

In the following, we focus on GW interferometry. Interferometry is well suited to achieve highly sensitive measurements of the effects of gravitational radiation, for a wide range of frequencies [151]. It is based on the the principle that the effect of a passing GW is different on light beams traveling along paths that are not parallels. (see Section 1.1). In the following we describe the operation of GW interferometers in general. We then go on to describe some of the existing and future GW detectors, in particular the LIGO observatory network. [152, 153, 154, 155].

1.3.1 Gravitational wave interferometry

Interferometers measure the differential distance between two paths by sending a synchronized light beam along those paths. The incoming light beams that travel along the two distinct paths are directed to a common point where they interfere. The resulting intensity is determined by the phase difference of the two light beams. This phase difference may be used to reconstruct the differential distance between the two paths. Since light needs to be monochromatic and coherent traveling over long distances, interferometers operate with very stable lasers as light sources.

Michelson interferometer

The most common interferometer type is the so-called Michelson interferometer [156], in which a light beam is split into two by a semi-transparent mirror, the so-called beam splitter. The split beams bounce back on two mirrors at the end of their paths and are recombined by the beam splitter.

In the simplest configuration, one can choose two perpendicular, equidistant paths for the interferometer arms. Consider a Cartesian coordinate system in which the two arms of the interferometer point towards the x and y coordinates. A passing gravitational plane wave, coming along the z axis (with the right polarization), will modify the lengths of the two arms differentially: when the x arm is stretched, the y arm is compressed, and vice versa.

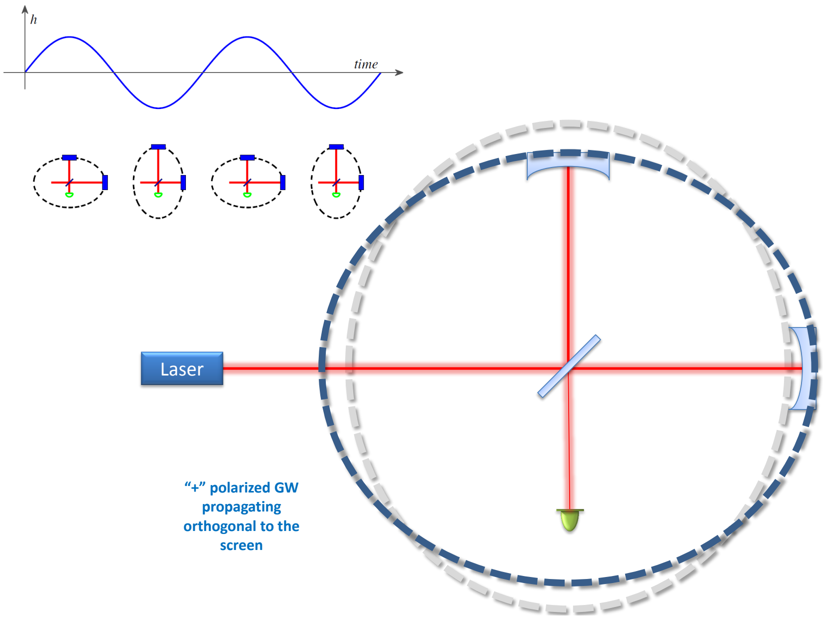

Figure 1-4: Schematic diagram of the effect of a passing gravitational wave on a Michelson interferometer (courtesy of Giacomo Ciani; with modifications).

Such distortion is illustrated in Fig. 1-4). For a GW (+ polarization) amplitude h_+ and interferometer arm length $L_x = L_y \equiv L$ (when no GW is present), the differential arm length between the two arms is defined as (see Eq. 1.16)

$$L_- \equiv \frac{\Delta L_x - \Delta L_y}{2} = \frac{L\frac{1}{2}h_+ + L\frac{1}{2}h_+}{2} = \frac{h_+ L}{4}. \tag{1.22}$$

Measuring the phase difference $\Delta\phi$ of the light beams traveling along the two arms of the interferometer through their interference yields the GW amplitude:

$$h_+ = \Delta\phi\lambda/(4\pi L). \tag{1.23}$$

Fabry-Pérot cavity

As GWs only cause extremely small variations in the lengths of the interferometer arms, further interferometer components need to be added to increase measurement sensitivity. One of the most important additions is the so-called Fabry-Pérot cavity (e.g., [157]), which is placed along each arm of an interferometer. In principle, a Fabry-Pérot cavity consists of two, highly reflecting mirrors, which are used to fold the optical path of the laser beams in the arms. Usually curved mirrors are used to suppress the widening of the laser beam due to diffraction [157].

In a heuristic picture, the cavity's effect is the following: light is reflected back and forth between the two mirrors. After each round trip, a fraction of the light exits. The effect of such a cavity is that light will travel along the interferometer arm multiple times, hence the interferometer has a longer effective length. This amplifies the detector's response to a GW, i.e. a smaller length difference will be measurable with the same precision of measuring $\Delta\phi$. Further, since each photon inside the cavity has a finite probability to exit the cavity after each bounce, a fraction of the light inside the cavity will exit after each bounce. Such an effect is important in measuring GWs whose wavelength is comparable to the folded arm length (i.e. actual length × average number of bounces inside the cavity). For a GW with a wavelength exactly matching the folded arm length, an interferometer for which light bounces a fixed number of times would be completely insensitive as the effect of gravitational distortion cancels out for a photon traveling for the full period of the GW (see, e.g., [157]). For a GW with a wavelength much shorter than the effective length of the interferometer, the Fabry-Pérot cavity increases the signal-to-noise ratio by a factor of N equal to the average number of bounces inside the cavity. Fig. 1-5 shows an example of a Michelson interferometer with Fabry-Pérot cavities in the two arms.

Power recycling

The interferometer's sensitivity to passing GWs depends on the power of the light beam. The precision of measuring the departure from the equidistant interferometer configuration, when light from the two paths destructively interfere, increases with increasing light beam power. Further, higher beam power suppresses shot noise, decreasing the measurement error for higher frequency signals.

To increase the power of the light beam in the interferometer, an additional, so-called power-recycling cavity is formed by placing a partially transmitting mirror (the so-called power recycling mirror) in the path of the beam between the light source and the beam splitter (see Fig. 1-5) [158]. This semi-reflecting mirror "recycles" most of the light that

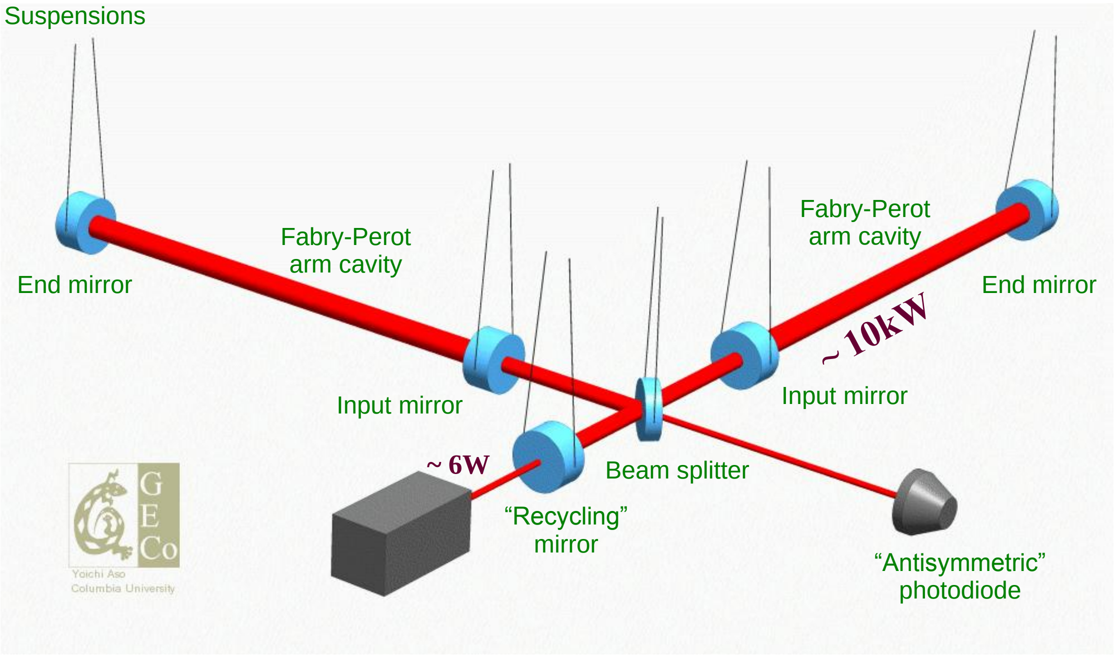

Figure 1-5: Schematic diagram of LIGO (courtesy of Yoichi Aso).

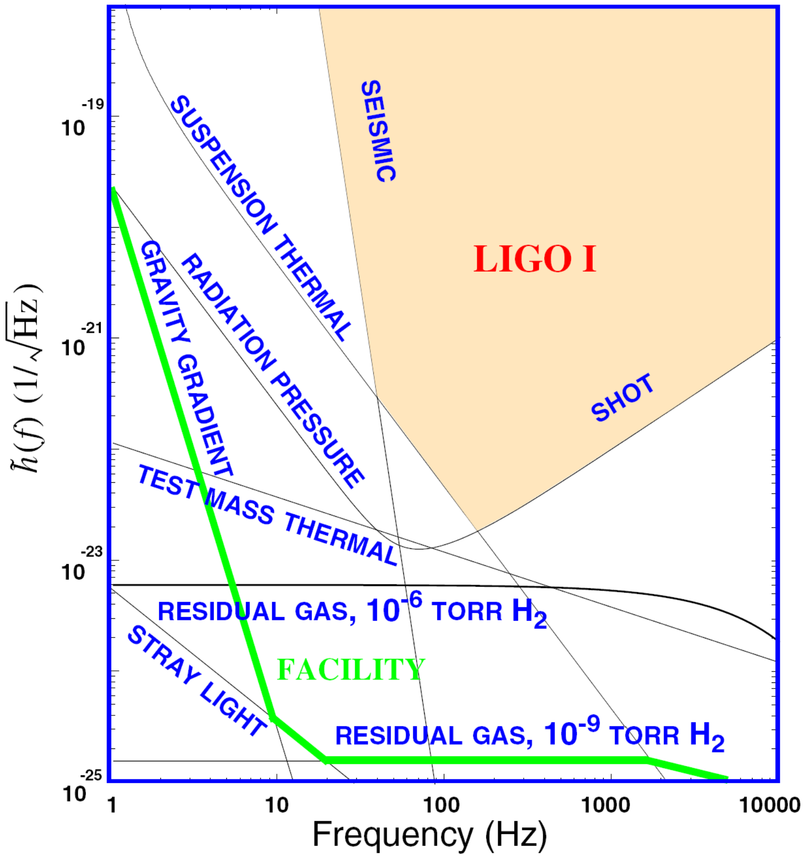

Figure 1-6: Conceptual plot of the dominant sources of noise in LIGO (courtesy of LIGO).

would otherwise leave the system towards the light source. Such power recycling cavity is in fact similar in effect to a Fabry-Pérot cavity [159]. Fig. 1-5 shows an example of a Michelson-Fabry-Pérot interferometer with a power-recycling mirror.

1.3.2 Noise sources in earth-based interferometers

GW interferometers need to face a host of different noise sources that could surpass the extremely weak GW signals. Below we present a short summary of a selection of these noise sources. They can be either displacement noises that affect the actual arm length of the interferometer, or sensing noises that affect our ability to determine the arm lengths [159]. Below we mostly follow the discussion in Weiss [151] in describing the noise sources. The dominant noise contributions for LIGO are presented in Fig. 1-6.

The major noise sources in earth-based interferometers are the following:

- **Seismic** – Motions of the ground, both horizontal and tilt, can drastically change the differential arm length. Various processes can result in seismic vibrations, from earthquakes and ocean waves to traffic and logging. There are also tidal effects due to the Moon that change the separation over typical interferometer lengths with several micrometers. Seismic noise can be the dominant background at low frequencies, albeit "technical" noise[2] is also significant. To ensure a large degree of isolation, GW interferometers are equipped with sophisticated seismic isolation systems (e.g., [160]). As part of such isolation systems, the mirrors of the interferometers are hung from long, thin wires (glass fibers) to minimize the effect of external forces coupling into the motion of the mirror in the direction of the incoming laser beam (see Fig. 1-5).

- **Mechanical thermal** – Mechanical thermal effects introduce displacement noise through the thermal fluctuation of the mirrors and the suspension system of the interferometer. As a consequence of thermal effects, either the mirrors' center of mass moves or their shape varies. In order to minimize such noises, in some planned detector configurations (e.g., KAGRA [161] or the Einstein Telescope [162]), the mirrors will be cooled to cryogenic temperatures ($< 20\,\mathrm{K}$; [163]).

- **Thermal gradient** – A temperature difference between the mirror and the chamber surrounding the mirror results in differential pressure on the mirror via the residual gas molecules within the chamber. Decreasing the gas density around the interferometer is an efficient way of suppressing this noise.

- **Radiation pressure** – Fluctuation in the input laser amplitude results in fluctuating radiation pressure along the beam path. Such fluctuation can introduce noise in the differential arm length through affecting the two arm lengths differently due to slight asymmetries in the arms.

- **Laser output** – Fluctuation in the laser output amplitude results in fluctuation in the perceived interference of the laser beams. Since the level of deviation from completely

---

[2] Technical noises are introduced by the instrument hardware, as opposed to fundamental noises, which are imposed by the laws of nature.

destructive interference can be characterized by the brightness of the interference pattern, fluctuating laser power converts to fluctuation in the conversion factor between the perceived interference level and differential arm length. Laser phase and frequency fluctuations result in displacement noise for non-zero differential arm length [151, 164].

- **Residual gas** – Residual gas in the path of the laser beams causes the fluctuation of the index of refraction along the path, causing a displacement noise. To suppress this effect, interferometers need to be operated at ultra-high vacuum ($10^{-8} - 10^{-9}$ torr; e.g., [154]). This requires that every optical or other component placed inside the vacuum system needs to be cleaned through heating ("baked") prior to its placement in order to remove water and other gases. Further, any kind of activity close to components that will be inside the vacuum system requires specialized protective equipment (see Fig. 1-7).

- **Stray light** – The laser beams in GW interferometers are placed in vacuum system to minimize the effect of residual gas. Some of the light may get reflected from the surface of this system (tube) along the beam path. To suppress this effect, baffles are placed to the inner surface of the tubes to ensure that reflected light cannot couple back to the laser beam, which otherwise would result in displacement noise [165].

- **Gravity gradient** – Ambient seismic waves propagating in the earth induce density fluctuations, which in turn produce varying gravitational forces on the interferometer test masses [166]. While such noise was much below the sensitivity of initial GW detectors, it will be important for advanced detectors. Gravity gradient cannot be attenuated, for instance because of its similarity to stochastic GWs. An effective method for suppressing the effect of gravity gradients is to monitor density fluctuations underground close to the observatory, and subtract their effect from the measured displacement [167].

- **Cosmic rays** – High energy muons from the atmosphere can interact with the interferometer mirrors, causing impulsive displacements of the order 10^{-18} cm for typical muon energies and mirror masses [151]. Such effect, however, is significantly below the sensitivity of GW interferometers [168] (nevertheless, this effect is important for bar detectors, where the deposited energy can excite bar vibrations similar to a passing gravitational wave).

Figure 1-7: Protective equipment is required for activity close to the vacuum system in order to protect the the interferometer from contamination. The figure shows the Author participating in maintenance work at the LIGO Hanford observatory.

1.3.3 Laser Interferometer Gravitational-wave Observatory

LIGO is a network of Michelson-type GW interferometers in the United States (see Fig. 1-8) [154, 169, 170, 171]. Initially, LIGO detectors operated at two sites: two detectors, one with a 4-km and one with a 2-km baseline were placed in Hanford, Washington, while a third one with 4-km baseline was placed in Livingston Parish, Louisiana. Initial LIGO detectors were designed to be able to detect GW strain amplitudes as small as $h \sim 10^{-21}$ in their most sensitive frequency band around $\sim 150\,\mathrm{Hz}$. They were sensitive to GWs in a wide frequency band of $80 - 7000\,\mathrm{Hz}$ [154]. They reached their design sensitivity and continued data-taking from November 2005 to September 2007 as part of the so-called S5 science run. After the S5 science run, the 2-km interferometer in Hanford was decommissioned. After further improvements, another data-taking period (S6) took place from July 2009 until October 2010, with somewhat better sensitivity than S5 (e.g., [172]). Fig. 1-9 shows the sensitivity curve of initial LIGO (S5).

Since the finish of the S6 science run, LIGO is being upgraded to its advanced configuration that will be completed around 2015. The sensitivity of Advanced LIGO is planned to exceed the sensitivity of initial LIGO by a factor of 10. Further, its sensitive frequency band will include frequencies down to $\sim 10\,\mathrm{Hz}$ instead of the $80\,\mathrm{Hz}$ of initial LIGO [170]. The ten-fold improvement in sensitivity will provide 10× farther reach for the detector, increasing the detectable source rate compared to initial LIGO by a factor of 1000. Fig. 1-9 shows the sensitivity curve of Advanced LIGO as a function of GW frequency.

In order to achieve this increased sensitivity, most subsystems of the detector are being replaced with improved components (while the vacuum system will remain mostly the same). There are also additional subsystems that were not present in initial LIGO. One of these subsystems is the signal recycling mirror, which is placed between the beam splitter and the readout [173]. Without the signal recycling mirror (i.e. the case of initial LIGO), the detector's response is maximal to an essentially zero-frequency GW, and decreases for greater frequencies. The rate of this decrease depends on the finesse of the Fabry-Pérot cavities. Increased finesse corresponds to greater response at low frequencies, while there is no change for high frequencies (see, e.g., [157]). The limitation of using an ever greater finesse is the thermal tolerance of the optics.

Figure 1-8: The LIGO interferometers at Hanford, Washington and Livingston, Louisiana (USA).

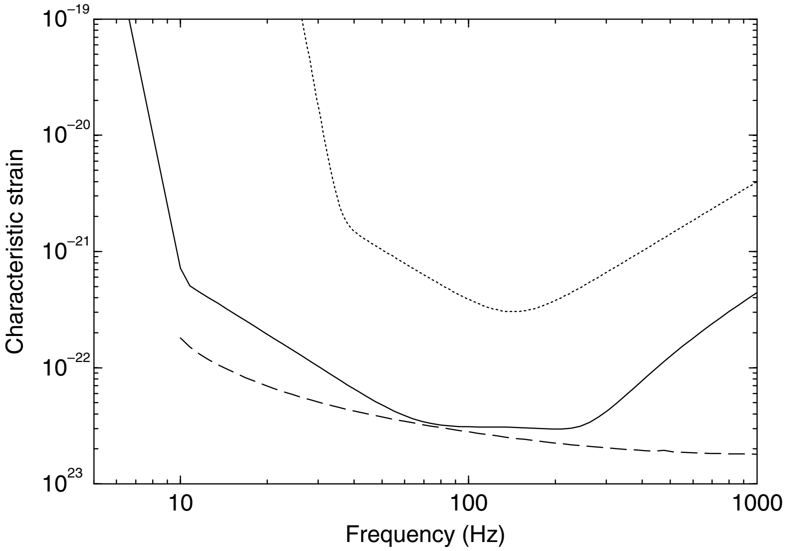

Figure 1-9: Characteristic noise amplitudes ($\sqrt{fS_n(f)}$, where f and $S_n(f)$ are the GW frequency and detector's power spectral density, respectively) of initial LIGO (dotted), Advanced LIGO in a broadband configuration (solid), and the minimum noise level achievable with Advanced LIGO in its narrow band configuration (dashed). Taken from [2].

With the addition of the signal recycling mirror, one can displace the frequency of maximal response to higher frequencies, with the expense of greater suppression for lower frequencies [173]. Such displacement can be useful if one aims to find GWs from narrow-band, high-frequency sources (see Section 1.2 for examples of such sources). Fig. 1-9 shows the sensitivity achievable with the narrow band configuration for individual frequencies (i.e. the sensitivity shown can be achieved for one specific frequency at a time).

Advanced LIGO will consists of three detectors. Beyond one detector in Hanford and one in Louisiana, there are plans for placing the third LIGO detector (instead of its originally planned location at Hanford as a second detector) in India [169]. This third, distant location would provide much improved direction reconstruction capability, as well as improved sensitivity, for the Advanced LIGO network.

1.4 Multimessenger Sources of Gravitational Waves and High Energy Neutrinos

In this section we discuss the joint sources of GWs and high energy neutrinos (HENs). Such sources are the aim of intense investigation that will be further discussed in Chapters 4 & 5. The goal of this section is to present some of the important elements of our current understanding of these multimessenger sources.

1.4.1 High-Energy Neutrinos

Production

GRBs are produced by highly beamed, relativistic plasma outflows (jets), driven by a central engine in the GRB progenitor, such as NS-NS binary mergers or core collapse supernovae.

In our discussion below, we will assume that gamma-ray emission is induced through collisionless internal shocks. We note here, however, that GRBs may in fact be created through fundamentally different mechanisms. A promising alternative model is collisional heating [174]. According to this model, variability in the Lorentz factor Γ of a baryonic outflow evolves to a "two-fluid" state, in which, besides the outflowing plasma, there is a neutron outflow with Lorentz factor $\Gamma_n \ll \Gamma$. Nuclear collisions between the neutron and proton fluids produces mildly relativistic pions. These pions immediately decay: $\pi^{\pm} \rightarrow \mu^{\pm} + \nu_{\mu} \rightarrow e^{\pm} + \nu_e$, and $\pi^0 \rightarrow \gamma + \gamma$ [174]. These neutrinos escape the progenitor with observed energies $\sim 0.1\Gamma$ GeV. This model is therefore very promising for creating detectable of HENs. The energy of these $e^{\pm}$ pairs is converted into radiation. Such a radiation above the photosphere results in the observed GRB. We note that similar, collisional heating can result in the production of HENs for pp collisions as well (e.g. [175]). Another possible alternative model for GRBs is Poynting flux powered outflows driven by a magnetized, rotating central engine [176]. Non-axysymmetry in the central engine's magnetic field leads to variations in the electromagnetic field around the engine, which carries energy outwards. Poynting flux can efficiently carry energy in the relativistic jet without the need of baryon transport. This can help explain high Lorentz factors observed in GRBs that would require very large energies if a matter component is also present in the outflow. In such outflows, the GSuch outflows are inefficient emitters of HENs, therefore HEN observations or non-observation will be informative on the Poynting flux components of relaticistic jets [176].

According to the traditional emission model, the variability in the output of the central engine results in internal shocks within the jet, which accelerate electrons and protons to high energies. Internal shocks can occur even when the relativistic jet is still propagating inside the star [177]. For jets inside the star, reverse shocks can also occur [178] at the head of the jet, which can also accelerate electrons and protons to relativistic energies.

Relativistic electrons emit gamma rays through synchrotron or inverse-Compton radiation. Relativistic protons interact with these gamma rays ($p\gamma$), or with other non-relativistic protons (pp), producing pions and kaons. Photomeson interactions produce charged pions (π^+) through the leptonic decay $p\gamma \to \pi^+$. Proton-proton interactions produce charged pions ($\pi^\pm$) and kaons ($K^\pm$). Charged pions and kaons from these processes decay into neutrinos through

$$\pi^\pm, K^\pm \to \mu^\pm + \nu_\mu(\overline{\nu}_\mu) \tag{1.24}$$

Muons further decay to produce secondary neutrinos through, e.g., the process $\mu^+ \to e^+ + \nu_e + \overline{\nu}_\mu$. Nevertheless, if the synchrotron photon density is high enough, or in the presence of strong magnetic fields (i.e. for smaller radii), they may immediately undergo radiative cooling, giving a flux of lower energy neutrinos [9, 179].

The energy of charged mesons from both $p\gamma$ and pp processes is about 20% of the proton's energy, while roughly $1/4^{th}$ of this energy is given to $\nu_\mu(\overline{\nu}_\mu)$ [180]. The energy of the produced neutrinos and antineutrinos is therefore $\sim 5\%$ of the proton energy. The energies of the photon (ϵ_γ) and proton (ϵ_p) in the $p\gamma$ interaction need to satisfy the photo-meson threshold condition of the Δ-resonance [180]

$$\epsilon_\gamma \epsilon_p \approx 0.2\Gamma^2\,\mathrm{GeV}^2 \tag{1.25}$$

where Γ is the Lorentz factor of the shock. Assuming Lorentz factor $\Gamma \sim 300$ and observed γ ray energy $\epsilon_\gamma \sim 1$ MeV, one obtains a characteristic neutrino energy of $\epsilon_\nu \sim 10^{14}$ eV [180].

For both $p\gamma$ and pp processes, the energy spectrum of HENs is determined mainly by the proton energy spectrum, and the optical depths of the $p\gamma$ and pp interactions. The distribution of the proton energy ϵ_p in internal shocks, in the observer frame, is $\mathrm{d}^2N/(\mathrm{d}\epsilon_p \mathrm{d}t) \propto$

ϵ_p^{-2}, with a maximum energy cutoff due to photo-pion losses. The cutoff energy depends on both jet properties and the radius where the internal shocks occur.

The collisional or radiative nature of the internal shocks at high densities can be an impediment to Fermi acceleration. For mildly relativistic jets, particle acceleration happens less efficiently because the shock is somewhat spread out [181]. However, the details of the acceleration process are still uncertain, and for many alternative acceleration scenarios this is not an issue [182, 183, 184]. On the other hand, neutrinos are the best probes for the physics responsible for the acceleration, and HEN observation should shed light on this aspect.

Interactions and Oscillations

HEN emission from internal shocks can commence at a distance $r_s \approx \Gamma_j^2 c\delta t \approx 3 \times 10^9$ cm [177], where $\Gamma_j = 10$ is the jet Lorentz factor and $\delta t = 10^{-3}\,$s is the jet variability time. Photo-pion losses determine the cut-off in the energy spectrum.

Whether and when HENs escape the star depends on the star's optical depth to neutrinos, which depends on neutrino energy as well as where neutrinos are emitted inside the star. HENs can only escape after the relativistic jet gets to a low density region, beyond which the interaction of HENs with the stellar medium is negligible.

The effect of HEN interaction with matter on observable HEN emission prior to the outbreak of the jet has been discussed previously, e.g., by Razzaque, Mészáros, and Waxman [185]. Using a simplified model for the jet and progenitor star, Razzaque et al. found that HEN interaction is negligible if the jet gets close to the surface (estimated as having roughly $\sim 0.1\,\mathrm{M}_\odot$ envelope mass over 4π above the jet front). If the jet is deeper inside the star (with overlying envelope material of $\sim 1\,\mathrm{M}_\odot$), they found HEN interaction effects to be noticeable, especially for stellar models that lost their hydrogen envelope. For this latter case, they found that the neutrino optical depth becomes larger than unity for neutrino energies $\epsilon_\nu \gtrsim 2.5 \times 10^5\,$GeV. Horiuchi and Ando [178] also mention HEN interactions for jets within the stellar envelope. They find that only neutrinos with energies less than $\epsilon_\nu < 10^2\,$GeV can escape a progenitor star from $r \approx 10^{10}$ cm.

The interaction probability of HENs increases with their energy, and can be non-negligible if a neutrino beam were to travel through large quantities of dense matter, as is the case for neutrinos produced inside massive stars. The mean free path of HENs is determined by inelastic scattering processes, with neutrino-nucleon interactions (νN or $\overline{\nu}N$) being the major determinant of the optical depth [10, 186]. At the relevant neutrino energies, the interaction cross sections are approximately the same for all neutrino flavors [186], therefore we treat the cross section to be flavor independent (see [186]). Electron-antineutrinos are the exception to the above, as the interaction of electron-antineutrinos and electrons ($\overline{\nu}_e e$) becomes the dominant effect around the resonant neutrino energy $\epsilon_{\overline{\nu}_e} \approx 6.3 \times 10^6\,\mathrm{GeV}$ [10]. We shall neglect this exception as it only results in the attenuation of a small fraction of HENs, i.e. the radius at which neutrinos of a given energy can first escape does not change.

To obtain HEN interaction lengths, we adopt the neutrino cross sections obtained by Gandhi et al. [10] (other calculations give similar results; see, e.g., [187]). We additionally take into account nuclear effects (i.e. that both free and bound nucleons are present) calculated by Pena et al. [188]. Gandhi et al. [10] calculated the cross sections for charged and neutral currents, the sum of these two giving the total cross section σ_ν. For the range of neutrino energies of interest here, neutrino cross sections are, to a good approximation, flavor invariant [10, 186]. We note that the cross sections for neutrinos and antineutrinos are somewhat different.

The neutrino-nucleon interaction cross section $\sigma_\nu(\epsilon_\nu)$, obtained numerically by Gandhi et al. [10], assumes that matter is in the form of free nucleons. To take into account the presence of bound nucleons (mostly helium), we approximate nuclear effects following Castro Pena et al. [188]. The ratio of the total cross section $\sigma_\nu(A)$ corrected for nuclear effects over the cross section σ_ν without correction (free-nucleon case) decreases with energy and with atomic mass number A. The effect is practically negligible (order of a few percent) below a neutrino energy of $\epsilon_\nu \approx 10^5\,\mathrm{GeV}$. Above $\epsilon_\nu \approx 10^5\,\mathrm{GeV}$, we approximate the energy dependence presented in [188] (see Figure 2 therein) with the empirical function

$$\frac{\sigma_\nu(\epsilon_\nu, A)}{\sigma_\nu(\epsilon_\nu)} \approx \left(\frac{\epsilon_\nu}{10^5\,\mathrm{GeV}}\right)^{-\ln(A)/556} . \tag{1.26}$$

Given the neutrino interaction cross sections, one can obtain the interaction length (or mean free path) λ_ν via

$$\frac{1}{\lambda_\nu(\epsilon_\nu, r)} = \sum_A \rho(r)\omega_A(r)N_{\rm av}\sigma_\nu(\epsilon_\nu, A) \ , \tag{1.27}$$

where $\rho(r)$ is the stellar density as a function of the radial distance r from the center of the star, $\omega_A(r)$ is the mass fraction of elements with mass number A, $N_{\rm av}$ is the Avogadro constant, and $\sigma_\nu(\epsilon_\nu)$ is the νN interaction cross section as a function of neutrino energy ϵ_ν and atomic mass number A. For antineutrino interaction length $\lambda_{\overline{\nu}}$, the difference compared to λ_ν is the energy-dependent ratio of neutrino and antineutrino cross sections.

Besides scattering, neutrinos also undergo flavor mixing due to neutrino flavor oscillations. After the neutrinos escape the star, the neutrinos travel a very long distance in space wherein the wave-packets of each mass eigenstate must separate. Therefore, neutrinos observed at Earth should be considered as incoherent superpositions of these mass-eigenstates. If the expected neutrino flavor ratio at the source is ϕ_{ν_e}:ϕ_{ν_μ}:ϕ_{ν_τ} = 1:2:0, neutrino oscillations from the source to the detector transform these ratios to 1:1:1 [189]. If muon radiative cooling is significant, then only muon neutrinos are produced through the decay of kaons and pions, i.e. the flavor ratio at the source will be 0:1:0. This leads to measured flavor ratios of 1:2:2 at the detector [189]. Other flavor ratios are possible and have been explored [190]. As the energy and time profile of neutrino emission remains almost unchanged by oscillations, we do not consider these oscillation effects. We note that these ratios can be modified by neutrinos oscillations inside the star that may be important for neutrino energies $\lesssim 10^4$ GeV [186].

Detection

HENs traveling through Earth interact with the surrounding matter creating secondary particles, mostly muons. Cherenkov radiation from these muons is detected by neutrino detectors, which reconstruct direction and energy based on the detected photons [191]. While the IceCube detector [192] has a nominal threshold of $\sim 10^2$ GeV, Earth starts to become opaque to neutrinos with energies $\epsilon_\nu \gtrsim 10^6$ GeV, decreasing the neutrino flux that reaches the vicinity of the detector after crossing Earth [14]. So-called upgoing neutrinos (i.e. neutrinos whose trajectory crosses Earth before reaching the detector) with energies above $\sim 10^6$ GeV are practically undetectable, as most of them are absorbed before reaching the detector (note that this is true for muon-neutrinos; tau-neutrinos can penetrate Earth even at higher energies [14]). For upgoing muons this sets the observable energy window at $(10^2 - 10^6)$ GeV. Downgoing and horizontal neutrinos (i.e. neutrinos whose trajectory reaches the detector without crossing Earth) are detectable at practically any energy [14]. The disadvantage of such directions is the much higher background noise from atmospheric muons that are, for these directions, not filtered out by Earth. Due to this high background, most HEN analyses only consider upgoing HEN events. The only exception is extremely-high energy neutrinos ($\gtrsim 10^6$ GeV), as atmospheric muons seldom reach such high energies.

There are several currently operating HEN telescopes, e.g., IceCube [192], a km^3 detector at the South Pole, and ANTARES [193] in the Mediterranean sea. Both ANTARES and a third detector at the lake Baikal [194] are planned to be upgraded into km^3 telescopes [195]. These km^3-scale detectors observe HEN events and measure their energy, time, and arrival directions. While uncertainties remain in the emission mechanism and expected source flux [196], depending on the model, these km^3-scale detectors may observe $(1 - 100)$ HEN events in the energy range $(10^2 - 10^6)$ GeV, for a typical GRB at 10 Mpc.

The uncertainty of muon energy reconstruction in neutrino telescopes is ~ 0.3 in $\log_{10}(\epsilon_\nu/\mathrm{GeV})$ [197, 198, 199], becoming somewhat larger [199] for partially contained muons of greater energies. Timing resolution is expected to be on the nanosecond level [200, 201]. Angular pointing is expected to be $\lesssim 1^\circ$ at these energies, which may allow identification of the source independently. Although we will not perform a detailed simulation of the observable signal, we shall keep in mind these experimental parameters.

1.4.2 Common sources of gravitational waves and high energy neutrinos

GWs and HENs may originate from a number of common sources. Plausible sources include gamma-ray bursts (GRBs) [180, 202, 178, 203, 204, 185, 205, 206, 207], core-collapse supernovae (CCSNe), soft gamma repeaters [208, 209, 210] and microquasars [211, 212]. For a joint GW+HEN search, potentially the most interesting sources are those which are difficult to detect using electromagnetic (EM) telescopes. Below we shortly describe some of these sources of interest.

Choked GRBs

CCSN progenitors can have observable gamma-ray emission only if the relativistic outflow from the central engine, that is responsible for the production of gamma-rays, breaks out of the star [178]. The outflow can advance only as long as it is driven by the central engine. If the duration of the activity of the central engine is shorter than the breakout time of the outflow, the outflow is choked, resulting in a choked GRB [177].

HENs, due to their weak interaction with matter, can escape from inside the stellar envelope, from depths gamma-rays cannot. Consequently choked GRBs, similarly to "successful" GRBs, may be significant sources of HENs [178, 213]. Choked GRBs are expected to emit GWs similarly to successful GRBs.

Low-luminosity GRBs

Low-luminosity (LL) GRBs [214, 215, 216, 217, 218, 219, 220, 221] form a sub-class of long GRBs with sub-energetic gamma-ray emission. Of the six detected long-GRBs with spectroscopically confirmed SN associations, four are of the LL-GRB variety [222]. Although in general both of these classes of GRBs have been associated with luminous Type Ic SNe, the less energetic SN that accompanied low-luminous burst GRB 060218 suggests that the connection may extend towards lower energy SN explosions (e.g. [218]). In addition, the relative close proximity of observed LL-GRBs implies a much higher rate of occurrence than that of canonical high-luminosity (HL) GRBs [218, 220]. Due to this higher population rate, the total diffuse HEN flux from LL-GRBs can be comparable or even surpass the flux from conventional HL GRBs [207, 223, 224]. While individual LL GRBs are less luminous in neutrinos, the higher population rate makes LL-GRBs valuable sources for GW+HEN searches.

Unknown Sources and Mechanisms

A potential advantage of the search for astrophysical GW and HEN signals is the discovery of previously unanticipated sources or mechanisms. Such mechanisms include, for example, HEN emission at a larger beaming angle than the observed beaming angle for gamma rays.

Source population

Some of the most interesting GW+HEN sources, CCSNe (SNe Ib/c) are expected to be similarly or somewhat less abundant [9] than galactic SNe, with an estimated rate of ∼1/century/Milky Way equivalent (MWE) galaxy [225]. Additionally, late-time radio observations of supernovae indicate that $\lesssim 1\%$ of SNe have mildly relativistic jets [226]. The expected rate of another interesting population, LL-GRBs, is $\sim 3 \times 10^{-5}$ yr^{-1} / galaxy ($\sim$300 Gpc^{-3}yr^{-1}) [227], although this value is highly uncertain [228]. The rate of HL-GRBs is several orders of magnitudes smaller (~ 1 Gpc^{-3}yr^{-1}) [227].

1.5 Searching for Gravitational Waves

In this section we outline the main GW search strategies that have been developed and applied in observations. Further, we outline searches for GW sources performed using the LIGO network (often together with other observatories, e.g. the Virgo GW observatory [229]), organized along the different messengers used together with GWs. The presentation below is based on our recent work to review the GW signature of GRBs, which will be published in the near future.

In the past decade since the construction of LIGO (the first kilometer-scale GW observatory), a large number of searches have been performed with two distinct aims: to achieve the first direct detection of GWs, and to extract astrophysically meaningful information from the measurements. Nevertheless, these two goals require similar steps to be taken in many respects. By achieving a higher probability of observing a GW event, one reaches farther in testing our understanding of the Cosmos and its habitants. Further by combining the information channels from different astronomical messengers, one can extract significantly new information about the source, along with suppressing the false alarm probability of a potentially significant signal.

1.5.1 Gravitational wave search strategies

Search strategies for GW transients can be divided into four main categories based on their use of other messengers.

1 **All-sky** searches, in which no information is used from other messengers (e.g. [230, 231]).

2 **Externally-triggered** searches, in which one specifically looks for GW signals from sources confirmed via other messengers. For instance one can search for GW signals from detected GRBs, using their location, time, and other parameters (e.g. [232, 233, 234, 118]).

3 **EM follow-up** searches, in which GW signal candidates are used to trigger electromagnetic or other follow-up searches with other telescopes (e.g. [235, 236, 237]).

4 **Coherent multimessenger** searches, in which one uses sub-threshold signal candidates from multiple observatories of different messengers in a joint search (e.g. [212, 238, 13]).

In the following we shortly review some of the GW search strategies and past GW searches for GRBs, organized along the above categories.

All-sky searches

All-sky GW transient searches provide a generic way to identify plausible GW sources with minimal assumptions on source models, and without relying on the detection of other messengers. Many initial LIGO/Virgo analyses have been performed as all-sky searches. Besides looking for nearby sources that have not been detected electromagnetically (e.g., off-axis GRBs), all-sky searches were able to set competitive population upper limits on various GW sources. In the latest LIGO-GEO-Virgo all-sky analysis of sources with unmodeled transient waveforms (bursts), Abadie et al [230] have found no significant event, and set a loudest-event source rate upper limit of $R^{\mathrm{UL}} \gtrsim 10^{-6}(E_{\mathrm{GW}}^{iso}/1M_{\odot}c^{2})$ yr^{-1}Mpc^{-3}, where E_{GW}^{iso} is the isotropic-equivalent GW emission of the source. This result was obtained at 90% confidence for the $\sim 1\,$yr long observation, for linearly polarized signals with sine-Gaussian waveform, at the most sensitive frequency band of the LIGO-Virgo detectors ($\sim$ 150 Hz). This upper limit greatly depends on the characteristic frequency of the signal (see Fig. 7 of [230]), as well as the signal waveform (see Tables II, III and IV of [230]). The obtained upper limit can be expressed in source rate per Milky Way-equivalent galaxy, assuming that the source population follows the blue-luminosity distribution of galaxies [13] (see Figure 2 in [13]).

In the latest all-sky analysis for GWs from neutron star (NS)-NS and NS-black hole (BH) coalescences, Abadie et al. [239] used non-detection to establish source rate upper limits over a total mass range of $2M_\odot$-$25M_\odot$. They calculated the so-called horizon distance D_h for the measurement for various sources, which is defined as the distance at which an optimally located and oriented source would produce signal-to-noise ratio (SNR) of 8. For a NS-NS binary each with 1.35 $M_\odot$, they obtained $D_h^{\mathrm{NSNS}} \sim 40$ Mpc, which corresponds to 90% confidence rate upper limit $R_{90\%}^{\mathrm{NSNS}} \approx 1.3 \times 10^{-4}\ \mathrm{yr}^{-1}(L_{\mathrm{B}}^{\mathrm{MW}})^{-1}$ (for non-spinning NSs), where $(L_{\mathrm{B}}^{\mathrm{MW}})^{-1}$ is the blue luminosity of the Milky Way. For a BH-NS binary with 1.35 and 5.0 solar masses, respectively, they obtained a horizon distance of $D_h^{\mathrm{NSBH}} \sim 80$ Mpc, and 90% confidence source rate upper limit of $R_{90\%}^{\mathrm{NSBH}} \approx 3.6 \times 10^{-5}\ \mathrm{yr}^{-1}(L_{\mathrm{B}}^{\mathrm{MW}})^{-1}$.

Externally triggered searches

External triggers in GW searches present various advantages due to the additional information that can be used in the analysis. A crucial advantage of external triggers is greatly increased search sensitivity. An external GRB trigger reduces the temporal and spatial parameter space in which one has to search for a GW signal above the background, which is particularly important due existing non-Gaussian noise transients, so-called glitches, in GW detector data [240]. A detected external trigger can also be used to set constraints on the GW signal. For example, observing a GRB implies that, for most GRB progenitor models, the rotational axis of the progenitor is likely pointing towards the observer (within the beaming angle). For compact binary mergers and for various CCSN models, this implies a circular or closely circular gravitational waveform.

Previous GRB-triggered GW searches include searches for both unmodeled GW bursts and compact binary mergers. In one of the most interesting GW analyses, Abbott et al. [241] searched for signals coincident with GRB 070201, a short-hard GRB whose electromagnetically determined sky position overlapped with the spiral arms of the Andromeda galaxy (M31). Given the proximity of M31, a binary merger from this galaxy would have been observable by LIGO. Abbott et al. used non-detection to rule out a compact binary progenitor. The remaining, most likely progenitor of the event is a SGR, which is likely the first confirmed extragalactic SGR [242]. Other, similar searches are possible for GRBs whose direction overlaps with a nearby galaxy from where plausible GW amplitudes could be detected. Another analysis searched for a GW counterpart of GRB 051103, a short-hard

GRB whose electromagnetically determined sky position was coincident with the M81 group (3.63 Mpc away from Earth) [243]. No evidence for GW emission was found, ruling out compact binary progenitors from M81, making the source a likely extragalactic SGR giant flare.

Besides searches for coincidences with individual, nearby GRBs [244, 241], other analyses searched a large set of GRBs for coincident GW events. In the most recent GW burst search, Abadie et al. [245] looked for GW bursts in coincidence with 154 GRBs. Most GRBs were identified by the Swift [4] or Fermi [246] satellites. No GW event was found, allowing for a median exclusion distance of $D \sim 17\,\mathrm{Mpc}\;(E_{\mathrm{GW}}^{iso}/10^{-2}M_{\odot}c^{2})^{1/2}$ for characteristic GW frequencies of 150 Hz, where E_{GW}^{iso} is the isotropic-equivalent emitted GW energy of the GRB. For NS-NS and BH-NS binaries, the same search yielded exclusion distances of 16 Mpc and 28 Mpc, respectively.

Several GW searches aimed to identify GWs in coincidence with SGR flares [117, 78, 130, 118]. Most recently Abadie et al. used 1279 flares from six magnetars as triggers, aiming to identify GW signals from neutron-star f-mode ringdowns or other GW-producing mechanisms. The search set constraints on the energy of GW emission from these flares comparable to some giant flares' electromagnetic energies, and an order of magnitude below previously existing limits. For a nearby magnetar (SGR 0501+4516) located at $\sim 1-2\,\mathrm{kpc}$ that emitted a large number of flares during the observation period, the obtained upper limit on f-mode GW emission was $\sim 10^{47}$ erg. The upper limit for GW emission at $\sim 10^{2}$ Hz, i.e. within most sensitive frequency band of LIGO/Virgo, was $\sim 3 \times 10^{44}$ erg, a promising limit compared to theoretical upper limits on GW emission from SGRs [112].

Electromagnetic follow-up

With the rise of a global GW detector network, it became possible to reconstruct, albeit with a relatively large uncertainty, the direction of a GW signal candidate. Such reconstruction enables the use of GW signal candidates in triggering electromagnetic (EM) followup observations, during which a telescope or satellite with a limited field of view is used to take observations in the assumed direction (i.e. a larger confidence region) of the GW signal candidate [235, 247]. There are various scientific advantages of such follow-up search:

- As EM observations cannot continuously cover the whole sky with high sensitivity, GWs can be used to guide these telescopes and point towards the right direction at the right time.
- Oftentimes the most interesting and strongest emission from an EM transient comes within the first seconds after its onset. Since GW emission is, in many cases, expected to precede the onset of EM emission, telescopes have the chance to commence follow-up observation in a very early emission stage, or even catch the onset of the EM event.
- GW signal candidates will often have too low significance to be unambiguously identified as extraterrestrial signals. The observation of an EM follow-up event can greatly enhance the significance of the joint observation, making detection more probable.
- Similarly to other multimessenger searches, information from the different messengers can enhance the information (and therefore science) that one can extract from the source.

The first implementations of EM follow-up observations were introduced for the initial LIGO-Virgo detector network in 2009-2010 (S6-VSR2+3 science run) [248, 249]. Events with $\sim 1\text{day}^{-1}$ false alarm rates were selected, and sent out to telescopes after automatic as well as manual data quality validations. Due to the typically large and irregularly shaped reconstructed point spread function, probable directions were further down-selected based on a galaxy catalog [250]. The remaining directions were distributed to various (typically wide-field, robotic, optical) telescopes [251], such as QUEST, TAROT, ZADKO, Pi in the sky, ROTSE, SkyMapper, the Palomar Transient Factory [248], and the Swift satellite [249].

Coherent multimessenger analyses

These analyses generalize the idea behind externally triggered searches by combining information from sub-threshold signal candidates of various messengers into one powerful test statistic. While in many cases each type of sub-threshold messenger would individually have too low significance to be identified as an astrophysical signal of interest, the combination of individual significances can greatly enhance the analysis' potential of identifying astrophysical events (see Chapter 5 for a coherent multimessenger search).

The AMON initiative [252] is planned to combine sub-threshold triggers of multiple messengers in a low-latency coherent multi-messenger analysis. It will introduce a radically new approach that combines multiple messengers in a coherent manner to identify high-significance candidates for EM follow-up observations. It is planned to use the extracted information, besides claiming detection itself, to initiate EM followup observations, which can add to the number of coincidentally observable messengers.

1.5.2 Electromagnetic counterpart

The electromagnetic emission of many GRBs that are beamed towards the earth can be detected even from very large distances. These distances are often much greater than how far GRB progenitors can be detected through GWs. Due to this extremely luminous EM emission, many GRBs are established astrophysical sources, and can be used as external triggers for GW searches. Long GRBs have typical isotropic-equivalent luminosities of $10^{52}\,\mathrm{erg\,s^{-1}}$, and can be detected through their gamma ray emission at redshifts up to $z \sim 10$ [253]. GW emission from long GRB progenitors, considering optimistic emission scenarios, will be detectable out to hundreds of megaparsecs with advanced GW detectors (comparable to NS-NS sensitivity estimate in [40]; see Chapter 1.2). Short GRBs have similar peak gamma-ray luminosities as long GRBs, but have lower overall radiated energy. They are detectable only at smaller distances than long GRBs, up to redshifts $z \sim \mathcal{O}(1)$ [254]. For compact binary progenitors, a GW signal can be detected up to $\sim 500\,\mathrm{Mpc}$ for NS-NS and $\sim 1000\,\mathrm{Mpc}$ for BH-NS binaries with advanced GW detectors [40]. Magnetar progenitors of short GRBs can emit giant gamma flares with energies up to $\sim 10^{46}$ erg that could be detected from $\lesssim 40\,\mathrm{Mpc}$ with existing EM instruments [114, 113]. The GW emission of magnetar progenitors will be detectable, optimistically, for galactic sources [118] (see Chapter 1.2).

GW searches are also promising in the context of GRBs with sub-luminous EM emission towards the Earth. Sub-luminous emission can be difficult to detect/identify with gamma-ray telescopes such as Swift [255], Fermi [246] or the Palomar Transient Factory [256] without external information on the source. GW transient searches can effectively trigger EM-followup searches of such transients. These followup searches can increase the probability of detecting sub-luminous EM transients, while they can also increase detection confidence on the GW side. Some sub-luminous events, such as off-axis GRBs that are beamed away from the Earth, may produce EM radiation with weaker emission than on-axis GRBs. Matter ejected from compact binary encounters may produce such electromagnetic transients [257, 258, 259, 260, 261, 55]: the ejected neutron star matter can undergo radioactive decay, producing a short isotropic emission named “macronova” [262] or “kilonova” [259]. The ejected matter can also interact with the ambient medium, producing an isotropic radio emission detectable for weeks to up to $z \approx 0.1$ [263].

Another sub-class of potentially sub-luminous events are low-luminosity GRBs [220, 227, 207, 264]. These low-luminosity GRBs may be a distinct population from high-luminosity GRBs [227, 264]. Heavier stars may form a black hole after collapse, and produce a high-luminosity, high-Lorentz factor outflow, while lighter stars may form a neutron star after collapse, and drive an outflow with low luminosity and Lorentz factor [265, 264]. Low-luminosity GRBs are thought to be an order of magnitude more common than their high-luminosity counterparts, with lower EM luminosity and smaller beaming angle [220, 227], making them a promising source type for multimessenger detections.

Beyond the prompt gamma-ray emission, GRB afterglows also promise to carry information connected to GW radiation. Corsi and Mészáros [266] showed that the observed X-ray plateau in the afterglow of some GRBs may be connected to the formation of a highly magnetized millisecond pulsar that can lose angular momentum through GWs during a $10^3 - 10^4\,\mathrm{s}$ period.

1.5.3 Neutrino counterpart

Many GW sources, and in particular GRBs, are expected to be copious emitters of neutrinos [267, 268, 8, 177, 211, 269]. Astrophysical neutrino emission can be divided into two main sub-groups based on two distinct emission mechanisms, with two distinct energy ranges. So-called low energy neutrinos (with energies $\epsilon_\nu \lesssim 100 MeV$) are produced in the extremely hot, dense central regions of CCSNe and probably GRBs. High energy neutrinos (with energies $\epsilon_\nu \gtrsim 100 GeV$) are thought to be emitted by shock accelerated particles in relativistic outflows driven by the central engine of the GRB (e.g. [8]). So far only low energy astrophysical neutrinos have been confirmed, and in one instance, for supernova 1987A [270, 271].

One of the advantages of joint GW-neutrino searches [13, 272] is that both GW and neutrino detectors (low and high energy) continuously observe the whole sky, recording signal candidates without the need to "point" the detector in a particular direction. Such full sky coverage is of special importance for multimessenger searches as the sky coverage for each messenger needs to overlap for a joint search. Further, while EM follow-up searches require low-latency response from EM telescopes, GW-neutrino observations can be performed with high latency without loss of information.

Low-energy neutrinos

In CCSN progenitors, the iron core of a massive star collapses after exceeding the Chandrasekhar mass of $\sim 1.44\ \mathrm{M}_\odot$ via silicon shell burning [273]. After the center of the collapsing core reaches nuclear densities ($\rho_0 \approx 10^{14}$ g/cm^3), its compressibility becomes much lower, and it bounces due to the increased pressure. A dynamic shockwave forms that results in a burst of ~MeV neutrinos [274] that carries away a significant fraction of the core's binding energy [275]. In a CCSN, both low energy neutrino [275, 276] and GW emissions [60, 277] are expected to commence near core bounce within a few milliseconds ($\lesssim 10$ ms). This temporal correlation is orders of magnitude greater than correlation with EM signals [238, 269], and can greatly enhance the sensitivity of a search for joint GW-low energy neutrino sources. Low-energy neutrino emission peaks within a fraction of a second after bounce, while emission continues for up to tens of seconds as the protoneutron star cools and contracts [276, 274].

The joint detection of GWs and low energy neutrinos could provide constraints on the CCSN mechanism as well as information on the properties of matter at high energies and densities [269]. For example the neutrino spectrum from CCSNe depend both on the nuclear equation of state (EoS; [278]) as well as the spin of the core [279]. One can break this degeneracy using the additional information available in the GW channel, inferring information on both the EoS and the spin of the core. A potential secondary collapse due to hadron-quark phase transition in the protoneutron star during its post-bounce evolution [280] would also result in characteristic neutrino and GW emissions [280, 281].

Long and short GRB central engines are also probably strong emitters of low energy neutrinos [267, 268, 282, 268]. As the progenitors of long GRBs may be the progenitors of

CCSNe as well [283, 284, 285], emission from long GRBs may commence similarly to the case of CCSNe. In the collapsar scenario, neutrino emission from the core ceases upon black hole formation, while a newly formed accretion disk will become a significant source, as a large fraction of the accretion energy can be carried away by neutrinos [267].

Compact binary mergers – the likely progenitor of short GRBs – are expected to emit low energy neutrinos [267, 268] from the accretion disk around the central black hole. In the case of NS-NS binary mergers, a HMNS may form prior to BH formation, and further produce neutrino [268] as well as GWs [51] emission. Neutrino emission from compact binary mergers is expected to commence at the beginning with the merger phase, in coincidence with the GW burst due to the merger. This GW burst signal is preceded by the much longer inspiral phase, and followed by the ringdown phase. Such temporal coincidence can be utilized in a joint search.

Several large-scale low energy neutrino detectors are currently in operation. These include Super-Kamiokande (Japan) [286], KamLAND (Japan) [287], LVD (Italy) [288], Borexino (Italy) [289] and Baksan (Russia) [290]. Further, the IceCube high energy neutrino detector [291] is also capable of detecting bursts of low energy neutrinos [276], albeit without the ability to reconstruct the source direction. Recognizing the importance of multimessenger observations, Super-Kamiokande, LVD, Borexino and IceCube are members of the Supernova Early Warning System (SNEWS) [292]. These observatories send real-time triggers of detected supernova candidate events, which are distributed to the astronomer community to allow for low-latency follow-up EM (or other) searches.

The most sensitive current low-energy neutrino detectors (Super-Kamiokande and IceCube) are able to detect the low energy neutrino signal of a supernova from up to $\sim$100 kpc [293]. The expected event number within this distance, however, is relatively small outside of the Milky Way. Planned megaton detectors, such as LBNE [294] or Hyper-Kamiokande [295], could detect SNe from up to $\lesssim$10 Mpc [296] with a SN rate of ~ 1 per year. Multimessenger searches of low energy neutrinos and GWs could further increase these detectable supernova rates [297], and would provide increased confidence in a detected signal. This can be especially important when no EM counterpart is detected.

High energy neutrinos

Non-thermal, high energy (TeV) neutrinos are thought to be created by shock-accelerated particles in relativistic outflows driven by the central engine [8, 202, 177, 298, 204, 299, 300, 301]. The emission mechanism is similar for both long and short GRBs, the former expected to be the stronger emitter. Magnetars [302, 303, 209] or CCSNe with rapidly rotating cores [301, 179] are also expected to emit high energy neutrinos (see also Section 1.4.2). While early high energy neutrino emission models have been significantly constrained [192], the standard fireball picture for neutrino emission remains viable [304, 305].

As their production mechanism is connected to that of gamma photons, high energy neutrinos are probably beamed similarly to gamma rays. This decreases the rate of detectable joint sources similarly to the case of EM emission (see above).

There are several ongoing searches for joint sources of GWs and high energy neutrinos. A first externally triggered search using the initial LIGO-Virgo (S5/VSR1 science runs) and the partial ANTARES detector in its 5-string configuration has been completed. The analysis used the directional distribution and the time of arrival of neutrinos to trigger a GW analysis, similar to the analysis used for GW searches with EM external triggers from GRBs (e.g. [233]). The search used the conservative coincidence time window of 500 s of Baret et al. [238], which is a model-motivated, observation based time window on coincident GW and high energy neutrino emission from GRBs (see Section 3.1).

Joint searches for GWs and high energy neutrinos are well-suited for coherent multimessenger analyses, as both messengers have typically sub-threshold significances. For this purpose Baret et al. [272] developed a multimessenger analysis method that coherently combines the significance and other information from the two messengers (see Chapter 5).

1.5.4 Host galaxies

The location of potential or confirmed host galaxies of GRBs can be utilized in GW searches to enhance sensitivity as well as in event selection or localization.

Long GRBs are found to occur in star-forming regions of distant galaxies, in accordance with their association to the deaths of massive stars [284]. Consequently, the rate of long GRBs is correlated to the blue luminosity of galaxies [306, 307, 284, 308, 309]. Long GRBs are actually found in the very brightest region of their host galaxies, which are significantly fainter and more irregular than typical host galaxies of CCSNe, suggesting that they are associated with extremely massive stars, and galaxies with limited chemical evolution [308].

Star-formation rate in host galaxies of short GRBs is significantly lower than that of long-GRB host galaxies [254]. In fact many short GRBs show association with an old (~ 1 Gyr) stellar population in their host galaxies [254, 310], and it is highly unlikely that short and long GRBs are drawn from the same underlying population [310]. Nevertheless, the rate of short GRBs in a given galaxy is correlated with the optical light of their host, and to less extent with the blue luminosity of the galaxy [311], indicating that short-GRB progenitors have a wide age distribution of several Gyr. As neutron stars may experience an initial kick at birth [312, 313, 104], binary mergers can take place far away from the star-forming region where they originate from. For kick velocities of $\mathcal{O}(100\,\mathrm{km\,s^{-1}})$ and inspiral times of several Gyr, binaries can travel megaparsecs from their birth place before their merger [254, 314], traveling far outside their host galaxies. Typical predicted distances are $\sim 10-100$ kpc [132], the predicted distance distribution being well-matched by observed short-GRB distributions [315].

Magnetars [109, 254] form another possible progenitor type of short GRBs, making up less than $\sim 1/3^{rd}$ of their population [310]. They are weaker and softer gamma-ray emitters than other short GRBs, making them identifiable mostly at smaller distances, within the Milky Way and the Large Magellanic Cloud. Their expected GW emission is also much weaker than the GW emission of compact binary mergers, making them interesting for the purposes of GW measurements only at smaller distances. Nevertheless, some detected extragalactic short GRBs may be (unconfirmed) magnetar flares [316]. One GRB (070201) has been likely an extragalactic giant flare from a magnetar, as suggested by GW measurements [115, 116]. Magnetars are thought to be created in SN explosions [316], AS they can receive an initial kick velocity during the SN explosion similarly to radio pulsars, only a fraction of them may be near its respective SN remnant, in accordance with observations [316]. Magnetars are observed to be mostly young ($\sim 10^4$ yr) objects [316], therefore they did not travel far from the star forming region of their respective SNe. Consequently, extragalactic magnetar flares can be expected to occur within the star-forming regions of galaxies.

The expected probability distribution of GRBs can be used to enhance GW searches by providing an addition significance measure to signal candidates (e.g. [272]). A priori information on source distribution has been used in multiple GW-GRB searches using various methods and weights. The used weights depend on the scope of the search in terms of potential sources as well as used messengers. For extragalactic sources, their distribution is expected to follow the galaxy distribution of the universe.

The first GW search where the galaxy distribution played a significant role was the search for the GW counterpart of GRB 070201 [115]. The direction of this short GRB overlapped with the direction of M31. A binary merger from M31 would have been strong-enough to be detected, therefore non-detection excluded this possibility.

The galaxy distribution plays a significant role in EM follow-up searches, in which GW triggers are followed up by EM observations. Since most GW signal candidates have a reconstructed point spread function spreading over a few degrees (which is scattered over a larger area on the sky), it is greater than the field-of-view of most astronomical instruments used for follow-up observations. To decrease the surveyed area on the sky, the directions in which EM follow-up is performed is down-selected using the directions of nearby galaxies overlapping with the GW point spread function [247].

In coherent multimessenger searches, the distribution of galaxies can be used to increase the significance of astrophysical signals as well as to reject background events whose directions do not overlap with the direction of a galaxy (see Chapter 5).

Chapter 2

The Advanced LIGO Timing System

After outlining in Chapter 1.3 the upcoming Advanced LIGO experiment, which holds the promise of the first direct detection of GWs, below we present our work on a mission-critical component of the observatory: the Advanced LIGO Optical Timing Distribution System.

A network of detectors, besides lowering the noise floor compared to a single detector[1], provides increased sensitivity by being able to efficiently reject signal-like background events (called glitches). Glitch rejection is based on the fact that detectors separated by large distances will have uncorrelated backgrounds, while real GW signals are correlated appear coincidentally and have coherent waveforms in the detectors. Direction reconstruction, a crucial element of retrieving astrophysical source information from a measurement, relies upon the accurate knowledge of the arrival times of GW signals to determine the source direction.

This chapter introduces the Advanced LIGO Timing System, based on the work of Bartos et al. [317]. Section 2.1 discusses the role of timing from the perspective of astrophysical measurements and data analysis. Section 2.2 introduces and describes the Advanced LIGO

---

[1] Since the background noise in multiple detectors are independent, while an astrophysical signal is correlated, this correlation can be utilized to efficiently extract an astrophysical signal from the background. Further, one of the main sources of uncertainty in reconstructing astrophysical signals is the non-Gaussianity of the background. Such non-Gaussian features (glitches) can be filtered out by requiring coincidence between multiple detectors.

Timing System that will provide timing for the Advanced LIGO detectors. We discuss the structure and specific components, the synchronization methods and system diagnostics. Finally, section 2.3 presents some performance tests of the Advanced LIGO Timing System that demonstrate its precision in practice and its robustness against environmental and configurational changes. The chapter is based on the extensive description and documentation of the Advanced LIGO Timing System [317, 318, 319, 320, 321, 322, 323, 324, 325, 326, 327, 328, 329, 330, 331].

2.1 Timing in Gravitational-wave Astrophysics

Timing information of GW signals is vital for multiple purposes. First, coincident arrival times in different detectors separated by large distances is one of the main tools of background rejection. Another important purpose of precision timing is the reconstruction of source direction. Not only does it increase detection confidence by enabling comparison to possible celestial sources, but it is also essential for electromagnetic follow-up observations [332]. Furthermore, accurate direction reconstruction can greatly enhance multimessenger, e.g., GW-high energy neutrino joint searches [333, 212, 13].

The accuracy of direction reconstruction largely depends upon the accuracy of timing (it further depends on the network geometry, the source direction compared to detector locations, uncertainty introduced by the analysis method, and detector calibration) [332, 334]. For instance if one precisely knows the arrival time of a signal for a network of three detectors, the signal direction can be precisely reconstructed with a degeneracy including the actual direction and its mirror image with respect to the plane of the three detectors (for some cases amplitude information can be used to break this degeneracy) [332]. A typical angular uncertainty for the advanced LIGO-Virgo detector network for a detectable signal is $\sim 4^\circ$ (for a circularly polarized signal with characteristic frequency in the detectors' most sensitive frequency band, and with signal-to-noise ratio of 8) [334].

Timing jitter, another crucial factor that can affect measurement precision, has special importance due to the intrinsic sensitivity curve of the Advanced LIGO detectors. Timing jitter introduced in the analog to digital converter (ADC) of a detector will result in the sampling process creating higher harmonics to the existing noise. Due to the steep negative slope of the Advanced LIGO noise curve (see, e.g., [335]) at low frequencies, the background at low frequencies below the interferometer's most sensitive frequency regime will be much higher than the background at the frequencies of its higher harmonics. This will result in the higher harmonics being much more emphasized compared to the case of uniform noise spectrum. It is therefore critical to reduce the appearance of higher harmonics by minimizing timing jitter.

As an example to the precision of arrival time reconstruction, assume that a GW signal of frequency f_0 is incident on a detector. The uncertainty of the measured arrival time can be approximated as [336, 337]

$$\Delta t \simeq \frac{1}{2\pi f_0}\frac{1}{\mathrm{SNR}} \tag{2.1}$$

where SNR is the signal to noise ratio. We will assume a signal of higher characteristic frequency of $f_0 \approx 1\,\mathrm{kHz}$, that can be produced by several sources interesting to Advanced LIGO (see Chapter 1.2). With a signal to noise ratio of $\mathrm{SNR} \approx 10$, we obtain $\Delta t \approx 15\,\mu\mathrm{s}$.

The Advanced LIGO Timing System is required to provide timing information with uncertainty below $1\,\mu\mathrm{s}$[2]. This uncertainty limit is safely below the requirements of arrival time or direction reconstruction. This requirement also allows for a possible 1% amplitude and 1° phase calibration - for the case of, e.g., a $1\,\mathrm{kHz}$ signal, this would mean $2.8\,\mu\mathrm{s}$ maximum allowed uncertainty. We note here that, between the actual timing of GW data and the timing signal from the Advanced LIGO Timing System, there are other data acquisition subsystems, whose accuracy might also introduce timing/phase errors that will be added in the total timing error of GW data. It is hence important that the precision of the Advanced LIGO Timing System stays below the limit required by the considerations described above to "leave room" for sources of uncertainty from other subsystems.

The provided timing signals are required to be synchronized to Coordinated Universal Time (UTC) provided by the GPS satellite system. We note that the nominal accuracy of the GPS system provided by the United States government is below 100 ns.

---

[2] This requirement was $10\,\mu\mathrm{s}$ for initial LIGO.

2.2 System Architecture

Timing information for GW detectors requires different levels of synchronization. First, one needs to provide synchronous timing to sub-systems of a given detector, a challenging task due to the large size of the Advanced LIGO interferometers. Furthermore, in order for results to be comparable between each detector and to be comparable with non-GW measurements, timing needs to be synchronized between different detectors, and needs to be synchronized to an absolute time measure.

The Advanced LIGO Optical Timing Distribution System (Advanced LIGO Timing System) [318, 319] provides timing information to detector sub-systems. Timing is synchronized to Coordinated Universal Time (UTC), this way insuring both relative and absolute synchronization [3]. The system distributes timing information in a modular structure. A central component, called the Master module, synchronizes its internal clock to UTC, and distributes this synchronized timing through optical fibers to peripheral components, called Slave modules. Slave modules synchronize their internal clocks to the received timing signal, and provide timing information based on their internal clock signal to external devices. The distribution of timing information is aided using intermediate components, so called Fan-Out modules. Fan-Out modules synchronize their internal clock to the received timing from an upstream source, and distribute it to up to 16 destinations (either other Fan-Out or Slave modules), enabling a highly flexible structure of arbitrary size. We note here that the key element of providing flexibility to the Advanced LIGO Timing System is the use of Field-programmable gate arrays (FPGAs, type: Xilinx Spartan-3E) in each module. FPGAs are integrated circuits designed such that they can be easily (re-) programmed by the user or developer on site, without the need to re-manufacture the modules.

Below we describe the structure of the Advanced LIGO Timing System by following the path of timing information throughout the system. The structure of the system, as well as an example configuration are depicted in Figure 2-1.

We start with the UTC time stamp that is provided by the GPS satellite network. UTC time is received by the Master module through two paths. An external GPS receiver is used to receive and pre-process UTC timing and provide it as the primary input of the Master

---

[3] Optionally, common view GPS can be used to confirm timing precision if requirements make it necessary.

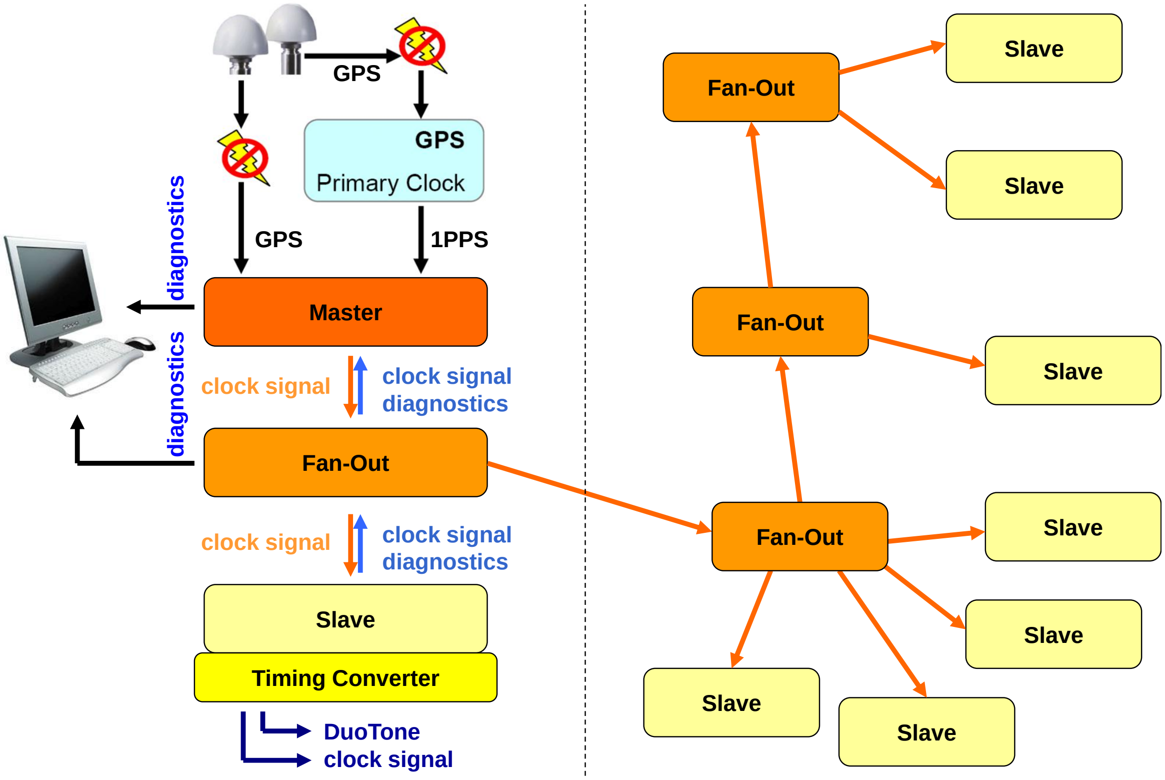

Figure 2-1: (left) Schematic structural diagram of the Advanced LIGO Timing System. The Master module is connected to a GPS receiver module that receives timing from a GPS antenna. Another, failover GPS antenna is connected directly to the Master module. GPS antennae are connected to the GPS receiver and the Master module through lightning arresters. The Master module provides timing information to a Fan-Out module, while the Fan-Out module sends back diagnostics information. The Fan-Out module provides timing information to a Slave module, while the Slave module sends back diagnostics information (including the clock signal that is used to compensate for the time delay in the fiber). The Slave module, together with a Timing Converter interface outputs timing information to an external device. The Master and Fan-Out modules output diagnostics information to an external computer through the internet. (right) Example organization of Advanced LIGO Timing modules in a star-like structure. Practically any number of Fan-Out modules can be serially connected, while one Fan-Out or Master module can provide timing information to up to 16 Fan-Out or Slave modules.

module in the form of one pulse per second (1PPS) signal. The Master module also has its internal GPS receiver sub-module (type: Oncore) that, upon being connected to a GPS antenna, will provide the Master module's secondary, failover 1PPS timing input that is used if 1PPS is not received through the primary input.

2.2.1 Master module

The Master module [318] [4] uses the received 1PPS signal to which it synchronizes its internal clock. The core of the Master module's internal clock is an Oven Controlled Crystal Oscillator (OCXO, type: Wenzel) that has excellent phase noise characteristics and naturally operates on a 2^N Hz base frequency. The OCXO is synchronized to the external 1PPS through a phase-locked loop with a bandwidth of several millihertz, that filters out higher frequency fluctuations in GPS timing.

The Master module provides synchronized timing information through optical fibers based on its internal clock signal, to up to 16 Fan-Out or Slave modules. Timing information is transferred in the form of a 2^{23} Hz (~ 8.4 MHz) square-wave signal. The positive edges of this square-wave signal are spaced equally, and are used as the clock signal. The spacing of the negative edges is used to transfer additional information between the modules, such as the 1PPS signal, or diagnostics information (pulse-width based binary encoding, see also Section 2.2.11).

The time delay due to signal transfer in the optical fibers is automatically compensated for. The Master module sends out a 1PPS signal to the downstream (Fan-Out or Slave) module that, upon reception, immediately sends it back to the Master module. The Master module uses the measured time delay between these two signals to determine and compensate for the time delay due to signal transmission. This synchronization is done upon the connection of a new module, therefore its value does not change during proper operation. The 8.4 MHz clock signal is also adjusted to compensate for the delay due to the cable.

---

[4] Schematics and components information: [322] (front panel) and [323] (rear panel); Assembly Drawing: [324]; Chassis Integration Plan: [326]; Test Procedure: [328]

2.2.2 Fan-Out module

Synchronized (and delay compensated) timing information is transmitted from the Master module to a Fan-Out module [318]. Fan-Out modules use the received timing information to which they synchronize their internal clocks. The core of a Fan-Out module's internal clock is a Voltage Controlled Crystal Oscillator (VCXO, type: Vectron) whose oscillation frequency is synchronized to the received 8.4 MHz clock signal. The 1PPS of the Fan-Out module is determined based on the incoming 1PPS signal.

We note here that the Fan-Out and Master modules are mostly identical, the only difference being the OCXO and GPS receiver that the Master module has but the Fan-Out module does not.

The Fan-Out module, similarly to the Master module, provides synchronized timing information of a 8.4 MHz clock signal and 1PPS signal, based on its internal clock signal, to up to 16 Fan-Out or Slave modules. It also compensates for time delay in the optical fibers similarly to the Master module.

2.2.3 Slave module

Synchronized timing information from the Master module, after being transferred through an arbitrary number of Fan-Out modules, will be received by a Slave module [318]. Slave modules, similarly to Fan-Out modules, use the received timing information to which they synchronize their internal clocks. Their internal clock is also identical to those of the Fan-Out modules.

Slave modules provide timing information to external devices, i.e. detector sub-components. They convert the received 8.4 MHz clock signal and 1PPS signal into the format required by the specific device they communicate with. Slave modules use operation specific interfaces: daughter boards that are placed onto the Slave modules. While these interfaces provide the physical connection between the Slave module and external devices, operation specific timing information is generated within the (also operation specific) FPGA code programmed onto the Slave module's FPGA chip.

Operation specific interfaces include the Timing Converter Interface described below, that is used to synchronize the analog-to-digital and digital-to-analog converters, RF units and some of the CPU clocks of Advanced LIGO. Another interface is the Timing Comparator interface, that is used to (i) output UTC synchronized 1PPS signals from the Slave module through multiple BNC ports and (ii) compare 1PPS signals from several different external devices to high precision. Further interfaces include the IRIG-B (Inter-range Instrumentation Group B) interface, that is used to communicate with devices that require IRIG-B input, such as some computer interfaces.

2.2.4 DuoTone generation

Advanced LIGO analog-to-digital and digital-to-analog converters require a two-tone signal to monitor their state of synchronization. The two-tone signal generated by the Advanced LIGO Timing System, called DuoTone, is the sum of two sinusoids of 960 and 961 Hz. The frequency difference $\Delta f = 1\,\mathrm{Hz}$ between its two components enables the precise determination of every 1 second mark by using the phase difference between the two sinusoids. While, for a 1PPS signal, one uses a few microseconds of data each second to determine the precise position of the 1 second mark (e.g. the rising edge of 1PPS), for a DuoTone signal, one can use the full 1 second long data stream for the same purpose. The narrow Fourier band width of a DuoTone signal is another important advantage that decreases possible cross-channel contamination. The LIGO GW channels can have significant narrow band noise at the 60 Hz power line harmonics. There can be a crosstalk between ADC channels, therefore it was safe to place the frequencies of the timing signals on top of a high frequency line harmonics, where the crosstalk cannot cause an additional loss of bandwidth.

Advanced LIGO sub-components that require DuoTone signal, such as the analog-to-digital and digital-to-analog converters, will be connected to the Timing System through a so called Timing Converter interface [318]. Besides a DuoTone signal, they also require other timing signals, which are shown and explained in Figure 2-2.

2.2.5 Operation Diagram

Fig. 2-3 summarizes the operation of the Master and Fan-Out Modules, representing the main, distinct parts of operation with separate “black-boxes”. The detailed operation of these black-boxes are discussed in subsequent diagrams below. There is an order in which

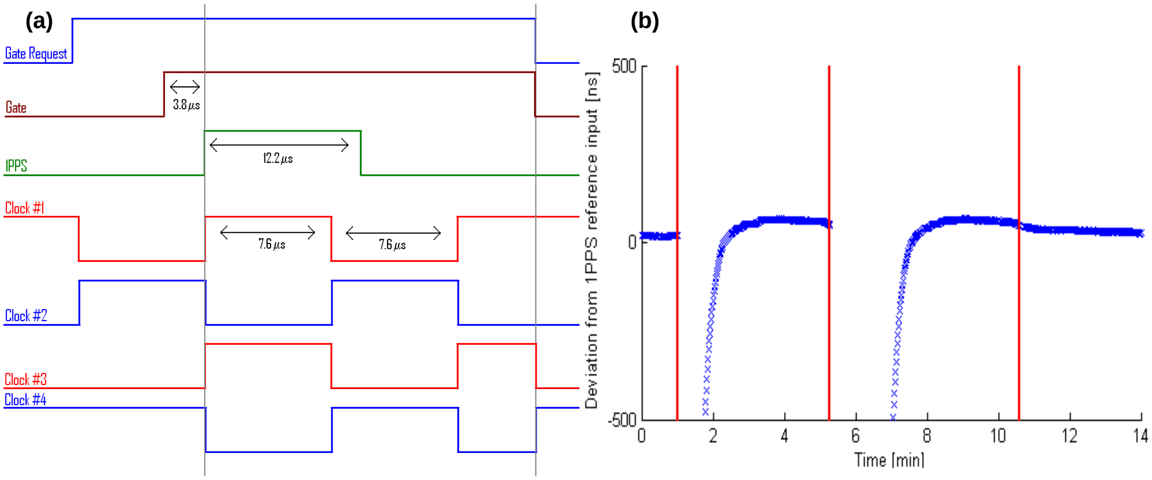

Figure 2-2: (a) Input/Output signals of the Timing Converter interface (excluded the DuoTone signal), compared to 1PPS. The Timing Converter continuously outputs Clock #1 and Clock #2, two 2^{17}Hz clock signals which are the inverse of each other and are synchronized to 1PPS. The external device (i.e. an analog-to-digital converter), upon starting conversion at an arbitrary time, sends a Gate Request signal to the Timing Converter. The Timing Converter outputs a Gate signal after Gate Request was turned on, starting right before the 1PPS signal such that it is closer to the 1PPS signal than the half cycle of Clock #1. The Timing Converter also outputs two additional clock signals, Clock #3 and Clock #4, that are the logical products of Gate and Clock #1 and Clock #2, respectively. (b) On/Off test of the Advanced LIGO Timing System: deviation between the input and output 1PPS signals of a Master-Fan-Out-Slave module chain as a function of time. The red vertical lines show the times of power recycle for the Master module (first and second line) and the Slave (third line) modules. The Master module and Fan-Out modules were connected through a 4km long fiber. The system restores itself and acquires precise timing within 3 minutes after the Master module is restarted, and within 20 seconds after the Slave module is restarted. Note that the Fan-Out module uses the same synchronizing mechanism as the Slave module.

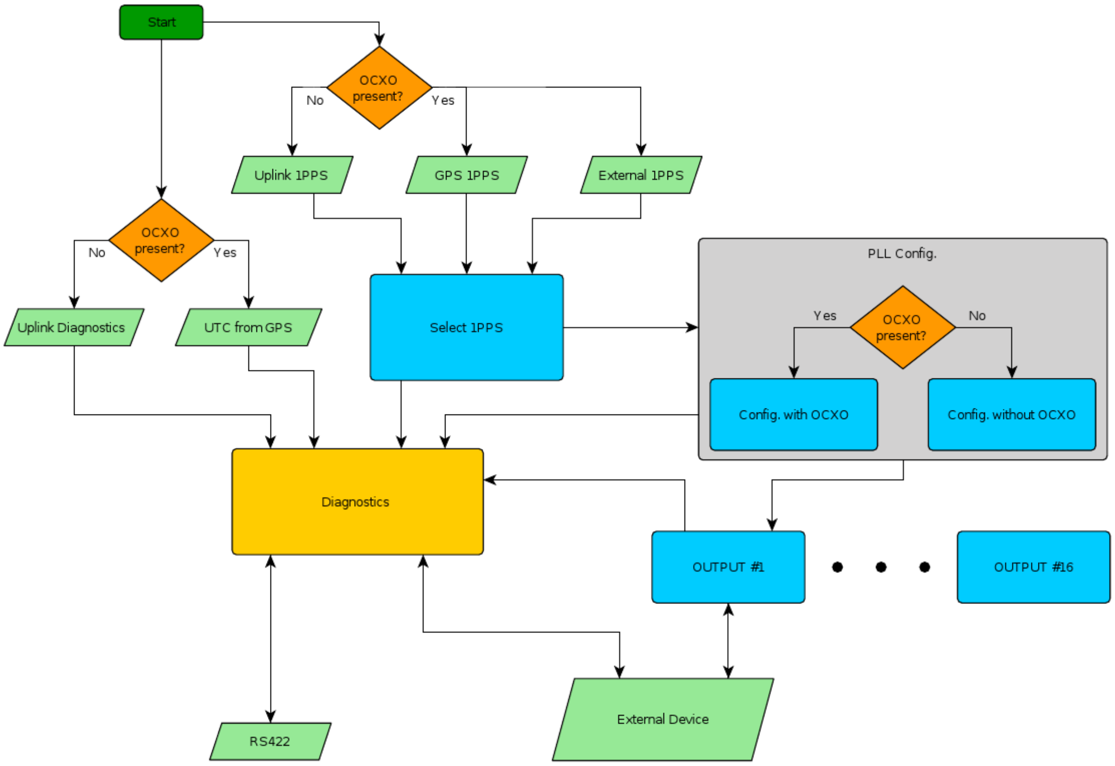

Figure 2-3: Schematic diagram of the Master and Fan-Out modules.

the system sets itself up in the case of startup or change/error in the input signals. This order is shown in Fig. 2-3. First, the system checks whether it has a built in OCXO. This determines whether it will operate as a Master (has OCXO) or as a Fan-Out (has no OXCO), and thus which inputs it will use for communication with other boards and to which inputs it locks its internal clock to.

Next, the system uses a phase locked loop (PLL) to lock its internal clock to the proper external signal. Finally, the system sends out timing information to external devices based on its locked internal clock. The whole process is being diagnosed and diagnostics information is sent upstream and downstream. Diagnostics information is eventually collected from connected boards and can be sent to an external computer.

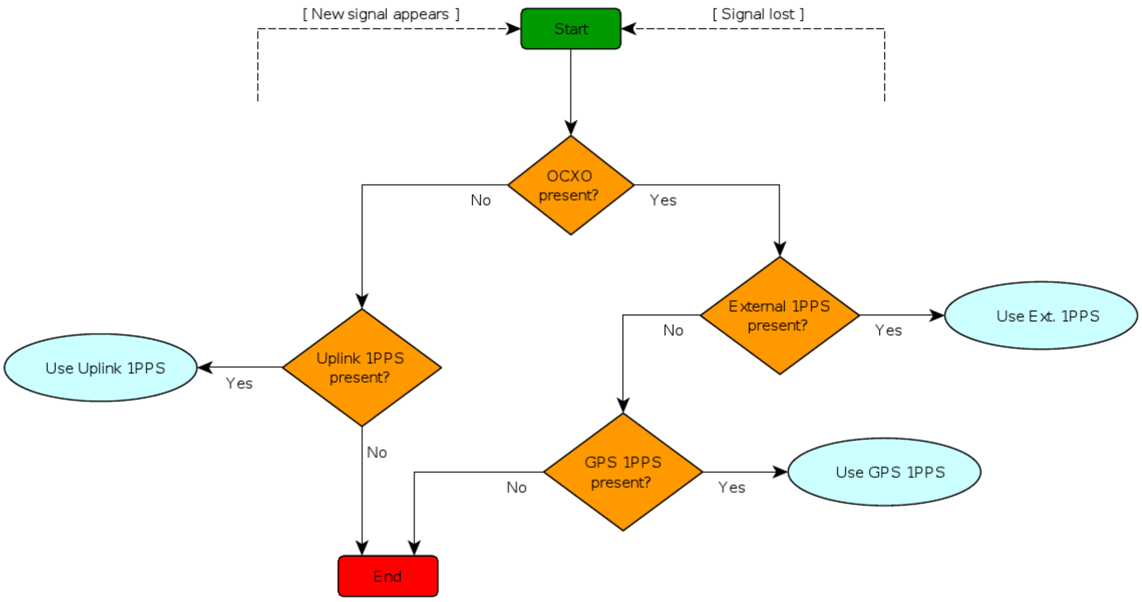

Figure 2-4: Schematic diagram of the selection of the 1PPS input signal by the Master or Fan-Out module, also shown in Fig. 2-3 as “Select 1PPS”.

2.2.6 Selection of 1PPS input

The procedure depicted in Fig. 2-4 shows the detailed operation of the “Select 1PPS” box in Fig. 2-3. It describes the procedure of how a Master or Fan-Out module selects the external 1PPS source that it uses to lock its internal clock. There is an order of preference in which the module selects the 1PPS source, if such source is present. The selection process is different for Master (has OCXO) and Fan-Out (has no OCXO) modules. After a selection is made, the module will use the selected 1PPS source until the signal from the source is lost or a new signal source becomes active. In this case the selection process is restarted. The selection process as a whole is executed in a small fraction of a second therefore it does not interfere with other processes. Changing the time source always generates a diagnostic flag.

2.2.7 Master Phase-locked Loop Configuration

Fig. 2-5 shows the process how the Master module locks its OCXO to an external reference 1PPS chosen previously by the “Select 1PPS” process, and its internal clock to the OCXO.

The Master PLL uses two internal clocks, an OCXO and a VCXO. The clock signal used in FPGA (FPGA clock) is taken from the VCXO. The signals of these two clocks, after being transformed to $\sim 8\,\mathrm{MHz}$, go to a phase detector that consists of positive-edge-triggered flip-flops with asynchronous resets and an $\underline{\mathrm{AND}}$ gate. After the phase detector, the signal reaches a filter that operates as the servo compensation, providing feedback to the VCXO to synchronize it to the OCXO. A 1PPS signal, obtained from the VCXO clock signal, is then compared to the reference 1PPS from the source previously chosen by Select 1PPS. If the difference is above threshold, the 1PPS is reset, otherwise it goes through a low pass filter and is used to lock the OCXO to the external reference by changing the applied control voltage on it.

2.2.8 Fan-Out/Slave Phase-locked Loop Configuration

Fig. 2-6 shows the process of how the Fan-Out and Slave modules lock their internal clock (VCXO) to an external reference 1PPS coming from an upstream Master or Fan-Out module (the upstream source was chosen by Select 1PPS using the fact that OCXO is not present).

The VCXO receives a similar feedback from a filter from the comparison of its clock signal to the uplink source than for the case of the Master PLL Configuration. The VCXO clock signal is then used to provide the FPGA clock. The 1PPS is based upon direct comparison to the 1PPS from the uplink source.

2.2.9 Fiber Delay Determination

Fig. 2-7 shows how the correct time shift of an output to an external device is determined. The output consists of an 8 MHz clock signal, 1PPS and diagnostics information.

After a signal is detected from the external device connected to the Output, the Master or Fan-Out module starts the transmission of the output signal (clock signal, 1PPS and diagnostics). The external device (a Fan-Out or Slave board) automatically synchronizes its internal 1PPS to the received 1PPS, and sends this 1PPS back. The Master or Fan-Out Module measures the delay of the received 1PPS from which it can determine the delay due to signal transmission time. This delay is then compensated for by sending out the 1PPS signal in advance to the internal 1PPS of the Master or Fan-Out Modules. Delay is determined 16

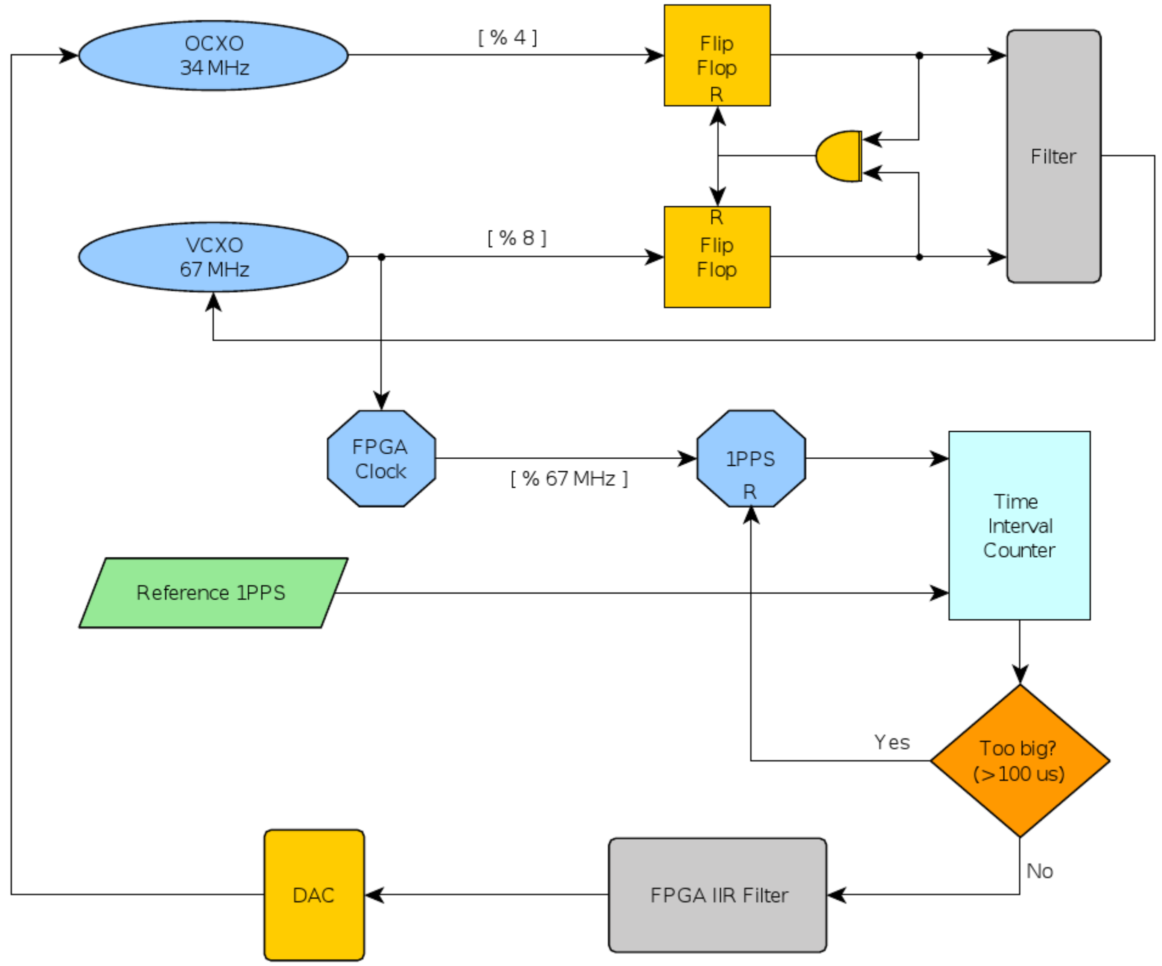

Figure 2-5: Schematic diagram of the phase-locked loop (PLL) synchronization of the Master module. This diagram is shown in Fig. 2-3 as "Config. with OCXO."

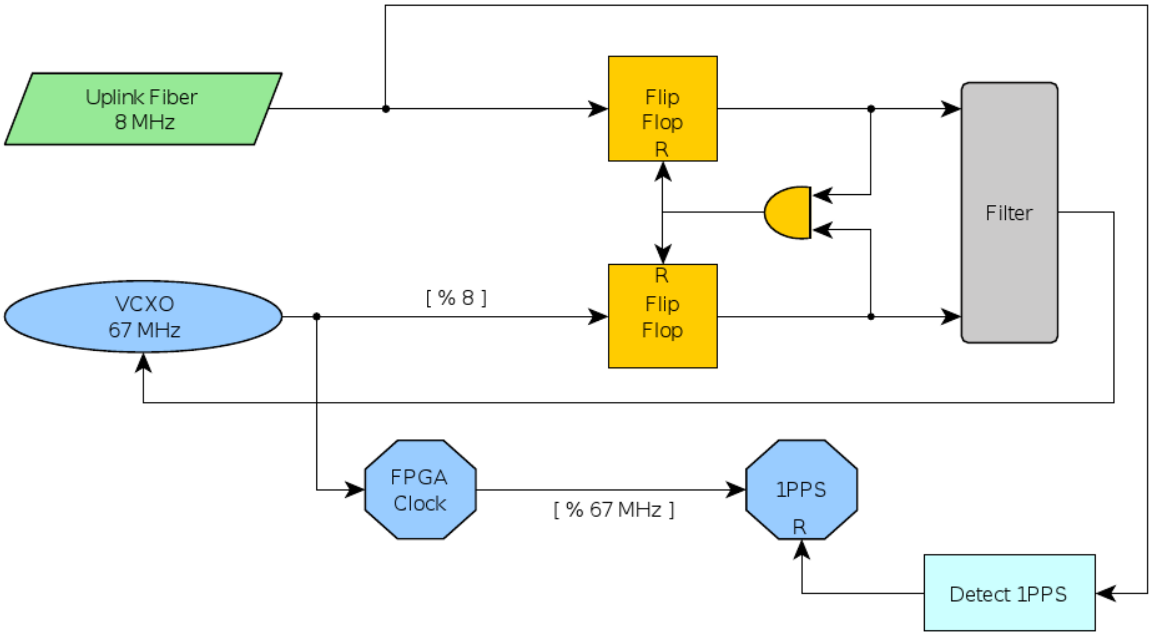

Figure 2-6: Schematic diagram of the phase-locked loop (PLL) synchronization of the Fan-Out and Slave modules. This diagram is shown in Fig. 2-3 as "Config. without OCXO."

times, using 16 seconds for each determination (except the first that takes 13 seconds). The determined value of the delay is then stored, therefore it is a fixed value after system startup, this way preventing fluctuations due to noise. In case of loss of signal, the determination of the delay restarts. This enables the change of external devices or cables without restarting the whole system.

2.2.10 Structure of the Diagnostic Output Data: Overview

Internal parameters of the Advanced LIGO Timing System are designed to accurately group all necessary information that is to be communicated to the consumer, user and/or developer. A computer interface of the Advanced LIGO Timing System (hereafter Computer) redistributes this information in order to make it easy to decipher, focusing on the requirements from the users perspective. Here we shortly outline the structure of the diagnostic data that appears on the RS422 output of the Master module every second. A detailed description can be found in [321].

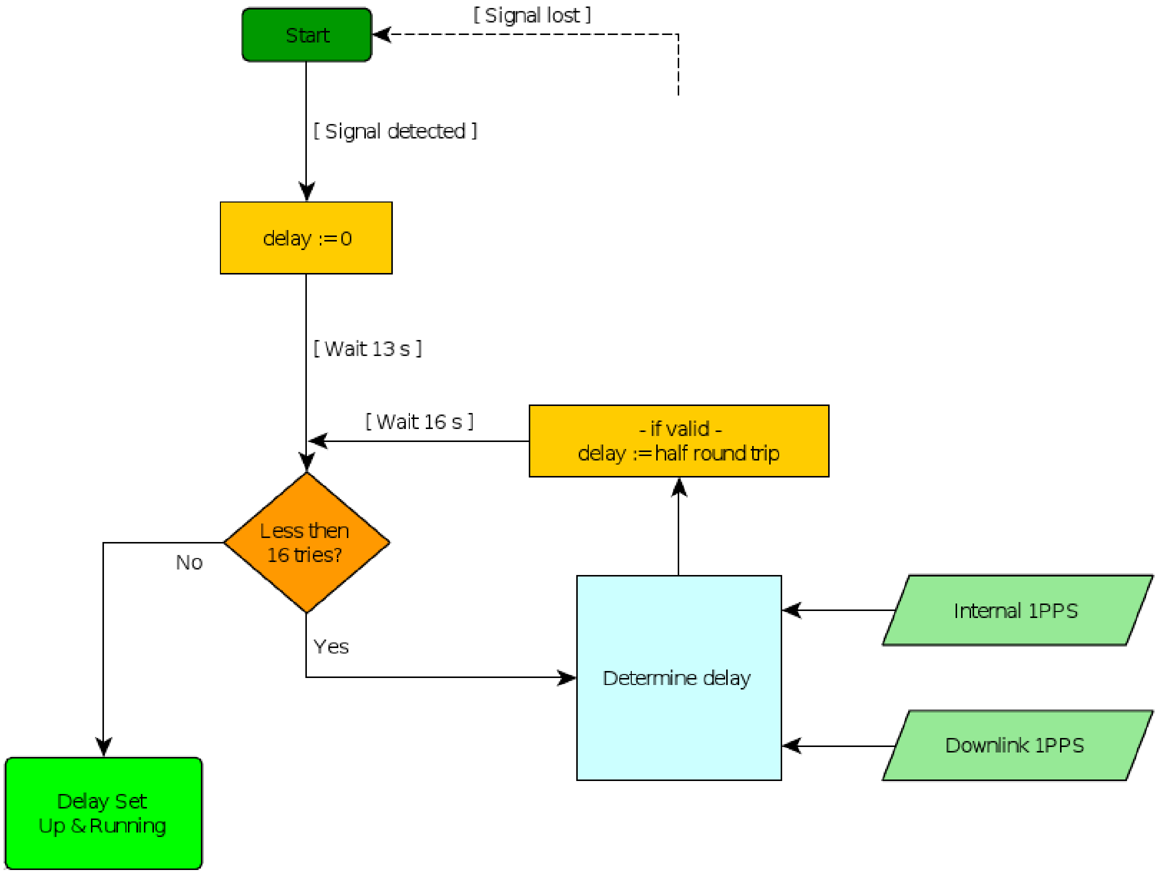

Figure 2-7: Schematic diagram of the determination of fiber delay by the Fan-Out and Slave modules. This diagram is shown in Fig. 2-3 as "Output #?."

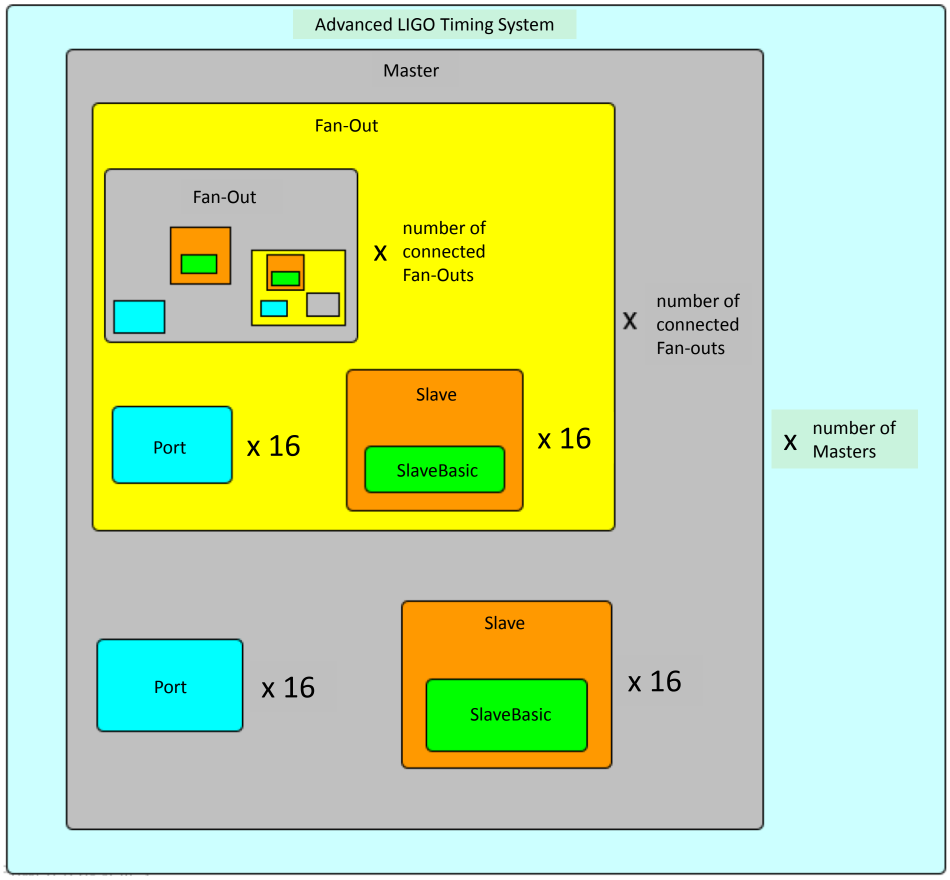

Figure 2-8: Schematic diagram showing the data structure of the Computer output.”

Since the structure of the Advanced LIGO Timing System (i.e. the architecture of the network of Master, Fan-Out and Slave modules) is not fixed, the structure of the data output also needs to be dynamic. The data structure implementation can also dynamically handle any structural changes, adapting to changes without the need to restart the system.

Data is accessible by the user in the following structure (see Fig. 2-8).

The data structure, similarly to the structure of the Advanced LIGO Timing System, is based on a hierarchical, tree-like structure. Data from an Advanced LIGO Timing System module (i.e. a Master, Fan-Out or Slave) is represented as a data unit, while other modules connected to the Advanced LIGO Timing System module are represented by data subunits. As shown in Fig. 2-8, the main data unit represents the Advanced LIGO Timing System itself. This has data subunits representing each Master. Data units representing a Master contain subunits for each Fan-Out and Slave connected to them, as well as subunits for every port (containing synchronization information). While there are 16 Slave and Port subunits independently of the number of connected modules, the number of Fan-Out subunits is equal to the number of connected modules. Note that the data units for Masters and Fan-Outs are identical, i.e. they contain identical parameters; the difference is only in the values assigned to these parameters. This identity mirrors the identity of Master and Fan-Out modules, the only difference being the presence of an OCXO and consequently the usage of the modules.

Data units represent modules and parts of the timing distribution system, as follows:

1. Advanced LIGO Timing System - represents the Advanced LIGO Timing System as a whole, containing the data units of each Master present.
2. Master / Fan-Out - represents a Master or a Fan-Out module (it also contains information on which module it represents). Besides containing the information on the module, it also contains the data modules of each Fan-Out or Slave connected to the given Master/Fan-Out, as well as a data unit for every connected port (containing synchronization information).
3. Slave - represents a Slave module. Contains information that is specific to Slave type, i.e. Fan-Out[5], Slave and DuoTone. It also contains a data subunit SlaveBasic.
4. SlaveBasic - contains the information of a Slave module that is independent of the Slave type, i.e. basic information.

2.2.11 Diagnostics

To monitor the operation of the Advanced LIGO Timing System, diagnostics information is collected from each Master module, Fan-Out and Slave module, as well as about the structure and configuration of the system as a whole. Diagnostics information is transferred every second through the optical fibers connecting the modules, along with timing information (see Figure 2-1) [321]. Data transfer is accomplished using pulse-width based binary encoding.

---

[5] Note that Fan-Out boards are also Slave boards from this perspective; therefore a Fan-Out board will have two subunits, one for its Fan-Out purposes and one for its Slave purposes (i.e. locking to another Fan-Out or a Master).

It utilizes the fact that only the positive edges of the 2^{23} Hz square-wave clock signal are used for synchronization purposes, leaving the negative edges available to carry additional information. Information bits are therefore encoded by shifting the negative edges by a quarter-cycle. Negative and positive shifts are both used to represent '1' bits, while no shift represents '0' bits. To account for the fiber receiving circuit's AC-coupling and to preserve DC-balance, positive and negative shifts are used one after the other for '1' bits. The only exception is the 1 second mark, which is differentiated from other information by having two consecutive '1' bit signs with the same shift (see [320] for further information on data encoding).

Data is collected by each Master and Fan-Out module from all downstream components, and is sent to a computer using RS422 or ethernet connection (see Figure 2-1). Assigned addresses of modules are used to construct a map of the physical fiber connections between modules. Diagnostics information further includes status and configuration information for each module. If needed, one can also send information to each module from a computer interface. Note that status information, besides signaling whether the system is up and running, also includes information on every error, e.g. temporary loss of signal, the time compensation applied for each connection due to delay in fiber, etc. For further information on data structure and processing, see [321].

2.3 Performance and Tests

As discussed above, the Advanced LIGO Timing System is required to provide $\mathcal{O}(\mu s)$ timing synchronized throughout a detector, as well as between different detectors. Besides the internal precision of the system, this microsecond precision needs to include the uncertainty introduced by communication with external devices, i.e. timing reconstruction using the DuoTone signal output. Of further importance is the Timing System's robustness against environmental and structural changes. In the following we present several test results that show the system's performance.

The Advanced LIGO Timing System transfers timing information using a modular system, each module is synchronized to its upstream module. To demonstrate proper synchronization of the entire system, we tested the synchronization between the two ends of a typical modular configuration including all elements. The configuration took its input timing 1PPS from a UTC GPS receiver. A Master module was connected and synchronized to this GPS 1PPS. A Fan-Out module was connected to the Master module, and a Slave module to the Fan-Out module. The Master and Fan-Out modules were connected with a 4 km long optical fiber, that allows for testing long distance-synchronization, as well as being the realistic setup for Advanced LIGO. We tested the synchronization of this GPS-Master-Fan-Out-Slave module network by comparing the 1PPS output of the Slave module to the GPS 1PPS. Conducting a 24 hours long measurement, we obtained a median of 14.3 ns and a 99% confidence interval of 6.2 ns (with maximum of 24 ns and minimum of 10.5 ns), showing that the uncertainty of internal synchronization is a small part of the total allowed error budget of 1 μs[6].

Some external devices require a DuoTone signal for sub-second time stamping or diagnostics. To determine the precision of this time stamping, we compared the 1PPS signal reconstructed from the DuoTone signal and the actual 1PPS signal. We conducted an ~ 9 days long measurement, calculating the difference between the reconstructed and actual 1PPS signals once every hour. The obtained time difference was $\Delta t = -263 \pm 2\,\mathrm{ns}$. This result demonstrates that the DuoTone signal can be used to precisely reconstruct the timing information.

Besides timing precision, the Advanced LIGO Timing System is also capable of quickly re-synchronizing itself if one changes its configuration by disconnecting or connecting some of its modules. To test this property, we used the configuration used for testing internal synchronization, i.e. a Master-(4km fiber)-Fan-Out-Slave module chain. After allowing the system to synchronize, we power cycled the Master module (twice) and then the Slave module. The results can be seen in Figure 2-2 (b). After restarting the Master module, the system re-acquired precise timing in about 3 minutes. This time frame is due to the low pass filter applied in synchronizing the Master module's OCXO. After restarting the Slave module, the system re-synchronized in about 20 seconds which is the time it takes for the FPGA chip on the board to reboot itself and the time of measuring the signal time delay in the fiber that connects the Slave module to the rest of the timing system. We note that the

---

[6] For comparison, the initial LIGO phase uncertainty was equivalent to a few microseconds (dominated by calibration, and not timing, uncertainties), with $\mathcal{O}(\mu s)$ variation during scientific data taking periods [338, 339]

same reboot durations apply for components that are newly connected to the system. This measurement demonstrated that the system is robust against power cycling or disconnection of its components, which provides additional safety and easy access to the system, enabling the quick addition and/or removal of elements.

2.4 Summary

The Advanced LIGO Optical Timing Distribution System provides UTC synchronized time-stamping throughout the Advanced LIGO detector, as well as to a network of detectors to sub-microsecond precision in hardware. This accuracy guarantees that uncertainties in arrival time and direction reconstruction will be unaffected by synchronization uncertainties. Sub-microsecond precision also enables a possible 1% amplitude and 1° phase calibration of the Advanced LIGO detectors. The self-diagnostics system of the Advanced LIGO Timing System allows for remotely monitoring status and structural information that enables the traceability of the modular structure, as well as possible errors. We demonstrated that the Advanced LIGO Timing System robustly recovers after power cycling or after the (dis-) connection of components.

Chapter 3

Observational Constraints on Joint Sources of Gravitational Waves and High Energy Neutrinos

3.1 Bounding the time delay between gravitational waves and high energy neutrinos from GRBs

This section, following Baret et al. [238], describes the possible time delay between GW and HEN signals arriving from a GRB.

Previous single or multimessenger searches for GWs, HENs and/or (electromagnetically detected) GRBs have defined various different time windows. Aso et al. [333] designed a GW+HEN multimessenger search algorithm and investigated possible time windows from 0.1 s to up to 1 day. In a search for HEN counterparts of detected GRBs, Abbasi et al. (IceCube Collaboration) [340] considered three different time windows around each burst. The first time window covered the observed prompt gamma-ray emission, expecting prompt neutrino emission to overlap with prompt gamma-ray emission. The second considered time window covers neutrino-producing processes before gamma-rays can escape from the fireball. This time window is taken to be 100 s immediately preceding the prompt emission time window. Abbasi et al. (IceCube Collaboration) [340] also considered a generic time window that was chosen to be much wider than the previous two to include possible unknown mechanisms. This third time window was chosen to be $[-1\text{h}, 3\text{h}]$ around the start of the prompt emission, a compromise between including unknown mechanisms and keeping the HEN background relatively low.

In a HEN search for GRB 080319B, one of the brightest GRBs ever observed, the IceCube Collaboration [341] uses two time windows for HEN detection. A shorter time window of 66s was used that overlapped with the GRB's prompt gamma-ray emission. Another, $\sim$ 300s long extended time window was also analyzed. Data from the detector was only available in this 300s around the GRB which motivated the choice of this time window.

Very recently a search for neutrinos from 117 GRBs was conducted using data from the IceCube detector's 40-string configuration [342]. Two different searches were performed; one model independent search, using no model for the energy distribution of HENs from GRBs. This search used a time window of ±24 hours around the burst. The second, model dependent search used the predicted energy distribution from GRBs by Guetta et al. [14]. This search considered the observed start (T_{start}) and stop (T_{stop}) times of gamma-ray emission from each GRB. A probability distribution was assigned for expected neutrino times with uniform probability between T_{start} and T_{stop}, and with Gaussian tails around this uniform window. The width of the tails was chosen to be $T_{stop} - T_{start}$, and was constrained to at minimum 2 seconds and at maximum 30 [342].

In GW burst searches triggered by long and/or short GRBs, performed with the LIGO-Virgo GW network, [343, 344, 241, 345], a time window of $[-120\text{s}, +60\text{s}]$ was used around the GRB trigger. This time window is longer than the duration of most analyzed GRBs. It was also chosen to include models predicting gamma-ray emission up to 100s after initial GW emission (e.g. [346]), as well as measurement uncertainties in GRB trigger time. For a search for GW inspiral counterparts of detected short GRBs, Abadie et al. (LIGO Scientific Collaboration and Virgo collaboration) [347] used a time window of $[-5\text{s}, +1\text{s})$ around the trigger time of GRBs, aiming to capture "the physical model with some tolerance for its uncertainties."

The analysis of the GW+HEN coincidence time window described below mainly relies on model-motivated comparisons with observations and simulations. We consider different types of information we have on GRBs from their detected electromagnetic radiation, and infer to the plausible time frame of GW or HEN emission based on this information. We use observations by BATSE [3], Swift [4] as well as Fermi LAT [348]. We estimate the duration of different emission epochs, and combine them to obtain an overall time window. While a joint search for GW and HEN signals mainly aims to detect astrophysical sources with unobserved electromagnetic (EM) counterpart, we constrain their emission based on the emission of detected sources, assuming that these two types have similar emission.

Below we discuss the different emission processes with special emphasis on their relative timing, defining their contribution to the GW+HEN coincidence time window.

3.1.1 Gamma-ray Emission

The observed temporal structure of gamma-ray emission from GRBs can be used as the foundation in the description of the temporal structure of GW and HEN emission. For the purposes of GW+HEN analysis, we define a practical upper limit for GRB duration as the 95% quantile of the T_{90}'s of GRBs detected by the Burst Alert and Transient Source Experiment (BATSE). We obtain this limit using data from the 4th BATSE GRB catalog (1234 GRBs, [3]), that includes 1234 GRBs with duration information (see Figure 3-1). As the measure of GRB durations, we use their T_{90}, the time interval in which the integrated photon counts from a GRB in the BATSE detector increased from 5% to 95%. See Figure 3-1 for the distribution of T_{90}'s of BATSE GRBs in comparison with t_{95}^{GRB}. The obtained duration upper limit is

$$t_{95}^{GRB} \simeq 150 \text{ s} \tag{3.1}$$

For comparison we note here that the 90% and 99% quantiles are $t_{90}^{GRB} \simeq 100$s and $t_{99}^{GRB} \simeq 300$s. Considering a similar analysis for GRBs detected by the Swift satellite (534 GRBs, [4]), we find that 87% of Swift GRBs have $T_{90} \lesssim 150$s. For Swift, the 90%, 95% and 99% quantiles are 180s, 300s and 500s, respectively. See Figure 3-1 for the distribution of Swift T_{90}'s.

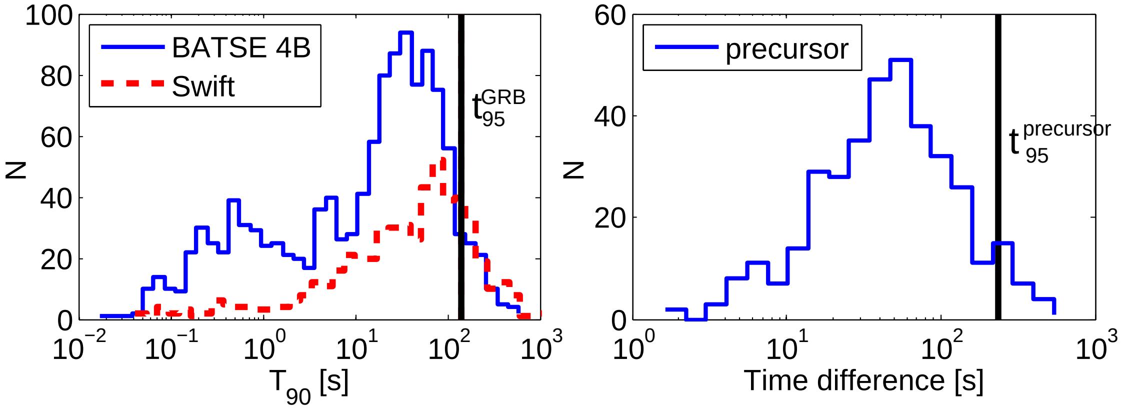

Figure 3-1: (left) Distribution of T_{90}'s for GRBs measured by BATSE (straight line, 1234 GRBs, [3]) and Swift (dotted line, 534 GRBs, [4]). The vertical line shows t_{95}^{GRB}, i.e. the 95% quantile of the T_{90}'s of BATSE GRBs. (right) Distribution of time difference between the onset of a precursor and the onset of the main GRB. The vertical line shows $t_{95}^{precursor}$, i.e. the 95% quantile of the time differences (the delays were obtained by Burlon et al. [5] using data from BATSE [3]).

3.1.2 High-energy Gamma-ray Emission

While typical gamma-ray energies from GRBs are in the range of $0.1 - 1$ MeV, some GRBs also emit gamma-rays with energies above 100 MeV (e.g. [349, 350]). Such high-energy component was first observed by the Energetic Gamma-Ray Experiment Telescope (EGRET, e.g, [351, 352, 353]), and has recently been identified for more than 20 GRBs [354] by the Large Area Telescope (LAT) on the Fermi satellite [348]. GeV gamma-ray emission from these GRBs, in most cases, shows radically different characteristics [349, 350, 355] compared to MeV gamma-ray emission.

The different temporal and spectral behavior of GeV photons imply that they are likely produced by different processes during a GRB than MeV photons. There are different proposed mechanisms responsible for the creation of GeV photons. It is also possible that different mechanisms are responsible for the GeV photon output for different GRBs. Studying the high energy emission of GRB 090510, Ghirlanda et al. [356] suggested that this may be explained entirely due to external shock emission. On the other hand, several other authors [357, 358, 359] have shown that internal shocks may also play a role, especially during the first few seconds of the high-energy tail. Toma et al. [360] argue that GeV photon emission can be due to Compton upscattered photospheric emission, during which photons are upscattered by electrons in internal shocks. Photohadronic interactions in proton-dominated bursts have also been considered, that may be responsible for the production of the high-energy component [361, 362]. In this case, GRBs with GeV photon emission can be excellent sources of HENs. In the more standard Waxman-Bahcall model, however, GeV emission, associated with higher Lorentz factor, results in decreased HEN emission (e.g. [341]). See e.g. [349] for a summary of possible emission mechanisms.

Due to the small number of detected LAT GRBs, as well as our limited understanding of the emission mechanisms, investigating the temporal behavior of high-energy gamma-ray emission is difficult. It seems, however, that in many cases the light curves follow a power-law decay in time: $F_{LAT} \propto t^{-\alpha}$ with $\alpha \simeq 1.5$ [355, 363, 364], while the rising parts for some cases are consistent with $F_{LAT} \propto t^2$. We note that the characteristic rising and decay were observed both for short and long bursts [355].

For the purposes of GW+HEN analysis, we are interested in the proportion of high-energy photons emitted in a given time window, T, following the onset of the GRB. For this estimate, following [356], we model the temporal distribution of high-energy photons with a smoothly broken power law

$$F_{LAT}(t) = \frac{A(t/t_b)^{\alpha}}{1+(t/t_b)^{\alpha+\beta}} + B \tag{3.2}$$

with $\alpha = 2$ and $\beta = 1.5$ as discussed above. The peak emission is at time $t_{peak} = t_b(\alpha/\beta)^{1/(\alpha+\beta)}$. A is an amplitude and B is the background level, both irrelevant for the calculation of the temporal behavior (for simplicity, we will assume $B = 0$).

Due to the low number of available data, we restrict our analysis to estimating the ratio of GeV photons arriving in the 150s time window, i.e. the GRB emission time window described above in Section 3.1.1. Following [355], we use 8 out of the 12 GRBs for which the detected GeV emission has high enough signal-to-noise ratio for the reconstruction of the temporal structure. We assume that the emission of these GRBs follow Equation 3.2, with t_{peak} equal to the maximum shown in [355]. Taking all 8 GRBs into account with equal weights, we verify that $\sim 90\%$ of the GeV photons arrive within a 150s time window after the onset of the GRB (see Figure 3-2). For comparison, 50% of the photons arrive within $\sim$ 7s, while 95% of the photons arrive within 650s. We conclude that the 150s time window is a reasonable upper bound for the high-energy gamma-ray emission as well. We note that the obtained time window does not depend significantly on the initial rising part. The important factors are the peak time and the slope afterward.

We note that, while the majority of GeV photons seems to arrive within the first 150s after the onset of the GRB, the importance of detected GeV photons from the perspective of neutrino emission can be that it might indicate a process, such as external shocks, that can produce HENs. If in such process the emission of GeV photons is not proportional to the emission of HENs (i.e. if the durations of the arrival of $\sim 90\%$ of GeV photons and HENs are different), the duration of HEN emission might be longer than 150s.

3.1.3 Gravitational-wave Emission

While gamma-ray and HEN emission from GRBs are practically independent from the specific mechanisms driving the (varying) relativistic outflow[1], GW emission is closely connected to the central engine.

Various mechanisms can result in the emission of GW transients. Here we first consider stellar core collapses, the likely progenitors of at least some long GRBs. For these the collapse of the rotating iron core, as well as the following rebound in the inner core instantly produce a GW burst lasting for tens of milliseconds (see e.g. [365]). Other mechanisms following core bounce can also emit GWs shortly, within a few seconds after the collapse. These processes include rotational non-axisymmetric instabilities, post-bounce convection, standing-accretion-shock instability (SASI), or non-radial proto-neutron star pulsation [365].

The collapse results in the formation of a protoneutron star, that can further collapse to form a stellar-mass black hole (e.g. [366] and references therein). The rotating, collapsing core might also fragment into two or more compact objects, whose coalescence can emit strong GWs [367, 368]. After the formation of a black hole, weaker GW emission is possible from accreting matter around this central black hole that can fragment due to gravitational instability. The resulting black hole - fragment binaries can emit GWs detectable by Earth-based GW interferometers [367, 369, 370, 97]. For high enough accretion disk masses, the self-

---

[1] The distance from the central engine at which observable gamma-rays and HENs are produced is much larger than the central engine (e.g. [8]).

gravity of the disk can result in gravitational instabilities such as spiral arm or bar formation, emitting GWs (e.g. [371], [372] and references therein). Non-uniform, non-axisymmetric accretion can also deform the central black hole that will emit gravitational waves during its ring-down [372]. Such GW emission processes can last for the duration of the accretion, i.e. possibly the duration of the GRB.

Compact binary coalescence, the likely progenitor of short GRBs, is anticipated to be strong GW emitters in the sensitive frequency band of Earth-based GW detectors (e.g [347, 373, 372]). Double neutron stars, black hole-neutron star binaries and black hole-white dwarf binaries are considered as possible sources (e.g. [372]). Most of the GW output of such sources is emitted in the form of a very short, $\sim$ 1ms long transient (e.g. [374, 372]). Furthermore, many short GRBs occur at low redshifts [375], increasing their significance as potential GW (and HEN) sources.

Based on the models discussed above, GRBs are expected to be strong emitters of GWs. While core-collapse and binary merger are expected to emit the strongest GW transient, emission is possible during the entire duration when the central engine is active (see Figure 3-2). GW emission can consist of either one or more short burst (e.g. due to core collapse or the infalls of fragments of the accretion disk [369, 370, 97]), or longer duration GWs (e.g. due to the emission of rotational energy [371]). If the central engine consists of an accretion disk, the activity of the central engine coincides with the emission of GWs.

3.1.4 High-energy Neutrino Production

In a GRB, according to the internal shock model, HENs and gamma-rays are expected to be produced due to the variability of the central engine's activity, that results in fluctuations of the relativistic outflow, creating internal shocks in the ejecta [8, 376, 14, 377, 378, 379] (note that other, alternative emission models also exist; see Section 1.4.1. Below we will focus on the internal shock model). These internal shocks accelerate electrons and protons in the outflow through the process of Fermi acceleration. Shock-accelerated electrons radiate their energy through synchrotron or inverse-Compton radiation (e.g. [378, 380]), emitting gamma-rays. Shock-accelerated protons interact with gamma-rays ($p\gamma$) as well as with other, non-relativistic protons (pp), producing charged pions and kaons [301]. Pions and kaons from these processes decay into HENs through [9]

$$\pi^{\pm}, K^{\pm} \rightarrow \mu^{\pm} + \nu_{\mu}(\overline{\nu}_{\mu}) \tag{3.3}$$

The resulting muons can further decay through, e.g., the process $\mu^{+} \rightarrow e^{+} + \nu_e + \overline{\nu}_{\mu}$. Nevertheless, these muons may undergo radiative cooling, which would suppress neutrino production from this muon decay [9, 381, 178]. For the proton energy range $E_p \approx 10^4 - 10^{5.2}$ GeV the $p\gamma$ process dominates HEN production, while outside of this energy range the pp process is dominant [301].

Since internal shocks in the relativistic outflow result in both gamma-ray and HEN emission, HENs are expected to be produced during the emission of gamma-rays (see Figure 3-2). We note here that, since efficient neutrino production requires significant target density of radiation and/or particles, typical HEN production is likely to happen close to the central engine and during the highest gamma-emission phase, when the engine is the most active.

For the case of long GRBs created by core-collapse supernovae, internal shocks in the relativistic outflow can occur even before the outflow emerged from the stellar envelope, therefore HENs are also expected to be produced before observable gamma-ray emission [178, 185]. While gamma rays emitted in this early phase cannot escape from the star due to its large optical depth, neutrinos have much longer mean free paths and may therefore pass through the stellar envelope. This pre-GRB neutrino emission is expected to precede the start of gamma-ray emission by up to 100s [178, 185] (see Figure 3-2).

GRB afterglows are not considered here as a part of the coincidence time window. Afterglows are produced by the relativistic jet driven into the surrounding medium (e.g. [380]), although some far-ultraviolet and X-ray flashes in the afterglow may be due to the late activity of the central engine [206]. The observed radiation, similarly to the case for prompt gamma-ray emission, is produced by synchrotron emission of shock-accelerated electrons. The energy distribution of protons is expected to be similar to that of electrons [380], therefore the softer emission spectrum of afterglows indicate that protons might also be of lower energy. These protons would need higher energy gamma-rays to produce neutrinos[2], that are scarcely present in the afterglow spectrum.

---

[2] In photomeson interactions producing HENs, the photon's energy ϵ_γ and the proton's energy ϵ_p are related,

We note that a few ultra high-energy neutrinos (UHENs) of energies $\sim 10^8 - 10^9$GeV might be emitted during the afterglow phase [202, 380, 382, 206, 383], if GRBs can accelerate some protons to energies $\epsilon_p \sim 10^{11}$GeV. In our time window estimation, we do not take into account such emission from the afterglow.

3.1.5 GRB Precursors

Gamma-ray bursts are sometimes preceded by fainter, softer electromagnetic emissions, so-called precursors (e.g. [384]). The underlying mechanism(s) creating these precursors is yet unknown. They have been detected for about $8 - 20\%$ of GRBs [384, 385, 5, 386], with some GRBs apparently having multiple precursors. It is expected, however, that a higher percentage of GRBs are preceded by precursors, as many of these might be missed due to, e.g., beaming, low signal-to-noise ratio, the proximity of the precursor and the main event, or the definition of what is considered a precursor [384].

Analyzing precursors detected by BATSE, Lazzati [384] finds that the net count of a precursor, a value connected to the energy of the events, is up to about 1% of the main burst, most precursors having non-thermal spectra. Burlon et al., using a more detailed analysis of data from the Swift telescope [385] and BATSE [5], finds that precursors, on average, emit $\sim 30\%$ (for Swift) and $\sim 10-20\%$ (for BATSE) of the energy of the main burst. Burlon et al. find that precursors and main events have very similar spectral properties, concluding that precursors and main GRBs are likely to be produced by the same underlying mechanism.

There are several different GRB precursor models in the literature (e.g. [5]). The "two-step engine" model [387] argues that precursors are produced by initial weak jets, that are created by and coincide with the actual core collapse. The "progenitor precursor" model (e.g., [388]) connects precursors with isotropic emission marking the jet breakout. The "fireball precursor" model [389] considers a simple model of an isotropic, post-acceleration GRB with constant rest mass and kinetic energy.

Depending on the considered model, either or both the precursor and main GRB can have GW and/or HEN emission. While not all of the models result in such emissions, due to

---

at the threshold of the Δ-resonance, by

$$\epsilon_\gamma \epsilon_p = 0.2\mathrm{GeV}^2\Gamma^2 \tag{3.4}$$

in the observer frame, where Γ is the bulk Lorentz factor of the outflow [380].

our lack of understanding of the underlying mechanisms responsible for precursor emission, we consider them as potential GW+HEN emitters in our conservative time window upper limit. The potential detection of HENs prior core-collapse/bounce GW emission from a joint source therefore can be an indicator of such precursor activity; an example when the temporal structure of joint emission can shed light on the underlying mechanisms.

We note that, while the models above are concerned with precursors from stellar core collapses, precursor emission has also been identified from short GRBs [386].

We estimate an upper bound for the time difference between the onset of a precursor and the onset of the main burst using the results of Burlon et al. [5]. Burlon et al. analyzed 2121 BATSE GRBs, out of which 264 (12.5%) was found to be preceded by one or more precursors (in total 369 precursors). From this data, we determine an upper bound $t_{95}^{precursor}$ to the time difference between the start of the precursor and the main burst, which is the 95% quantile of precursor time differences measured between the onset of the precursor and of the main GRB, as calculated by Burlon et al. Figure 3-1 shows the distribution of the time differences and the 95% quantile, for which we obtain (also see Figure 3-2)

$$t_{95}^{precursor} \simeq 250 \text{ s} \tag{3.5}$$

For comparison, we note here that $t_{90}^{precursor} \simeq 150\text{s}$ and $t_{99}^{precursor} = t_{max}^{precursor} \simeq 350\text{s}$. We use $t_{95}^{precursor}$ as the upper limit of time difference between the main burst and a precursor.

For the main GRB above, we used an upper limit of $\sim$ 100s for the time difference between the activation of the central engine and the onset of observable gamma-ray emission. We will use the same delay upper limit for precursors, i.e. the delay of the onset of gamma/X-ray emission from the precursor is estimated to be less than 100s after the start of the central engine (see Figure 3-2).

3.1.6 Summary

A summary of the considered emission processes and their time frames are shown in Figure 3-2. Note, that for the case of GW emission, a time frame possibly having GW signals means that there can be one or more short transients at any time of the time frame. There can also

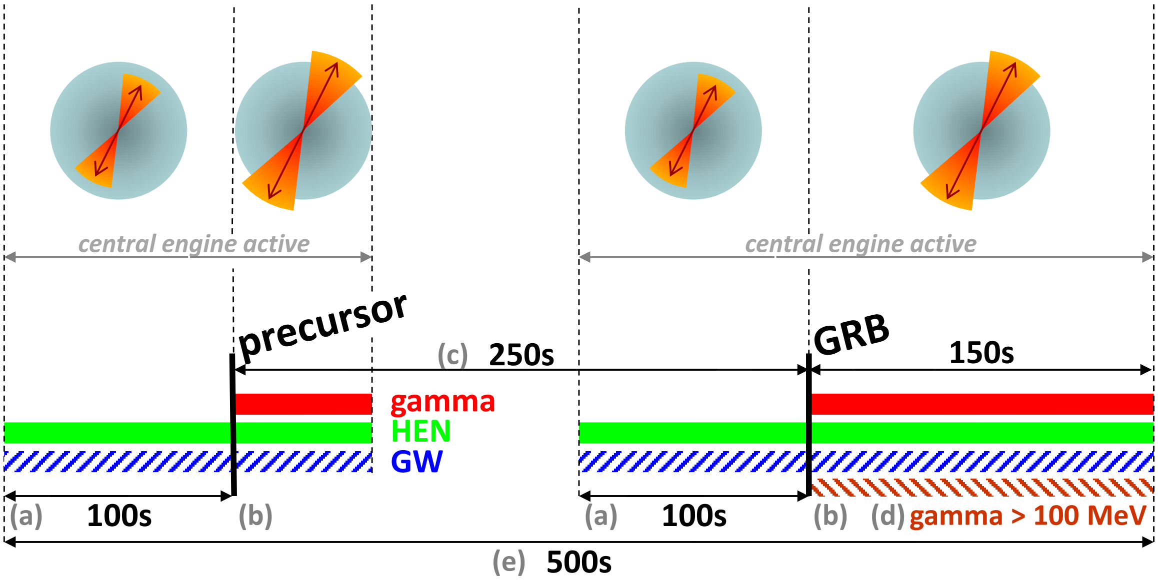

Figure 3-2: Summary of upper bound of GRB emission process durations taken into account in the total GW+HEN coincidence time window. (a) active central engine before the relativistic jet has broken out of the stellar envelope; (b) active central engine with the relativistic jet broken out of the envelope; (c) delay between the onset of the precursor and the main burst; (d) duration corresponding to 90% of GeV photon emission; (e) time span of central engine activity. Overall, the considered processes allow for a maximum of 500s between the observation of a HEN and a GW transient, setting the coincidence time window to $[-500\text{s}, 500\text{s}]$. The time window for GW or HEN signals from the onset of the GRB is $t_{GW} - t_{GRB} \approx t_{HEN} - t_{GRB} \in [-350\text{s}, +150\text{s}]$. Note that we show a period between the end of the precursor emission and the start of the main GRB with no GW or HEN emission. While we cannot exclude the possibility of GW or HEN emission in this period, such emission would have no effect on our estimated time window. The top of the figure shows a schematic drawing of a plausible emission scenario.

be a longer GW emission during this time (see Section 3.1.3 for further details).

- We start with the onset of gamma-ray emission from the main GRB. The duration of the main GRB is, in 95% of cases, shorter or equal than 150s (see Section 3.1.1). During this time frame, as the central engine needs to be active, both HEN and GW emission is possible.

- Recent Fermi/LAT observations (e.g. [349, 350]) have shown that at least some GRBs also emit high-energy (GeV) gamma-rays, with temporal structure different from that of gamma-rays of typical energies (see Section 3.1.2). Our estimated time scale of the emission shows that most ($\gtrsim 90\%$) of the high-energy photons are expected to be detected within 150s after the onset of the GRB.

- GW and HEN emission can commence up to 100s before the onset of gamma-ray emission (see Section 3.1.4) due to the time it takes for the relativistic jet to break out of the star (e.g, [178]). The central engine is active during this time, for the jet needs to be actively driven in order to advance.

- Precursor emission can begin up to $t_{95}^{precursor} \simeq 250$s prior to the onset of the main GRB (see Section 3.1.5). Since a precursor can be active practically any time within this time frame, and since the activity of the central engine is a prerequisite of precursor emission, both HEN and GW emission is possible during this period.

- The activity of the central engine responsible for a precursor can begin up to 100s before the onset of gamma/X-ray emission by the precursor (see Section 3.1.5). During this time, as the central engine is active, both HEN and GW emission is possible.

- We note that our choice for the GW/HEN coincidence window is not affected by what happens in between the precursor(s) and the main GRB. Since HEN and/or GWs may be present both at the precursor and during the main GRB, the GW/HEN coincidence window needs to extend anyway from the precursor up to the end of the main event. Thus, such a choice also covers the case in which GWs and/or HEN are also emitted between the precursor and the main GRB.

Considering the processes described above, we obtain a time frame of 500s during which both HEN and GW emissions are possible. This means that the difference between the arrival time t_{HEN} of a HEN and the arrival time t_{GW} of a GW transient from the same GRB is within the upper bound (i.e. time window) of

$$t_{HEN} - t_{GW} \in [-500\text{s}, +500\text{s}] \tag{3.6}$$

Note that multiple HEN (or GW) signals from a given source should arrive within a 500s time window.

We emphasize that the above time window is an estimated upper bound for GRBs. While the emission mechanisms considered are connected to the progenitor associated with long GRBs, short GRBs likely have shorter emission span and are therefore also bound by this time window. Also, we exclude potential GW/HEN emission from GRB afterglows from the time window (the emission of ultra-high energy ($\approx 10^8 - 10^9$GeV) neutrinos may be more extended; see Section 3.1.4). Other effects, such as some predicted by different Quantum Gravity models (e.g. [390]), can introduce additional time delay between different messengers. Searching for such effects may require larger time windows [390].

The processes considered above can also be used to set an upper bound on time window of GW or HEN signals coincident with an observed GRB. If the onset of a GRB is detected at t_{GRB}, both GW and HEN signals are expected to arrive within the time window

$$t_{GW} - t_{GRB} = t_{HEN} - t_{GRB} \in [-350s, +150s] \tag{3.7}$$

3.2 Observational constraints on multimessenger source population

In this section, following Bartos et al. [13], we interpret and combine previously published and independent GW and HEN observational results, to derive the first joint constraints on the rates of GW+HEN sources. We first discuss constraints from individual HEN and GW searches, and then combine these to derive upper limits on GW+HEN sources. We finally estimate projected constraints on GW+HEN sources with future detectors and joint GW+HEN searches.

3.2.1 Upper limits from neutrino observations

— Abbasi et al. [7] searched for transient point sources with the partially constructed IceCube detector in its 40-string configuration (hereafter IceCube-40) for over 1 year. The search covered the northern sky with various emission time-scales; no evidence for transient sources was found. With a conservative time window of 500 s for HEN emission from GRBs ([238]; see Section 3.1), 3 spatially coincident neutrinos in this analysis would have been sufficient for a

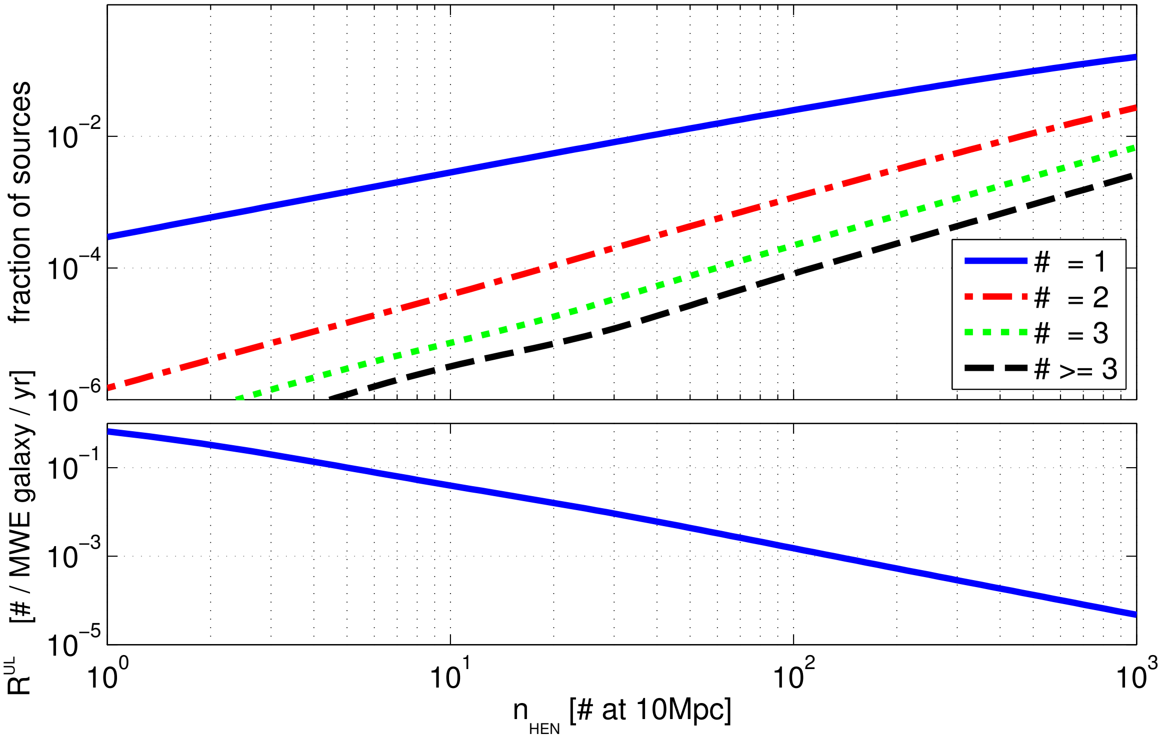

Figure 3-3: (Color online) **Top:** fraction of neutrino-emitting sources within 1 Gpc which would be detected with 1, 2, 3, or ≥ 3 neutrinos, as a function of n_{HEN} (the mean number of detected neutrinos from a source at 10 Mpc) for a detector with northern sky coverage (e.g. IceCube). Only sources are considered that emit neutrinos towards the Earth. **Bottom:** source population upper limit R^{UL} as a function of n_{HEN}, assuming a beaming factor of $f_b = 14$, and considering only the northern sky.

(5σ) discovery (even with the higher event rate of IceCube-86, three coincident neutrinos will remain a highly unlikely outcome from the background). We therefore estimate the source population upper limit as the maximum source rate that has $\lesssim 90\%$ probability to result in at least one occurrence of ≥ 3 coincident neutrinos in a time window of 500 s during a 1-year measurement.

We model the source population as following the blue-luminosity distribution of galaxies [391]: (i) for up to 40 Mpc, we take the blue-luminosity distribution given in the Gravitational Wave Galaxy Catalog [250] (we note that any incompleteness in the galaxy catalog makes our upper-limits conservative.); (ii) for larger distances (up to 1 Gpc) we adopt the homogenous blue-luminosity density from Blanton et al. [392]; (iii) we assume that IceCube is uniformly sensitive to sources in the northern sky only, which is a reasonable approximation of the detector's directional sensitivity [7]. Our upper-limits are calculated as a function of $n_{\rm HEN}$, defined as the average number of detected HENs from a source at 10 Mpc (e.g. [178]). This representation is independent of specific neutrino emission models or detectors, however its conversion to isotropic-equivalent neutrino luminosity L_ν^{iso} depends on the neutrino spectrum, duration of emission (t_0), and detector sensitivity. Writing $L_\nu^{iso} = \kappa n_{\rm HEN} t_0^{-1}$, we estimate the conversion factor for IceCube-40 [7, 393] as $\kappa \approx 1.5 \times 10^{49}$ erg for high-luminosity (HL) GRBs [differential spectrum $n(\epsilon_\nu) \sim \epsilon_\nu^{-2}$, 4 TeV $< \epsilon_\nu <$ 2 PeV], and $\kappa \approx 8 \times 10^{49}$ erg for choked GRBs [$n(\epsilon_\nu) \sim \epsilon_\nu^{-2} e^{-\epsilon_\nu/3TeV}$, 300 GeV $< \epsilon_\nu <$ 4 TeV]. The conversion assumes that the detectable ν_μ flux represents 1/3 of the total ν flux (after oscillations). For IceCube-86, κ differs by an estimated ×0.5 (HL; [393]) to ×0.2 (choked; [394]).

The results provided here assume that each source has the same intrinsic neutrino brightness (limits based on a fixed average brightness are conservative compared to those using any other brightness distribution), and account for beaming of the HEN emission. For a source with intrinsic brightness $n_{\rm HEN}$ at distance r, the probability that ≥ 3 neutrinos will be detected from it is

$$p(n \geq 3 | r, n_{\rm HEN}) = 1 - F\left(2 | (10\ {\rm Mpc}/r)^2 n_{\rm HEN}\right), \tag{3.8}$$

where r is the source distance, F is the Poisson cumulative distribution function, and n is the number of detected neutrinos from the source. Therefore for galaxy i with blue luminosity $\mathrm{L}_{\mathrm{B}}^{(i)}$ at a distance r_i, the average number $\widehat{N}_i$ of sources which are discovered (i.e. have ≥ 3 detected neutrinos) will be

$$\widehat{N}_i(R,T) = p(n \geq 3 | r_i, n_{\mathrm{HEN}}) \cdot R/f_b \cdot T \cdot L_{\mathrm{B}}^{(i)}/L_{\mathrm{B}}^{\mathrm{MW}}, \tag{3.9}$$

where R is the source rate [number of sources per year per Milky Way equivalent (MWE) galaxy (w.r.t. blue luminosity)], f_b is the HEN beaming factor of the source, T is the duration of the measurement ($\approx$ 1 yr [7]), and $L_{\mathrm{B}}^{\mathrm{MW}}$ is the blue luminosity of the Milky Way. The 90% confidence source population upper limit R^{UL} will be the upper limit that satisfies $2.3 \geq \sum_i \widehat{N}_i(R^{\mathrm{UL}}, T)$, i.e.

$$R^{\mathrm{UL}}(n_{\mathrm{HEN}}) = \frac{2.3 f_b L_{\mathrm{B}}^{\mathrm{MW}}}{T \sum_{\delta_i \geq 0} p(n \geq 3 | r_i, n_{\mathrm{HEN}}) L_{\mathrm{B}}^{(i)}}, \tag{3.10}$$

where the sum is over all galaxies with declination $\delta_i \geq 0$. For $r > 40$ Mpc where we consider a homogeneous matter distribution, the summation is substituted with an integral. Figure 3-3 (top) shows the fraction of HEN sources as a function of n_{HEN}. In the lower plot, population upper limits for HEN sources are shown, taking into account the sources' HEN beaming factor f_b. As mildly relativistic jets from CCSNe and low-luminosity (LL) GRBs are expected to make up a significant portion of HEN sources of interest [9, 178, 211], we adopt $f_b = 14$ corresponding to LL-GRB beaming factor obtained in [227].

3.2.2 Upper limits from gravitational-wave observations

— We use the limits obtained by the latest GW all-sky burst search by Abadie et al. [6]. We consider their result for sine-Gaussian GW waveform in the sensitive band of the GW detectors (LIGO band, $\sim$ 150 Hz). Abadie et al. report no detection using the initial LIGO-GEO-Virgo detectors [154, 165, 229], and set a frequentist 90% confidence upper limit of $R_{Abadie} \approx 10^{-3}(10^{-2} M_{\odot} c^2 / E_{\mathrm{GW}}^{iso})^{3/2}$ yr^{-1}Mpc^{-3}, or 2.0 detectable events per year, on the population of the considered GW bursts. Here we interpret this result through introducing a GW horizon distance $D^{\mathrm{GW}}(E_{\mathrm{GW}}^{iso})$, within which any GW bursts with E_{GW}^{iso} energy would have been greater than the loudest background event of the measurement, such that $\frac{4}{3}\pi (D^{\mathrm{GW}})^3 R_{Abadie} \cdot (1 \text{ yr}) \simeq 2.0$. This gives $D^{\mathrm{GW}}(E_{\mathrm{GW}}^{iso}) = 7.8 \ (E_{\mathrm{GW}}^{iso}/10^{-2} M_{\odot} \ c^2)^{1/2}$ Mpc.

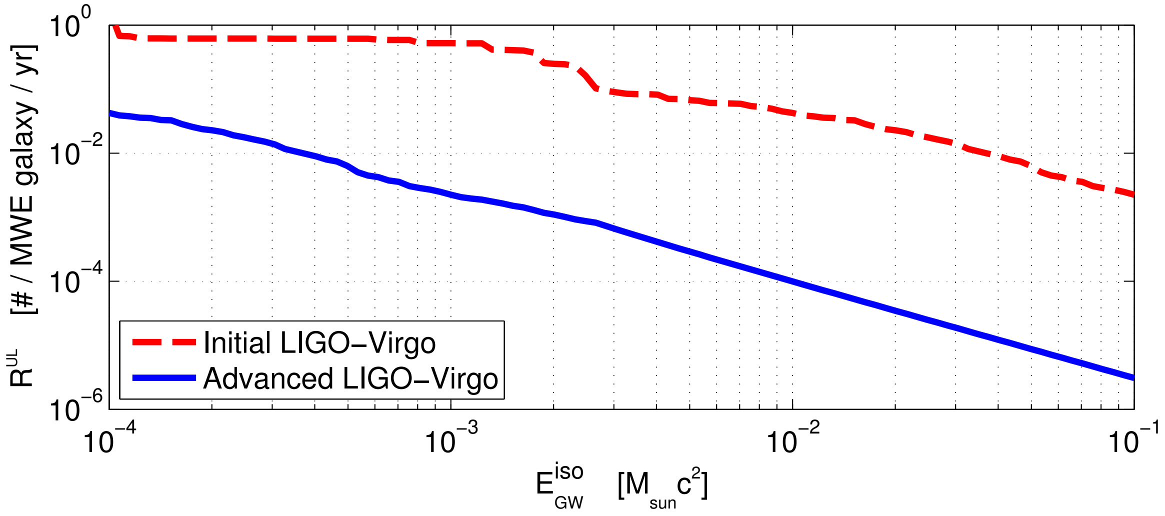

Figure 3-4: (Color online) Source population upper limits as functions of the sources' GW emission in isotropic-equivalent energy E_{GW}^{iso}. **Dashed red:** observational limits with initial LIGO-GEO-Virgo [6]. **Solid blue**: projected limits for the Advanced LIGO-GEO-Virgo GW detectors in the event of non-detection.

Using D^{GW} is a reasonable approximation of the detection efficiency of [6]. We conservatively assume isotropic GW emission since GW beaming is expected to be small (e.g. [134]). We thus derive a galaxy-based GW source population upper limit as a function of E_{GW}^{iso}, using the blue-luminosity-weighted distribution of galaxies as described in (i)-(ii) above:

$$R^{\mathrm{UL}}(E_{\mathrm{GW}}^{iso}) = \frac{2.0L_{\mathrm{B}}^{\mathrm{MW}}}{\sum_{r_i \leq D^{\mathrm{GW}}} L_{\mathrm{B}}^{(i)}} \cdot \mathrm{yr}^{-1}. \tag{3.11}$$

Here, we assumed that each GW source emits the same amount of GW energy. We estimate the achievable population upper limit for the Advanced LIGO-Virgo GW detector network by assuming a $\sim 10\times$ increase in sensitivity compared to initial detectors, with similar measurement duration. Results are shown in Figure 3-4.

3.2.3 Joint GW+HEN population upper limits

— Individual GW and HEN observations can be combined to determine a GW+HEN source population upper limit in the E_{GW}^{iso}–n_{HEN} parameter space. In Figure 3-5 (top) we provide GW+HEN population upper limits based on the statistical combination of current observa-

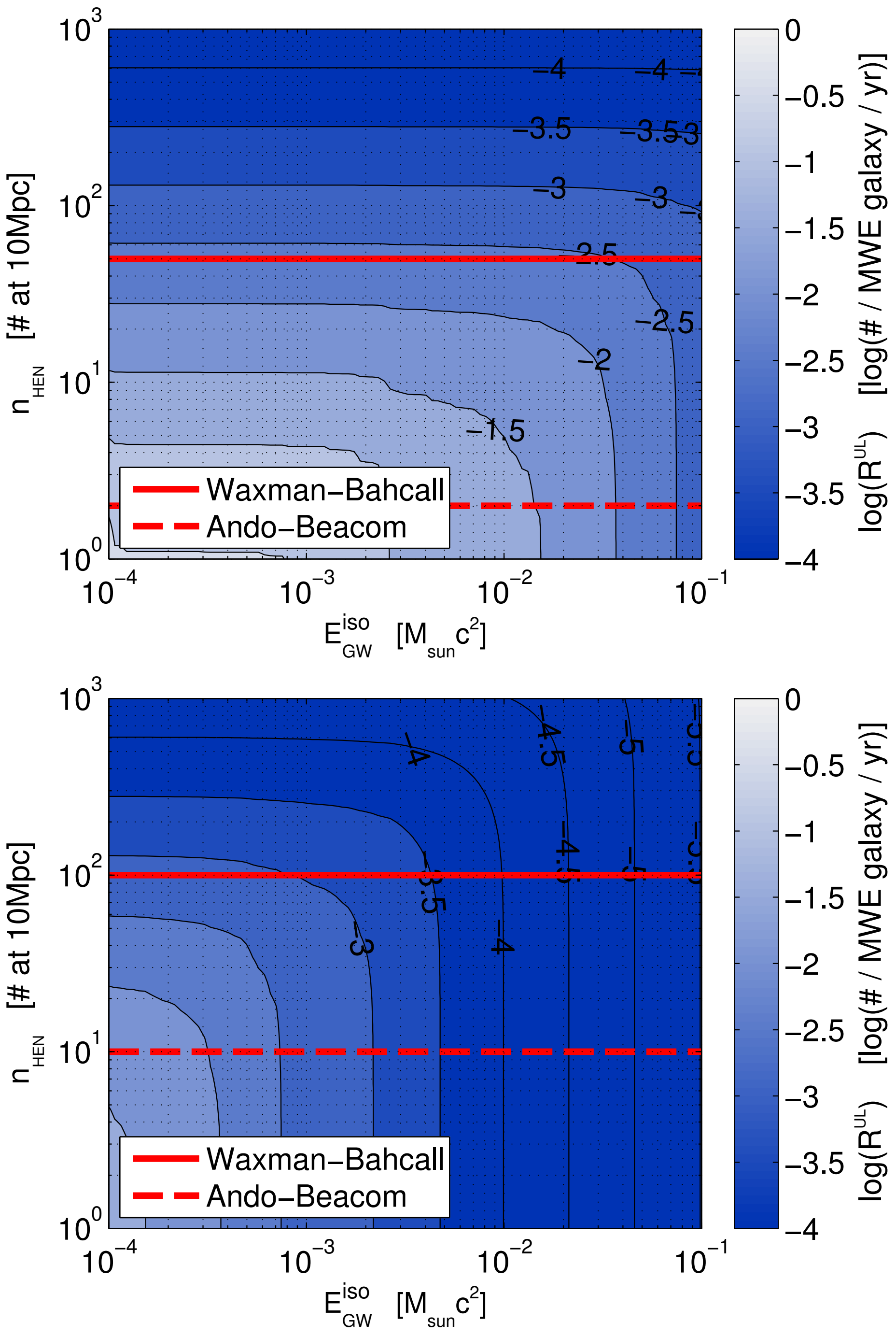

Figure 3-5: (Color online) GW+HEN source population upper limits based on the statistical combination of independent GW and HEN measurements. **Top:** observational results for measurements with the initial LIGO-GEO-Virgo GW detectors [6] and the IceCube-40 HEN detector [7]. **Bottom:** projected results for 1-year observations with Advanced LIGO-Virgo and IceCube-86. The limits shown assume a HEN beaming factor of 14. **Horizontal lines:** expected HEN rate from the Waxman-Bahcall [8] (solid) and Ando-Beacom [9] (dashed line) models, scaled to the IceCube-40 (top) and IceCube-86 (bottom) detector configurations.

tional results from independent GW and HEN measurements. We obtain a joint observational upper limit by considering that, on average, less than 2.3 GW+HEN bursts occur within D^{GW} or have ≥ 3 detected HENs per year (this is a $> 90\%$ confidence upper limit, since the GW and HEN measurements were longer than one year). The observational GW+HEN upper limit for a source population proportional to the blue-luminosity-weighted galaxy distribution will therefore be

$$R^{\mathrm{UL}}(E_{\mathrm{GW}}^{iso}, n_{\mathrm{HEN}}) = \frac{2.3 L_{\mathrm{B}}^{\mathrm{MW}} \cdot \mathrm{yr}^{-1}}{\frac{1}{f_b}\sum_{\{r_i > D^{\mathrm{GW}}, \delta_i \geq 0\}} p(n \geq 3 | r_i, n_{\mathrm{HEN}}) L_{\mathrm{B}}^{(i)} + \sum_{\{r_i \leq D^{\mathrm{GW}}\}} L_{\mathrm{B}}^{(i)}}. \tag{3.12}$$

Note that the first sum in the equation runs over sources farther than D^{GW}. This is to ensure that sources detectable by both GW and HEN detectors are not counted twice in the statistics. As the theoretical estimates [8, 9] shown in Fig. 3.12 are provided for km^3 scale detectors, for Fig. 3.12(top) we convert them to estimates for IceCube-40 using the factors 0.5 (hard) and 0.2 (soft) for the difference in sensitivity between IceCube-86 and IceCube-40.

Similarly to the above observational results, we also calculate the projected GW+HEN population upper limits based on the statistical combination of projected results from independent, 1 year long measurements with Advanced LIGO-GEO-Virgo and IceCube-86. Results are shown in Figure 3-5 (bottom).

We now estimate the projected population upper limits for GW+HEN sources obtainable with a joint GW+HEN search, considering a 1-year measurement with the Advanced LIGO-Virgo and IceCube-86 detectors. We consider an event candidate to be the coincidence of 1 GW trigger and 1 HEN. While we might detect more than 1 HEN from some sources, the fraction of such sources is small (see Figure 3-3), therefore we conservatively omit multi-HEN sources. For the joint search we define a horizon distance $D^{\mathrm{GWHEN}}(E_{\mathrm{GW}}^{iso})$, such that a joint GW+HEN event with 1 detected HEN and GW energy E_{GW}^{iso}, within D^{GWHEN} would be more significant than the (anticipated) loudest background event. We estimate D^{GWHEN} to be the same as the exclusion distance of the externally triggered search for GW bursts by Abbott et al. [345], who obtained a median exclusion distance of $D \sim 12$ Mpc $(E_{\mathrm{GW}}^{iso}/10^{-2} M_{\odot} c^2)^{1/2}$ with GW emission in the LIGO band. Such comparison to externally triggered GW searches

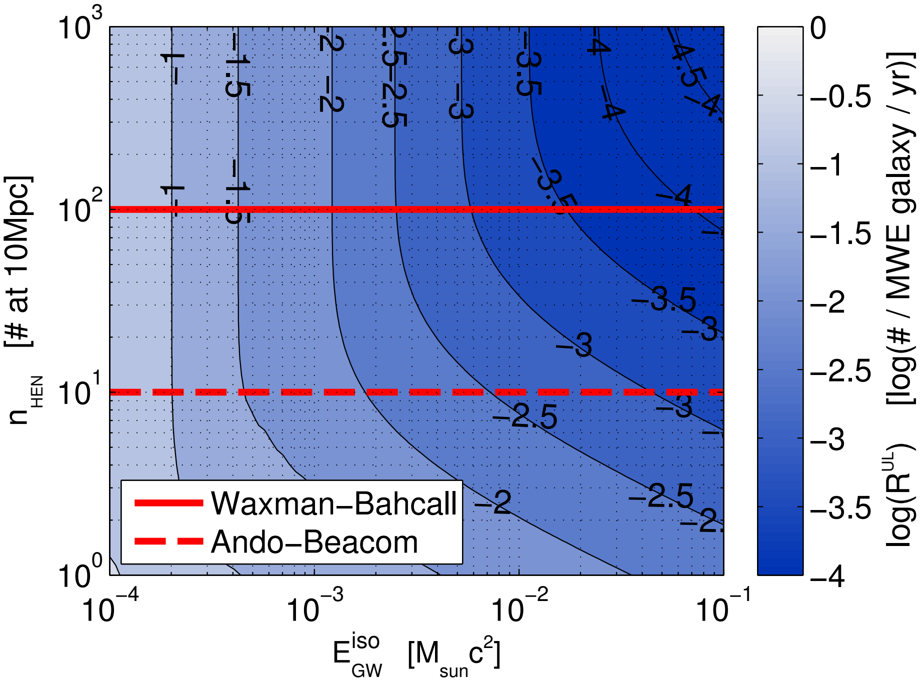

Figure 3-6: (Color online) Projected GW+HEN source population upper limits for a joint analysis of 1 year of observations with Advanced LIGO-Virgo and IceCube-86. Results are given as functions of source emission parameters E_{GW}^{iso} (GW emission in isotropic-equivalent energy) and n_{HEN} (average number of detected neutrinos from a source at 10 Mpc). **Horizontal lines:** expected HEN rate from the Waxman-Bahcall [8] (solid) and Ando-Beacom [9] (dashed line) models. The limits shown assume a HEN beaming factor of 14.

is a reasonable approximation if the joint search has $O(1)$ chance overlaps of background GW and HEN events (which can be controlled by adjusting the event selection threshold). For the joint GW+HEN search the estimated source population upper limit R^{UL} will be

$$R^{\mathrm{UL}}(E_{\mathrm{GW}}^{iso}, n_{\mathrm{HEN}}) = \frac{2.3 f_b L_{\mathrm{B}}^{\mathrm{MW}}}{T \sum_{\{r_i \leq D^{\mathrm{GWHEN}}, \delta_i \geq 0\}} p(n \geq 1 | r_i, n_{\mathrm{HEN}}) L_{\mathrm{B}}^{(i)}}. \tag{3.13}$$

The estimated population upper limits for a GW+HEN search are shown in Figure 3-6 for Advanced LIGO-Virgo and IceCube-86.

3.2.4 Discussion.

— To compare our results to emission models, we consider SNe Ib/c with mildly relativistic jets as promising GW+HEN emitters, whose rate $R_{\rm SN}^{jet}$ is $\lesssim 1\%$ [226] of the SN Ib/c rate $R_{\rm SN}$. This estimate is based on radio observations. It has been proposed, however, that mildly relativistic jets may be much more common, but completely choked (bright in neutrinos, dark in gamma-rays and radio) [178, 9]. The nearby CCSN rate is high enough to allow testing these models soon.

All-sky population upper limits with IceCube-86 are projected to exclude sources at rates $\geq R_{\rm SN}$ ($\lesssim 3\times10^{-2}$/yr/MWE galaxy) for $n_{\rm HEN}\gtrsim 12$ and at rates $\geq R_{\rm SN}^{jet}$ for $n_{\rm HEN}\gtrsim 300$ (Fig. 3-3). The former is comparable to the emission expected from SN jets by Ando & Beacom ($n_{\rm HEN}\approx 10$; [9]), or emission through reverse shocks in mildly relativistic jets ($n_{\rm HEN}\lesssim 7$; [178]). The latter is comparable to the Waxman-Bahcall flux, which estimates emission from HL-GRBs (which are, however, much rarer than SNe or LL-GRBs and have different spectra). Moreover, as evident from Fig. 3-4, advanced GW detectors are projected to exclude sources at rates $\geq R_{\rm SN}$ for $E_{\rm GW}^{iso}\gtrsim 2\times10^{-4}M_\odot c^2$, and at rates $\geq R_{\rm SN}^{jet}$ for $E_{\rm GW}^{iso}\gtrsim 5\times10^{-3}M_\odot c^2$. Both of these limits would exclude the suspended accretion model in the LIGO band [395], and significantly constrain, e.g., the collapsar accretion disk fragmentation model [97].

We obtain projected population constraints with a joint GW+HEN search (Fig. 3-6) that can be more restrictive in some regions of the parameter space than individual searches if the GW horizon distance $D^{\rm GW}$ of the joint search is $\gtrsim 2.4\times$ greater [$\sim f_b^{1/3}$] than $D^{\rm GW}$ of individual GW searches.

Chapter 4

Probing the Structure of Jet Driven Core-collapse Supernova and Long Gamma Ray Burst Progenitors with High Energy Neutrinos

This Chapter examines the question: What do the times of arrival of detected high energy neutrinos tell us about the properties of their source? We investigate the role of the opacity of CCSN/GRB progenitors in the properties and distribution of observed HENs, and how these observed HEN properties can be used to probe the progenitors' structure. Studying the optical depth at which HENs can escape the progenitor, we find a progenitor- and energy-dependent temporal structure of the high energy neutrino emission and jet breakout. Observations of HEN signatures of CCSNe or GRBs at neutrino telescopes, even with one or two events, could provide crucial information for differentiating between progenitors and characterizing their properties. Such information would advance our understanding of CCSNe, GRBs, and their relationship to each other.

Below, in Section 4.1, we review CCSN and GRB stellar models that we will use in our examination. In Section 4.2.1, we describe our calculations of the neutrino interaction length and optical depth inside the stellar envelope, and present our results on the energy-dependent radius from which neutrinos can escape. In Section 4.2.2, we discuss the temporal structure of energy-dependent neutrino emission from advancing and stalled jets for different stellar progenitors. This is followed in Section 4.2.3 by our results for energy dependent onset and emission duration of HENs. In Section 4.3, we present our interpretations for the energy-dependent onset of HEN emission and discuss how it probes the progenitors, particularly with a few detected neutrinos. We summarize our results in Section 4.4.

4.1 CCSN and GRB Progenitors

Current understanding of canonical long GRBs suggests that they are collapsars requiring a massive progenitor star that is (i) rapidly spinning [396, 397, 398, 399] and (ii) has a small radius ($\sim$ solar radius) [400, 401]. Successful GRBs also appear to prefer a lower metallicity [402], but choked GRBs may not require that. While this limited information does not always allow one to identify a specific progenitor, it does suggest that the progenitors are massive rotating stars [401].

Rotating red and blue supergiants (e.g., [403, 11]) may be the progenitors of many GRBs. These stars are in the final stages of the pre-collapse evolution of massive stars, whose collapse can naturally lead to CCSNe and GRBs. Furthermore, some of these stars may lose their hydrogen envelope due to a binary companion, which can help the stars retain the fast rotation necessary for the creation of GRBs [404].

Wolf-Rayet (WR) stars are originally heavy, but lose their hydrogen envelope (and therefore a significant fraction of their mass) through stellar winds. A relativistic jet from a rotating WR star can therefore escape without having to penetrate a hydrogen envelope, making these stars a common type of progenitor [11, 405]. Mass loss through stellar winds is expected to be significant for stars with higher metallicity [406]. One difficulty with such mass loss is that it carries away crucial angular momentum from the star. As the emergence of relativistic jets requires a very rapidly rotating core, losing angular momentum decreases the possibility of a GRB [407]. As a result, compact progenitors (i.e. that have lost their hydrogen and/or helium envelopes) also regularly explode as type Ibc supernovae without indications of a central engine injecting jet power into the explosion (e.g., [408]).

Model	Z $[Z_\odot]$	M $[\mathrm{M}_\odot]$	M_{He} $[\mathrm{M}_\odot]$	M_H $[\mathrm{M}_\odot]$	R $[10^{13}$ cm$]$	R_{He} $[10^{11}$ cm$]$	Ref.
15L	10^{-4}	14.9	4.5	7.4	0.4	1.4	[11]
15Lc	10^{-4}	5.2	1.7	0.4	N/A	1.4	[11]
15S	1	12.6	4.0	5.5	5.9	1.9	[11]
16T	10^{-2}	15.1	0.1	3×10^{-4}	8×10^{-2}	N/A	[407]
40S	1	8.7	0.1	10^{-3}	8×10^{-3}	0.8	[11]
75S	1	6.3	0.2	8×10^{-4}	7×10^{-3}	0.7	[11]
12L	10^{-4}	11.9	3.4	6.2	2.4	1.6	[11]
20L	10^{-4}	19.9	6.1	9.0	0.3	1.9	[11]
25L	10^{-4}	24.9	7.7	10.4	0.3	2.3	[11]
35L	10^{-4}	34.8	10.9	12.7	1.2	3.4	[11]
12S	1	10.7	3.4	5.1	4.3	1.9	[12]
15Sb	1	11.9	3.8	4.8	6.1	2.3	[12]
20S	1	12.7	4.0	3.5	7.7	2.8	[12]
25S	1	12.2	3.2	1.7	8.2	3.2	[12]
35S	1	14.6	2.2	0.4	0.1	0.2	[12]

Table 4.1: Properties of pre-supernova stellar models used in the analysis. The columns are: model name, metallicity, pre-supernova (PS) stellar mass, helium mass, hydrogen mass, stellar radius, helium core radius, and reference to models. Model names contain the ZAMS stellar mass, and a letter representing metallicity (L - low, T - 1% Solar, and S - Solar). There is additional differentiation between the various 15 $\mathrm{M}_\odot$ models we use.

Alternatively to stellar winds, massive stars can lose their hydrogen envelope to a companion star, which can leave more angular momentum at the core. Such rotating objects, composed of the bare helium core left behind, may also be GRB progenitors. Unusually rapid rotation on the main sequence can also result in mass loss [407].

Single stars with extremely rapid rotation may experience almost complete mixing on the main sequence [407], leading to a chemically homogeneous star. Such stars bypass the red giant phase and resemble WR stars, but with little mass loss. This scenario is particularly interesting for GRB production as it combines low mass loss with rapid core rotation, the two prerequisites for GRB emission.

Guided by these facts, we shall examine the following progenitor models in detail:

1. Red supergiant – zero-age main sequence (ZAMS) mass of 15 $\mathrm{M}_\odot$, both with solar (15S) and low (15L) metallicities. We further study the 15L model with its hydrogen envelope removed (15Lc) due to, e.g., a companion star.

2. Wolf-Rayet star – ZAMS mass of 75 $\mathrm{M}_\odot$ with solar metallicity (75S).
3. Bare helium core – ZAMS mass of 40 $\mathrm{M}_\odot$ with solar metallicity (40S).
4. Chemically homogeneous star – ZAMS mass of 16 $\mathrm{M}_\odot$ with low metallicity (16T).

We have indicated, in parentheses, the names of the models we consider in this study. To obtain the matter distribution and composition of these models, we use the numerical results of Woosley et al. [11], Woosley and Heger [407], and Heger et al. [12]. A detailed list of their properties (and a reference to the literature) is given in the upper box in Table 4.1. We also indicate in the table the references to the numerical results of the stellar progenitor models.

In addition to the models listed above, we examine other low- and solar-metallicity stars in the ZAMS mass range of (12 – 35) $\mathrm{M}_\odot$, also listed in the lower box in Table 4.1, to investigate some of our results' dependence on stellar mass and metallicity. Some of these models, which have ZAMS masses of $\lesssim 30\,\mathrm{M}_\odot$ will probably not create successful GRBs. Nevertheless, they can have choked relativistic jet activity that can be observed through neutrinos.

4.2 Calculations and Results

In this section, we characterize the effect of neutrino interactions on the observable HEN energies from jets. This effect can modify the neutrino flux from choked jets as well as from precursor neutrino emission for successful jets. We consider internal shocks for the calculation of the temporal structure and derive the energy-dependent onset time and duration for HEN emission. We note that there are alternative GRB emission models, which also predict different HEN emission (see Section 1.4.1). Below we consider internal shocks as the emission mechanism.

4.2.1 Optical Depth for High-Energy Neutrinos

Given the mass distribution $\rho(r)$ in a star, one can employ the expression for the neutrino mean free path described in the previous section to calculate the HEN optical depth of the star for a given distance from the center. We are interested in the innermost radius at which neutrinos can escape from the star.

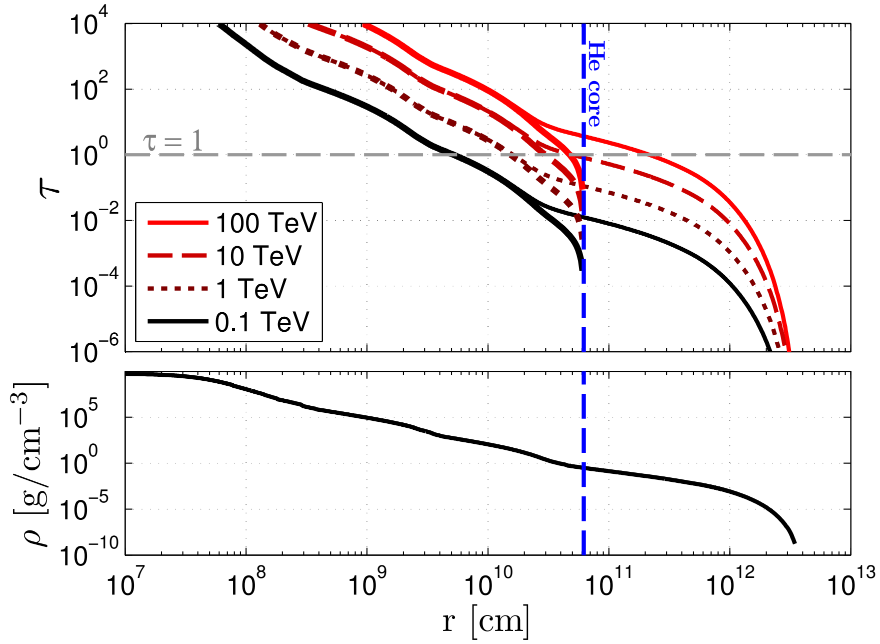

Figure 4-1: **(top)** High energy neutrino optical depths as a function of distance from the center of the star for different neutrino energies for a ZAMS $15\,\mathrm{M}_\odot$ star with low metallicity. A vertical dashed line shows the radius of the helium core. As a comparison, we show the optical depth of the helium-core-only case indicated with thick lines. The horizontal dashed line shows $\tau = 1$. Above this line, the stellar envelope is opaque to neutrinos. **(bottom)** The star's mass density as a function of distance from the center.

The optical depth τ of the star at a distance r_0 from its center, towards neutrinos that are produced at r_0 and are moving radially outward, is

$$\tau_\nu(\epsilon_\nu, r_0) = \int_R^{r_0} \frac{1}{\lambda_\nu(\epsilon_\nu, r)} \mathrm{d}r \tag{4.1}$$

where R is the stellar radius. We approximate neutrino absorption such that neutrinos with energy ϵ_ν cannot escape from below a critical radius r_ν for which $\tau_\nu(\epsilon_\nu, r_\nu) \approx 1$.

We calculated the optical depths for the considered massive stellar models (see Table 4.1) as functions of radial distance r from the center of the star, as well as neutrino energy ϵ_ν. In Figure 4-1, we exhibit the representative behavior of the neutrino optical depth as a function of distance from the center for a stellar model with $M = 15\,\mathrm{M}_\odot$ ZAMS mass and low metallicity. We can see that the hydrogen envelope of the ZAMS $M = 15\,\mathrm{M}_\odot$ star with low metallicity, for most relevant energies, is transparent to neutrinos. We also see that, for this stellar model, the helium core becomes opaque to neutrinos with all depicted energies around $\approx 10^{10}$cm.

To obtain r_ν as a function of neutrino energy, we inverted Equation 4.1 to derive the critical radii. In Figure 4-2, we present the critical radii for neutrinos. In the lower panel, we present the ratio of critical radius of antineutrinos and neutrinos (for the representative $M = 20\,\mathrm{M}_\odot$ low-metallicity case). One can see that the neutrino and antineutrinos have very similar critical radii. The maximum difference between the two radii is about 25%, indicating that our results on critical radii are valid for antineutrinos as well.

We have investigated the dependence of the above results on the mass and metallicity of the progenitor. To do so, we repeated the above exercise for models with low and solar metallicity, from (12-35) $\mathrm{M}_\odot$ listed in Table 4.1, and plotted the critical radius as a function of energy and ZAMS mass, separately for low and solar metallicity. A contour plot indicating the effect of ZAMS stellar mass on r_ν for different metallicities and neutrino energies is shown in Figure 4-3. The critical radius that corresponds to the supernova-progenitor's helium core is indicated with dashed horizontal lines (if all neutrinos with $\epsilon_\nu < 10^6$ GeV can escape the core, the horizontal dashed line lies above the shown parameter space; this is indicated with arrows pointing upwards).

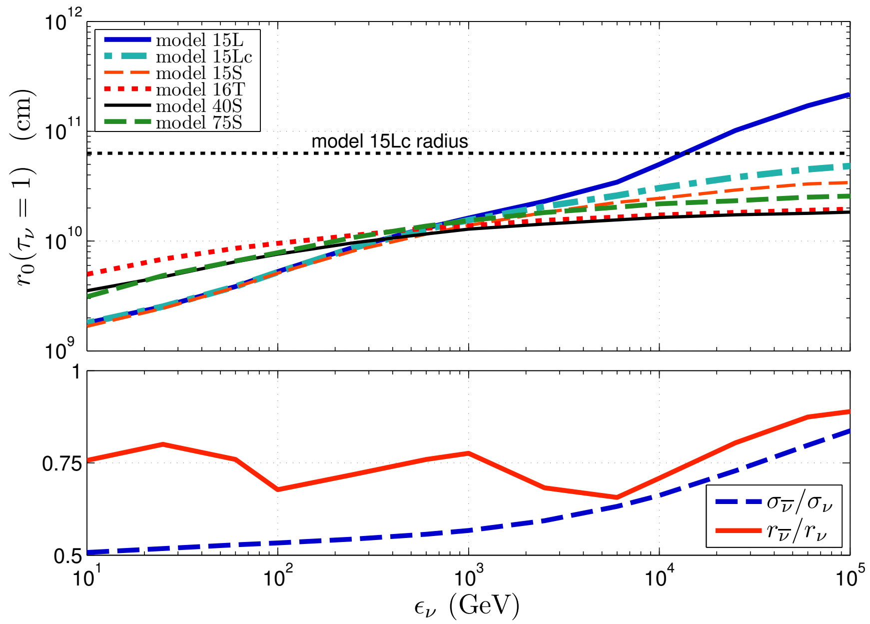

Figure 4-2: **(top)** Critical radius r_ν as a function of neutrino energy for the considered progenitor models (see Table 4.1). The horizontal dashed line shows the pre-supernova helium-core radius for the ZAMS 15 $\mathrm{M}_\odot$ star with low metallicity (model 15Lc). **(bottom)** Ratio of cross sections for neutrinos and antineutrinos $\sigma_{\overline{\nu}}/\sigma_\nu$ (data taken from [10]), and the obtained ratio of the critical radii for neutrinos and antineutrinos, as the function of neutrino energy, for the ZAMS 20 $\mathrm{M}_\odot$ star with low metallicity.

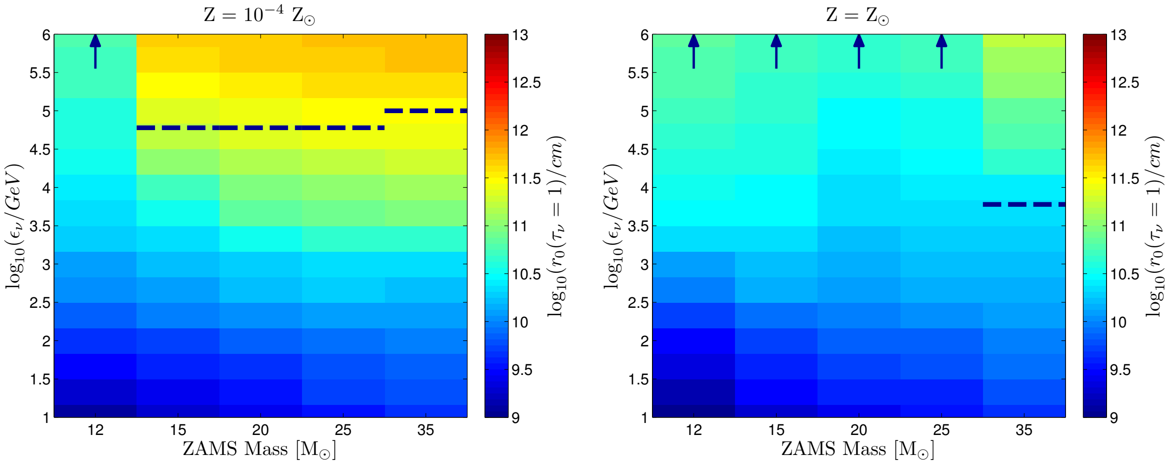

Figure 4-3: Critical radius $r_\nu = r_0(\tau_\nu = 1)$ as the function of ZAMS stellar mass and neutrino energy ϵ_ν for low-metallicity **(left)** and Solar-metallicity **(right)** simulations by Woosley et al. [11], and Heger et al. [12]. The horizontal dashed lines show, for each ZAMS mass, the energy for which the critical radius is equal to the pre-supernova helium core radius (if all neutrinos with $\epsilon_\nu < 10^6$ GeV can escape the core, the horizontal dashed line lies above the shown parameter space; this is indicated with arrows pointing upwards). Consequently, neutrinos with energies above the dashed lines cannot escape if produced inside the helium core. Note that, as shown for an example in Figure 4-1, the presence of the hydrogen envelope has only small effect on this threshold energy.

Figure 4-3 shows that the critical radius lies within the stellar helium core for neutrino energies of $\epsilon_\nu \lesssim 10^5$ GeV for practically all massive progenitors. Consequently, the most relevant neutrino energy range for observations will become observable somewhere beneath the stellar core, making neutrino observations from choked-GRBs relevant. The results further indicate that $r_\nu(\epsilon_\nu)$ is determined predominantly by the pre-supernova mass (and not the ZAMS mass) of the progenitors.

4.2.2 Temporal Structure of Jets

Jets have been studied numerically and analytically, and a detailed understanding has been developed; see, e.g., references in [178]. For our work, we use the semi-analytic method of Horiuchi and Ando [178] to calculate the velocity of the jet head advancing inside the star in order to characterize the temporal structure of HEN emission. This simple treatment assumes a constant jet opening angle, and will suffice to illustrate our point, but in the future this may be improved through more detailed numerical modeling of the jet morphology for individual progenitors.

Horiuchi and Ando consider the propagation of a relativistic jet with Lorentz factor $\Gamma_j \gg 1$. As the head of the jet advances through stellar matter with Lorentz factor Γ_h, a reverse and forward shock occur. The reverse shock decelerates the head, while a forward shock accelerates the stellar material to Γ_h. In the following, we use the subscripts j (jet, unshocked), h (jet head, shocked), s (stellar, shocked), and ext (stellar, unshocked) to denote quantities at different regions in and around the jet. Using this notation, the evolutions of the two shocks at the jet head are governed by the following equations [409, 410]:

$$e_s/n_s m_p c^2 = \Gamma_h - 1, \qquad n_s/n_{ext} = 4\Gamma_h + 3, \tag{4.2}$$

$$e_h/n_h m_p c^2 = \overline{\Gamma}_h - 1, \qquad n_h/n_j = 4\overline{\Gamma}_h + 3, \tag{4.3}$$

where m_p is the proton mass, c is the speed of light, and n_i and e_i are the particle density and internal energy measured in the fluids' rest frames. Lorentz factors are measured in the lab frame, except $\overline{\Gamma}_h = \Gamma_j \Gamma_h (1 - \beta_j \beta_h)$ that is measured in the jet's comoving frame ($\beta_i c$ is

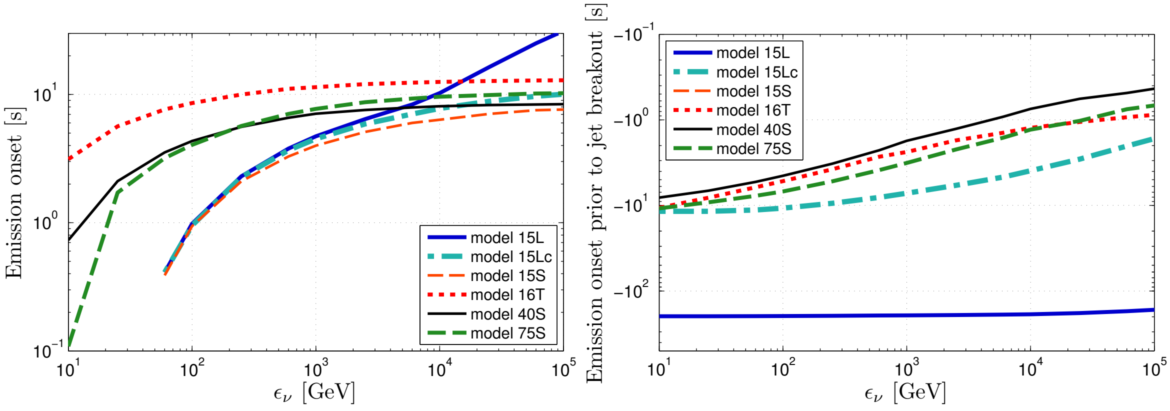

Figure 4-4: **(left)** Onset of observable HEN emission measured from the time when HEN production commences ($(t_e(\epsilon_\nu) - t_0)$), as a function of neutrino energy, for different stellar progenitors. **(right)** Time of jet breakout measured from the time of the onset of observable HEN emission ($(t_{br} - t_e(\epsilon_\nu))$), as a function of neutrino energy, for different stellar progenitors (note the inverse scale on the y axis). The calculations are carried out for the stellar models in Table 4.1 with jet energy $L_{iso} = 10^{52}\,\mathrm{erg\,s^{-1}}$ and jet Lorentz factor $\Gamma_j = 10$.

the velocity). For a jet with constant opening angle, the jet particle density at radius r is

$$n_j(r) = \frac{L_{iso}}{4\pi r^2 \Gamma_j^2 m_p c^3} \tag{4.4}$$

where L_{iso} is the isotropic-equivalent jet luminosity. At the jet head, the shocked jet head and shocked stellar matter are separated by a contact discontinuity, and are in pressure balance. Equating their pressures ($p_h = e_h/3$ and $p_s = e_s/3$, respectively) and using Equations (4.3) and (4.4), we arrive at

$$\frac{n_j}{n_{ext}} = \frac{(4\Gamma_h + 3)(\Gamma_h - 1)}{(4\overline{\Gamma}_h + 3)(\overline{\Gamma}_h - 1)} \tag{4.5}$$

We numerically solve Equation (4.5) using the appropriate stellar particle number density $n_{ext} = n_{ext}(r)$ of the considered stellar models (see Table 4.1) to obtain the jet propagation velocity as a function of radius. We took the terminal Lorentz factor of the jet head to be Γ_j in the limit of zero density. Similarly to Ref. [178], we find that the velocity of the jet head is practically independent of the gamma factor Γ_j of the jet, and increases with the isotropic equivalent energy L_{iso} of the jet (in the relativistic limit, the gamma factor of the jet head $\Gamma \propto \Gamma_j^{1/4}$ [177]).

4.2.3 Energy-dependent Emission Onset Time

The skewed neutrino emission due to stellar neutrino-opacity can be characterized through the temporal structure of observable emission. Let t_0 be the time when the relativistic jet reaches the shock radius $r_s \approx \Gamma_j^2 c\delta t \approx 3 \times 10^9\,\mathrm{cm}$. At this radius, internal shocks can form, causing HEN production to commence [180]. Neutrinos that are produced while the jet is still beneath the stellar surface may only be able to escape from the star through the envelope at a later, energy-dependent "escape" time $t_e(\epsilon_\nu)$, where ϵ_ν is the energy of the neutrino. At $t_e(\epsilon_\nu)$ the jet has advanced far enough so the remaining envelope and the jet itself is no longer opaque to neutrinos with energy ϵ_ν. More specifically, we take $t_e(\epsilon_\nu)$ to be the time when the jet reached the critical radius r_ν for which $\tau_\nu(\epsilon_\nu, r_\nu) = 1$.

In Figure 4-4 (left), we show $t_e(\epsilon_\nu) - t_0$ (observer frame) as a function of ϵ_ν for different stellar progenitors, which we calculated assuming a mildly relativistic ($\Gamma_j = 10$) jet with $L_{iso} = 10^{52}\,\mathrm{erg\,s^{-1}}$ output. We can see that as neutrinos with lower energies can easily escape through the stellar envelope, one finds $t_e(\epsilon_\nu \ll 100\,\mathrm{GeV}) - t_0 \approx 0$.

It is also interesting to compare the escape time $t_e(\epsilon_\nu)$ with the jet breakout time t_{br} from the stellar envelope. The point of jet breakout was chosen to coincide with the jet reaching the radius at which the simulated stellar progenitor models end. This corresponds to a sharp drop in matter density, dropping below $10^{-10}\,\mathrm{g\,cm^{-3}}$ for models 15L and 16T, and dropping below $10^{-4}\,\mathrm{g\,cm^{-3}}$ for models 40S and 75S, while the simulation ends at $10^{13}\,\mathrm{cm}$ for model 15S. Due to the low densities at the boundary of the simulated progenitors, the results should be robust to the specific choice of jet breakout radius. We note that the bulk of the gamma-ray emission from the jet may be shortly delayed compared to the breakout due to dissipation within the jet until the jet advances to a distance of $\gtrsim 10^{13}\,\mathrm{cm}$ [411, 62, 389, 412]. The GRB will become detectable within a few seconds after the jet head leaves the helium core [413].

Figure 4-4 (right) shows the time it takes for the jet to break out of the star from the point from which neutrinos can first escape (i.e. $t_{br} - t_e(\epsilon_\nu)$), as a function of ϵ_ν for different stellar progenitors. As before, a mildly relativistic ($\Gamma_j = 10$) jet with $L_{iso} = 10^{52}\,\mathrm{erg\,s^{-1}}$ output has been used. A disadvantage of using t_{br} for comparison is that it is only available for successful jets, and therefore it cannot be used to characterize, e.g., choked GRBs.

As the figure shows, when the jet is close to the center of the progenitor, only low energies neutrinos can escape the star. Gradually, as the jet proceeds outward, higher energy neutrinos become observable. Consequently, neutrinos escaping (and observed) earlier are expected to have lower energies, leading to a time dependent neutrino energy distribution, with the average energy increasing with time. Such distribution may be indicated upon the detection of multiple neutrinos from a CCSN. The precise relationship of the energy-dependent onset times and emission durations of HENs can encode information about the progenitors' density profile and composition.

4.2.4 Dependence on source parameters

The results presented above were calculated for sources with mildly relativistic jets ($\Gamma_j = 10$) with L_{iso} luminosity, and with jet variability of δt. From these parameters, Γ_j and δt determine the shock radius r_s (see Sec. 4.2.3). For greater Γ_j and δt, neutrino production will commence only at a greater radius, changing the lowest radius and earliest time from which neutrinos are observable. The jet luminosity L_{iso} affects the jet head velocity, with greater (smaller) L_{iso} corresponding to greater (smaller) velocity, which in turn change the time scale on Figure 4-4; the jet head velocity is practically independent of Γ_j and δt (see also [178]). These dependencies, however, do not affect our conclusions qualitatively.

4.3 Interpretation of Energy and Time Structure of Neutrino Emission

4.3.1 Strong-signal limit

For a very nearby CCSN or GRB, one expects a modestly large HEN flux of perhaps $\gtrsim 100$ events. Although this possibility is rare, it does represent a rather lucrative opportunity. The highest energy neutrino detected from such a source at any time constrains the total matter content of the envelope above the jet head at that time. Therefore, one can take the opportunity to map the inner stellar density profile and the jet's velocity.

Comparison of the emission onset profiles of different stellar progenitor models in Figure 4-4 (left panel) shows that, with a high-enough HEN flux, the stellar models have distinguishable energy-time profiles (i.e. cutoff energies as a function of time). For example, for a 5s long precursor emission, the groups of models {16T}, {40S,75S} and {15L, 15Lc,15S} are distinguishable, while members of a given group have practically the same energy cutoff.

Another consequence of the radius-dependent neutrino energy cut-off is that neutrinos emitted by choked relativistic jets (e.g., choked GRBs) will have an energy cutoff, resulting in lower average energy than jets that successfully break through to the surface of the star (e.g., successful GRBs). Such a difference can possibly be indicated upon the detection of a sufficient number of neutrinos from a set of CCSN with and without electromagnetic counterparts. The indication of a difference in average energies from successful and choked jets can provide information, e.g., on the distance the choked jets advance before they stall, a possible indicator of the energy and/or baryon content of the jets.

4.3.2 Weak-signal limit

Most observed astrophysical sources will only lead to $\mathcal{O}(1)$ detected neutrinos. Therefore, we find it more practical to consider the possibility that only a few neutrinos are detected. In the following, we explore some ideas for recovering structural information of the progenitors using only a few observed HENs. Such recovery may not be conclusive for every detected source, but for specific detections where the energy and timing of detected neutrinos are favorable, it can provide important information about the source.

HEN timing prior to time of jet breakout

The time difference between the onset of the (energy-dependent) observable HEN emission and the jet breakout can be used to constrain the possible progenitors, potentially even with one detected HEN. If the observation time of a detected neutrino and the time of the jet breakout differs more than what is allowed for a progenitor model, the respective progenitor model can be ruled out or weakened. For example, if one detects a HEN with reconstructed energy $\epsilon_\nu \approx 10^3$ GeV approximately $\sim$5 sec before the jet breakout, Figure 4-4 (right) suggests that one can practically rule out models {15S,16T,40S,75S}, while models {15L,15Lc} are possible progenitors. We note that it may be difficult to directly observe the time of jet breakout as the gamma-ray photosphere typically lies above the stellar surface.

HEN relative timing

It is also possible to constrain progenitors even if the jet does not break out of the star. In this case, the time difference between at least two observed neutrinos can be used to constrain possible progenitors by determining whether the observed time difference is possible or likely for a given progenitor model and the reconstructed neutrino energies. For example, the observation of two neutrinos, both with energies $\epsilon_\nu \approx 10^3$ GeV with ∼10 sec time difference would rule out all models but 15L out of those considered in Figure 4-4, indicating the presence of a hydrogen envelope.

Jet duration vs. onset of neutrino emission

Neutrinos above $\epsilon_\nu \gtrsim 10^3$ GeV for all models but 15L are emitted only in a small fraction of the time the jet spends within the progenitor. Since it is unlikely that jets are fine-tuned such that they stop just before breaking out of the star, the detection of HENs with $\epsilon_\nu \gtrsim 10^3$ GeV from confirmed astrophysical sources with no EM counterparts would make it highly probable that the progenitors have kept their hydrogen envelope prior to explosion.

Neutrinos and gravitational waves

The coincident observation of gravitational-waves and HENs from a common source has far-reaching astrophysical implications [13, 238]. The relation between the observed times of arrival of gravitational waves and HENs from a stellar core collapse could provide information on the stellar structure below the shock region of $\gtrsim 10^{10}$ cm (complementary to information from HENs and EM radiation, which map the structure at and above the shock region).

The time relativistic jets take to cross the stellar envelope is likely comparable to or less than the observed duration of prompt gamma-ray emission (as the duration of the outflow fed by the central engine is unlikely to be fine-tuned to the envelope crossing time). Given the observed long-GRB durations of $\approx (10-100)$ s and expected stellar progenitor densities at small radii, the jet is only likely to be able to cross the envelope within $\approx (10-100)$ s if the stellar density significantly decreases along the rotational axis [413]. Gravitational-wave emission from the stellar progenitor is likely connected to the onset of jet propagation (core-collapse and the formation of an accretion disk are both potential sources of gravitational waves [272]). Consequently, comparing the time of arrival of gravitational wave signals and HENs from a GRB or supernova progenitor can provide information on stellar densities below the shock region, and may provide information on the development of jets (see [413]).

Extremely high energy neutrino triggers

Extremely high energy neutrinos of energies $\epsilon_\nu \gtrsim 100\,\mathrm{TeV}$ may be emitted once the relativistic jet becomes sparse enough such that neutrino production is not suppressed by strong magnetic fields or high synchrotron-photon density [185, 178]. The emission of such extremely high energy neutrinos may commence only once the jet has advanced substantially, likely outside the helium envelope [178]. These neutrinos will therefore be produced only after most lower energy HENs are created while the jet is at lower radii (we note that the central engine of GRBs may show activity on a longer time scale than the prompt gamma-ray emission [414], therefore weaker, longer duration neutrino emission is also plausible). Processes other than internal shocks, such as the jet's interaction with the interstellar medium, can further produce so-called ultra high energy neutrinos with energies up to $10^{10}\,\mathrm{GeV}$ that may be of interest here [202, 415, 382]. Hence, it may be interesting to search for $\gtrsim 100\,\mathrm{TeV}$ neutrinos in coincidence with $\lesssim 100\,\mathrm{TeV}$ neutrinos that arrived prior to an extremely high energy neutrino up to tens of seconds.

While HEN detectors mainly use Earth as a shield from atmospheric muons, extremely high energy neutrinos with $\epsilon_\nu \gtrsim 1\,\mathrm{PeV}$ are also absorbed before they can cross Earth, and thus can only be detected from downgoing and horizontal directions [14]. Even though there is an abundant atmospheric muon background from these directions in the detector, most these muons have lower energies; hence, astrophysical extremely high energy neutrinos are relatively easy to identify.

Based on the above model, a search could be performed for extremely high energy neutrinos in coincidence with $\lesssim 100\,\mathrm{TeV}$ neutrinos that arrived from the same direction, prior to the extremely high energy neutrino up to tens of seconds. This search could be particularly interesting, as $\lesssim 100\,\mathrm{TeV}$ neutrino data have not been utilized in searches for astrophysical neutrinos (nevertheless, these downgoing events are recorded and stored for IceCube [416]).

4.4 Conclusions

In this Chapter we investigated the opacity of massive pre-supernova stars to high energy neutrinos (HENs) in order to address the question: What do the times of arrival of detected high energy neutrinos tell us about the properties of their source? We investigated the effect of opacity on the observable HEN emission from both successful and choked jets. In particular, we have examined various zero-mass main sequence (ZAMS) stellar masses from (12-75) $\mathrm{M}_{\odot}$ for low-metallicity non-rotating and stellar-metallicity rotating cases.

For the considered progenitors, we presented the energy-dependent critical radius from which HENs cannot escape. We found that the presence of the stellar hydrogen envelope has a negligible effect on the optical depth for neutrino energies of $\epsilon_{\nu} \lesssim 10^{5}$ GeV, i.e. the most relevant energy range for HEN detection. The critical radius, however, largely varies with ϵ_{ν} within the helium core, which has relevant consequences on observations.

The neutrino emission spectrum changes as the relativistic jet advances in the star. Considering mildly relativistic jets ($\Gamma_{j} \approx 10$) and HEN production in internal shocks, the energy dependence of the onset of neutrino emission is shown in Figure 4-4. Such time dependence can provide important information on the stellar structure. For instance, with observation of multiple HENs, the detected neutrino energies and times provide constraints on stellar density at different depths in the star. The energy of a detected precursor HEN can also provide information on the maximum time frame in which the relativistic jet will break out of the star and become observable.

We examined how neutrino interaction with dense stellar matter can be used to probe stellar progenitors. We investigated both the strong and weak-signal limits, i.e. when many or only a few neutrinos are detected, respectively. We demonstrated that under favorable conditions one can use the time difference between a precursor neutrino and the jet breakout to exclude some progenitor models. The relative times of arrival for multiple neutrinos may also be sufficient to exclude progenitor models, even with no observed electromagnetic emission. Additionally, the detection of HENs with energies above $\gtrsim 10^{3}$ GeV from choked GRBs makes it likely that the progenitor possessed a hydrogen envelope prior to explosion. Also, while the detection of HENs and electromagnetic signals can provide information on the stellar region at and above the shock radius, the coincident detection of HENs with gravitational waves [13] may be informative w.r.t. jet development and propagation below the shock radius. We proposed the use of extremely-high energy neutrinos ($\epsilon_\nu \gtrsim 100\,\mathrm{TeV}$) detected by cubic-kilometer neutrino detectors such as IceCube for searches for coincident downgoing neutrinos. These extremely-high energy events probably arrive after other lower energy events that can be used in a coincident analysis. Downgoing neutrinos with lower energies are typically not used in searches due to the large atmospheric muon background from these directions and energies.

A future extension of this work will be the calculation of neutrino fluxes from different radii, similar to the calculations of Razzaque et al. [185], who estimated the flux for two different radii, but without timing information. Such addition to the temporal structure of neutrino energies can provide a more detailed picture of not only the information in neutrinos about the progenitor, but also the likelihood of detecting neutrinos with given information content.

We note here that the uncertainty in the reconstructed energy and timing of HENs introduces uncertainty in the measurement of the onset of HEN emissions at the energies of the detected neutrinos. These uncertainties need to be taken into account when comparing emission models to observations. Additionally, there could be other factors, e.g., physics related to jet propagation, that we have treated schematically in this work, but could have similar impact on the temporal structure of HEN events. However, we have pointed out some generic features which should motivate future work that investigates experimental detectability of these features.

Chapter 5

Search for Common Sources of Gravitational Waves and High Energy Neutrinos

In this chapter, following [272], we present a joint GW and HEN analysis algorithm that combines the observations of a network of GW detectors and a HEN detector. We then describe preliminary, closed box results from this search performed using GW data from initial LIGO/Virgo (S5/VSR1 science runs), and the partially completed IceCube detector (22 strings; hereafter IceCube-22). To scale theoretical expectations on the HEN rate for km^3 detectors to expectations for IceCube-22, we estimate IceCube-22 to be approximately 10 times less sensitive than the completed IceCube.

Besides looking for astrophysical GW+HEN messengers, the search can also be used to derive upper limits on the population and flux of GW+HEN sources. We estimate the anticipated science reach for initial and advanced detectors, and discuss some of the existing emission models and how they can be constrained in the event of non-detection.

In Section 5.1 we describe the output of the GW and HEN detectors, as well as the astrophysical source distribution. We derive the quantities that will be used in joint GW+HEN analyses. In Section 5.2 we go on and describe the joint analysis method for the search for GW+HEN signals. Next, in Section 5.3 we investigate the constraints one can introduce with the GW+HEN search on the population of astrophysical GW+HEN sources. Finally, in Section 5.4, we present preliminary results of the analysis.

5.1 Data

5.1.1 Gravitational-wave Data

GW search algorithms are designed to detect and extract information about a GW signal from a stream of strain data from a set of GW detectors (e.g. [417, 418, 419]). One can think of a generic search algorithm as a GW radiometer, outputting the excess GW energy measured by a network of detectors, as a function of time t and sky location $\overrightarrow{x_s}$. These data analysis algorithms usually output so-called GW triggers, potential GW signals whose significance exceed a given threshold. A GW trigger's significance is characterized by a suitable test statistic (see e.g. [417, 418, 417]). GW triggers can have additional parameters, such as time of arrival, amplitude or waveform. Data from a network of GW detectors can also be used to recover directional information (e.g., [332]).

For the purposes of the joint GW+HEN analysis, we consider short transient events. The duration of a transient GW event is expected to be much shorter than the coincidence time window [238] of GW and HEN events (the window in which all GW and HEN signals arrive).

To obtain the background distribution of GW triggers, we time-shift data from the different GW detectors compared to each other such that no astrophysical signal can appear in more than one detector at a time. Background triggers can be generated in such a way for many different time shifts.

Let us assume that we have a GW search algorithm that identifies a set of GW triggers, for each trigger calculating a test statistic TS and a skymap (point spread function) $\mathcal{F}_{\mathrm{GW}}(\overrightarrow{x_s})$. The point spread function gives the probability distribution of source direction, given that the GW event is of astrophysical origin. To calculate the significance of a joint event, we need to take into account TS as well as $\mathcal{F}_{\mathrm{GW}}(\overrightarrow{x_s})$. The background distribution of TS can be obtained from time-shifted data. The distribution of TS for the case of a signal present, however, is not available, as it would greatly depend on the properties and direction of the signal. Therefore, we take into account TS in the joint significance by calculating its p-value, given the background distribution.

Let FAR_i be the false alarm rate of GW event i, corresponding to the rate of GW events with $\text{TS} \geq \text{TS}_i$ (average number of events over unit time). For TS_i we assign a p-value of

$$p_{\text{GW}}^{(i)} = 1 - \text{Pois}(0; T \cdot \text{FAR}_i),$$

where $\text{Pois}(k, \lambda)$ is the Poisson probability of k outcome with λ average, and T is the coincidence time window (see section 5.2.1). FAR_i is calculated from the distribution of background events.

For the skymap $\mathcal{F}_{\text{GW}}(\overrightarrow{x_s})$ both the background and signal distributions are available. We therefore take this information into account in the form of a likelihood ratio. Here our null hypothesis is that the GW event is a random fluctuation from the background, i.e. it has no preferred direction. We therefore approximate the background likelihood $\mathcal{B}_{\text{GW}}^{(i)}$ to be a flat distribution over the whole sky, i.e.

$$\mathcal{B}_{\text{GW}}^{(i)} = \frac{1}{4\pi}. \tag{5.1}$$

Our alternative hypothesis is that GW event i came from an astrophysical source at direction $\overrightarrow{x_s}$. The signal likelihood $\mathcal{S}_{\text{GW}}^{(i)}$ will be the calculated skymap, i.e.

$$\mathcal{S}_{\text{GW}}^{(i)}(\overrightarrow{x_s}) = \mathcal{F}_{\text{GW}}(\overrightarrow{x_s}). \tag{5.2}$$

5.1.2 High-energy Neutrino Data

The direction of HENs can be reconstructed using the arrival time of Cherenkov photons at different optical sensors, with a precision of $\sim 0.5° - 1°$ (depending on energy) for IceCube [394], or less than 0.3° for ANTARES [193]. Direction reconstruction is also one of the major tools in background rejection. So-called atmospheric muons, created by cosmic rays interacting with particles in the atmosphere over the detector, are the dominant background. To suppress these events, searches for neutrinos are principally performed using up-going events, i.e. those that have traveled through Earth and therefore can be attributed only to a neutrino. The vast majority of these up-going neutrinos are themselves the result of cosmic ray interactions on the other side of the Earth. These are the so-called atmospheric neutrinos, and in general constitute an irreducible background in searches for astrophysical neutrinos from space.

Many sources of astrophysical neutrinos are expected to exhibit a harder energy spectrum (typically E^{-2}) compared with the soft spectrum of atmospheric neutrinos ($\sim E^{-3.7}$). In such cases, reconstructed energy can play a role in further separating signal from background. The measured energy of the muon (related to the amount of light detected) becomes an estimated lower bound for the neutrino primary energy, since the muon may have propagated an unknown distance before reaching the detector. Probability distribution functions for the muon energies expected from signal (of different source spectra) and background can then be used in likelihood analyses to enhance sensitivity for hard source spectra while retaining sensitivity to softer spectra [191, 420].

A given reconstructed neutrino event i consists of a time of arrival $t_\nu^{(i)}$, reconstructed direction $\overrightarrow{x_i}$, directional uncertainty σ_i and reconstructed neutrino energy E_i. The neutrino point spread function, i.e. the probability distribution of the neutrino source direction, is defined as

$$\mathcal{F}_\nu(\overrightarrow{x_s}|\overrightarrow{x_i}) = \frac{1}{2\pi\sigma^2} \cdot e^{-\frac{|\overrightarrow{x_i}-\overrightarrow{x_s}|^2}{2\sigma_i^2}}, \tag{5.3}$$

where $\overrightarrow{x_s}$ is the true sky location of the source. The HEN point spread function is incorporated in the joint GW+HEN significance in the form of a likelihood ratio. Our null hypothesis is that HEN event i is a detected atmospheric neutrino, having no preferred direction. We approximate the background likelihood $\mathcal{B}_\nu^{(i)}$ to be a flat distribution over one hemisphere (since a neutrino detector is only sensitive to roughly half the sky), i.e.

$$\mathcal{B}_\nu^{(i)} = \frac{1}{2\pi}. \tag{5.4}$$

Our alternative hypothesis is that the neutrino came from an astrophysical source at direction $\overrightarrow{x_s}$. The signal likelihood $\mathcal{S}_\nu^{(i)}$ will be the point spread function, i.e.

$$\mathcal{S}_\nu^{(i)}(\overrightarrow{x_s}) = \mathcal{F}_\nu(\overrightarrow{x_s}). \tag{5.5}$$

For reconstructed neutrino energy E_i, the background distribution is known from the detected (background) neutrinos. The distribution of E_i for astrophysical signals, however, depends on the source emission model, therefore we treat it as unknown. We therefore take into account E_i in comparison with its background distribution by calculating its p-value $p^{(i)}_{\mathrm{HEN}}$, defined as the fraction of background neutrinos having energy $E \geq E_i$.

5.1.3 Neutrino Clustering

After obtaining the properties of individual neutrino events, we consider the possibility that multiple neutrinos are detected from the same astrophysical source. A set of neutrinos can potentially originate from the same source only if they are spatially and temporally coincident.

As it is described in section 5.2.1 below, assuming that a GW+HEN source emits neutrinos within a time interval Δt_ν (denoted by $t_\nu^{(+)} - t_\nu^{(-)}$ in section 5.2.1), we consider a set of neutrinos to be temporally coincident if all neutrinos arrive within a Δt_ν time interval.

For spatial coincidence, we require that all neutrinos have a common direction of origin from where each neutrino can originate with probability above a threshold $P_{min} = 0.05$ (i.e. if the probability that a neutrino came from a direction farther from its reconstructed direction than the common direction is $\leq P_{min}$). This probability threshold corresponds to an angular difference threshold $\Delta\overrightarrow{x}^{max}_{s,i}$ between the common direction and the neutrino direction ($\Delta\overrightarrow{x}^{max}_{s,i} = \sigma_i\sqrt{2\ln(1/P_{min})}$. The average angular difference threshold for IceCube-22 neutrinos is $\sim 2.5°$ for $P_{min} = 0.05$). Neutrinos i and j will be spatially coincident if their angular distance is $\leq (\Delta\overrightarrow{x}^{max}_{s,i} + \Delta\overrightarrow{x}^{max}_{s,j})$.

To take into account more than one neutrino in the joint GW+HEN significance, one needs to account for the probability of detecting a certain number of neutrinos from the background. The distribution of the number of neutrinos expected for astrophysical signals is model-dependent due to the non-homogenous source distribution, and is in general unknown. However, the probability of background neutrinos to occur in the same time window can be calculated. Given that we have at least one detected neutrino, the probability of detecting N neutrinos in the allowed time window is $\mathrm{Pois}(N-1; f_\nu \Delta t_\nu)$, where f_ν is the background neutrino rate (its typical value is $\sim 10^{-4}$ Hz for IceCube-22 and $\sim 10^{-2.5}$ Hz for the completed IceCube). We calculate the p-value for one neutrino to be in a time-window with N or more neutrinos to be

$$p_{cluster}(N) = 1 - \sum_{i=0}^{N-2} \mathrm{Pois}(i; f_\nu \Delta t_\nu). \tag{5.6}$$

This p-value is additionally taken into account to the other p-values in the joint test statistic. Note that, if one has only one detected neutrino in the cluster, $p_{cluster}(1) = 1$.

Note that the decision of whether to treat coincident neutrinos as a cluster or as individual events is made by the analysis based on which combination yields the highest significance (this decision process can proceed iteratively on the remaining neutrinos until all are accounted for).

5.1.4 Astrophysical Source Distribution - the Galaxy Catalog

The distribution of astrophysical GW+HEN sources at detectable distances is not uniform. This can be used in a joint search algorithm to increase sensitivity. One can weigh event candidates based on the expected source density in their direction. The density of proposed GW+HEN sources can be connected to the blue luminosity of galaxies [421, 422], while source density can also depend on, e.g., the galaxy type [423, 424]. We take the blue-luminosity distribution of galaxies up to 40 Mpc from the Gravitational Wave Galaxy Catalogue (GWGC) [250].

Let the astrophysical GW+HEN source density be $\rho(r, \overrightarrow{x})$, where r and $\overrightarrow{x} = (\phi, \theta)$ are the source distance and direction on the sky, respectively. The probability distribution of astrophysical neutrinos as a function of direction is proportional to the number of sources in the given direction, weighted with the distance of the sources to the -2^{nd} power (which cancels out in the volume integral):

$$\mathcal{F}_{gal}(\overrightarrow{x_s}) = \frac{1}{N_\nu} \int_0^{D_{horizon}} \rho(r, \overrightarrow{x_s}) \mathrm{d}r \tag{5.7}$$

where N_ν is a normalization factor, $\overrightarrow{x_s}$ is the source direction and $D_{horizon}$ is an expectation-motivated cutoff distance (see, e.g., [425, 250, 40]). For HEN searches, $D_{horizon}$ can be chosen to be very large, however for joint GW+HEN searches $D_{horizon}$ will be chosen to be the cutoff distance related to GW detection (see below). For searches using initial GW detectors, a reasonable choice can be $D_{horizon} = 40$ Mpc. Given the detector sensitivities

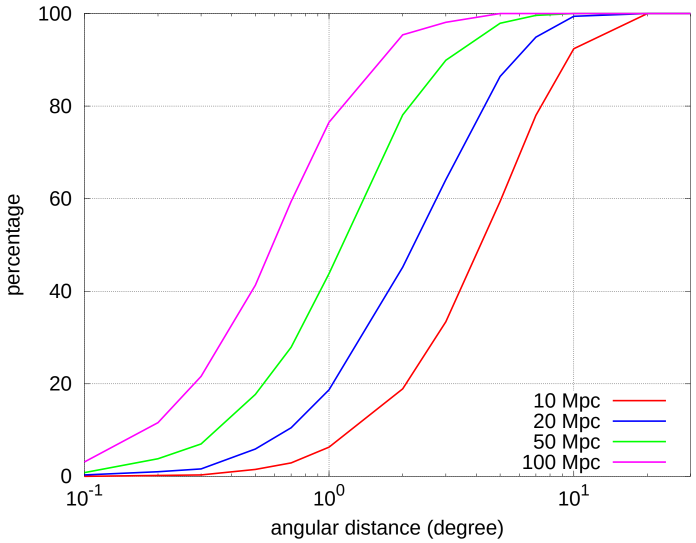

Figure 5-1: Probability that a random sky direction falls by chance within a given angular distance of at least one of the nearby galaxies listed in the GWGC.

and typical source strengths, sources of interest father than this distance are unlikely to have measurable effect. In the following we will refer to this distribution as the weighted galaxy distribution.

To take into account the galaxy distribution in the joint analysis, we consider our null hypothesis to be that the joint signal is a random coincidence from the background, i.e. it has no directional preference. This results in a background likelihood of

$$\mathcal{B}^{(i)}_{gal} = \frac{1}{2\pi}, \tag{5.8}$$

where we take into account that a joint event can only come from half of the sky due to the directional sensitivity of neutrino observatories. The alternative hypothesis is that the joint event came from an astrophysical source at direction $\overrightarrow{x_s}$. The corresponding signal likelihood is

$$\mathcal{S}^{(i)}_{gal}(\overrightarrow{x_s}) = \mathcal{F}_{gal}(\overrightarrow{x_s}). \tag{5.9}$$

The information on the distribution of galaxies is accurate for directions outside the galactic plane. Within the plane, the large density of galactic stars makes it more difficult to detect galaxies in these directions. This incompleteness needs to be taken into account in our perceived source distribution. Another complication is that nearby galaxies can be smeared to a finite area of the sky. We ensure that no source is missed due to these incompletenesses by performing a complementary search with no galactic weighing. Such a search, while being significantly less sensitive than a search that takes into account the galaxy catalog, is capable of detecting strong sources that are not aligned with the galaxy catalog. For this case, the galactic likelihood ratio is uniformly taken to be unity.

To illustrate the capabilities of using the galaxy catalog in rejecting false GW+HEN coincidences, we calculated the probability that a random sky direction is within a given angular distance from at least one galaxy in the galaxy catalog. This is a simpler and less sensitive way of utilizing information on galaxy locations than used in the method (which includes the blue-luminosity weight), but it already shows the usefulness of this additional information in background rejection. The results are shown in Figure 5-1. The probability of the coincidence of a random sky direction and at least one galaxy is evaluated for angular distances ranging from 0.1 to 10 degrees and considering galaxies with four different horizon distances from the observer. For these curves, it is possible to estimate the probability that a background neutrino be falsely associated with a host galaxy. We see that for an horizon distance of 50 Mpc (which is larger than the 40 Mpc used in the present analysis), there is one chance in two to get a false association if the position uncertainty is of order of one degree. The efficiency of the galaxy catalog to discard background neutrino triggers is directly connected to this probability (since background neutrinos coming from directions where there is no galaxy can be discarded). This result indicates that, within the 40 Mpc distance horizon, most background GW+HEN events will be farther from any galaxy than the typical angular uncertainty of HEN direction reconstruction, demonstrating the benefit of using the galaxy catalog, even for this simple model.

5.2 Joint GW+HEN Analysis

This section describes the joint analysis method for the search for GW+HEN signals. The joint analysis is described with a flow diagram in Fig. 5-2. For easier navigation the different steps in the flow diagram include references to the sections and figures where they are described in detail.

While the presented search example focuses on GWs and HENs, we note that it is straightforward to use the method with other messengers as well. The method also naturally incorporates externally triggered searches (see e.g. [241, 78]), where at least one messenger confirms the presence of an astrophysical signal. A confirmed signal can define either or both the time window and source location (or point spread function) which restricts the parameter space of the multimessenger search a-priory. For such cases the interesting scientific question is whether additional information is present in other messengers, and if it is then what can one infer about the source by the total available information. We also note that the search can be analogously used for much lower energy neutrinos. For instance because the photomultipier tube (PMT) dark noise rate is particularly low in ice, the IceCube detector has sensitivity to sudden fluxes of MeV neutrinos which lead to collective rise in the PMT rates. Nearby supernovae up to 50 kpc are expected to be detected this way. While the MeV neutrino signal does not provide any directional information, it can be readily naturally incorporated in the present joint analysis by using its time of arrival and significance (i.e. flux). The lack of directional information can be taken into account as a uniform sky distribution. Further, similarly to the blue-luminosity-weighted galaxy distribution, a-priori source source distribution can be used for nearby sources as well, for example in the form of the matter distribution within the Milky Way. Galactic sources behind the center of the Milky Way can be especially interesting for multimessenger searches since they are difficult to observe electromagnetically.

5.2.1 Coincidence Time Window

The maximum time difference between the arrivals of the observed GW trigger and HEN events is one of the key parameters of the joint GW+HEN search algorithm [238]. A too small time window might exclude some potential sources, while a too large time window would unnecessarily increase the false alarm rate and the computational cost.

Here, we adopt a conservative arrival time difference of ±500 s described in Section 3.1. Multiple neutrino events and a GW trigger are considered temporally coincident if the greatest time difference between any two of these neutrinos, or any neutrino and the GW

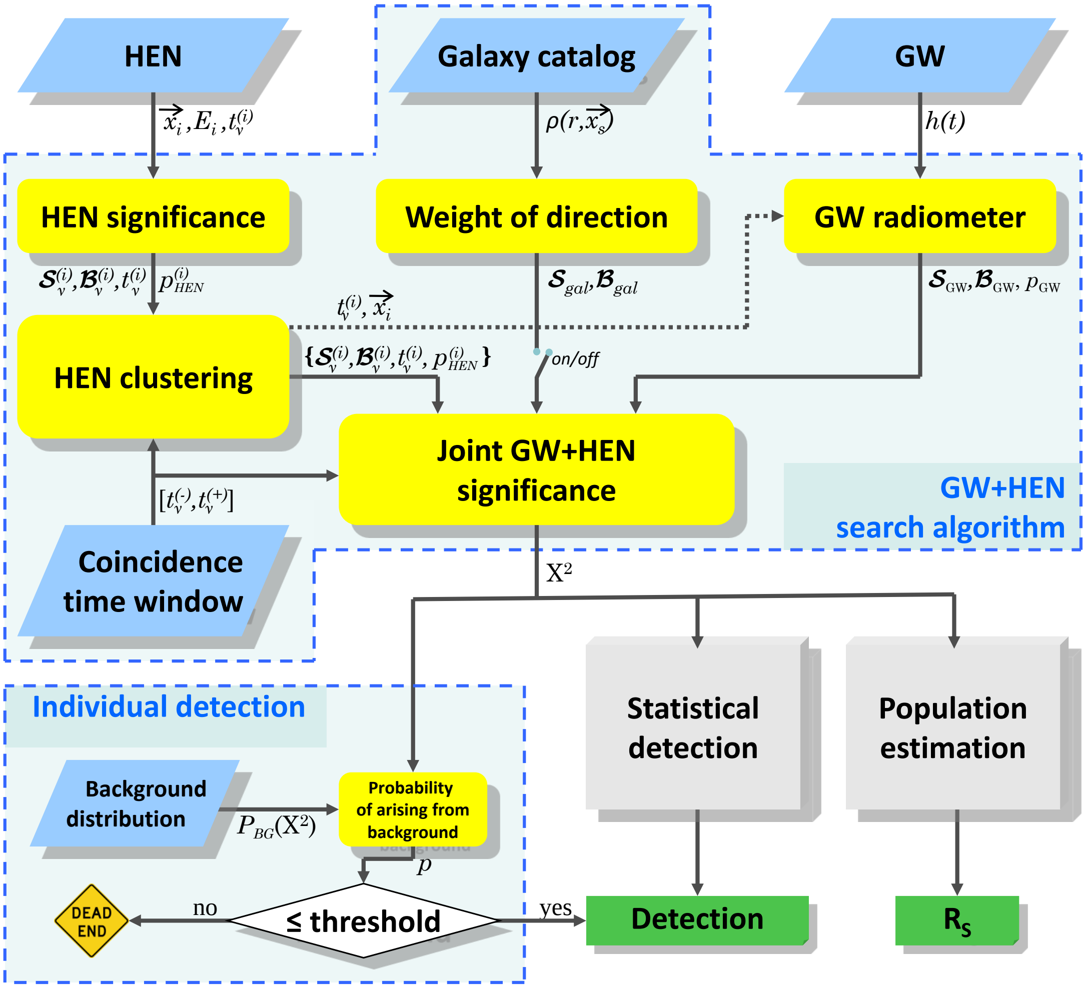

Figure 5-2: Flow diagram of the joint GW+HEN search algorithm. Steps include references to the sections and/or Figures in which they are described in details.

trigger, is less than 500 s.

We consider only one GW transient (trigger) per astrophysical GW+HEN source (we choose the GW trigger that gives the maximum joint significance; see below). Besides determining temporal coincidence, we apply no additional weight based on the arrival times of the HEN events and GW trigger (while the flux of neutrinos is probably time dependent, the uniform weight reflects our lack of information about this time dependence; see, e.g, [426]).

5.2.2 Joint GW+HEN Significance

The joint significance combines the significances of the GW, HEN, and galaxy distribution components. For the directional distribution of these components, there exists a signal hypothesis, and therefore they are assigned a likelihood ratio. The other components of the GW and HEN events (e.g. energy) have no model-independent signal hypotheses, therefore they are assigned a p-value. These two types of information are combined into one joint significance measure.

First, we combine the likelihood ratios of the directional components to obtain a significance measure, i.e. p-value. The joint likelihood ratio $\mathcal{L}(\overrightarrow{x_s})$ is defined as

$$\mathcal{L}^{(i)}(\overrightarrow{x_s}) = \frac{\mathcal{S}^{(i)}_{\mathrm{GW}}(\overrightarrow{x_s})\mathcal{S}^{(i)}_{gal}(\overrightarrow{x_s})\prod_{\{j\}}\mathcal{S}^{(j)}_{\nu}(\overrightarrow{x_s})}{\mathcal{B}^{(i)}_{\mathrm{GW}}\mathcal{B}^{(i)}_{gal}\prod_{\{j\}}\mathcal{B}^{(j)}_{\nu}}, \tag{5.10}$$

where $\{j\}$ is the set of neutrinos within GW+HEN trigger i. Note that the joint likelihood ratio, as it combines the directional distributions, is defined as a function of direction. Example directional distributions are shown in Fig. 5-3. Since we are mainly interested in the significance of the signal being of astrophysical origin, we treat the direction as a nuisance parameter and marginalize over it. Since the background likelihoods are uniform over the sky, the marginal likelihood ratio is

$$\mathcal{L}^{(i)} = \int \mathcal{L}^{(i)}(\overrightarrow{x_s})\mathrm{d}\overrightarrow{x_s} \tag{5.11}$$

The background distribution of $\mathcal{L}$, $P_{\mathrm{BG}}(\mathcal{L})$, can be obtained from time scrambled data (see section 5.2.3). Using this distribution, the p-value p_{sky} of the directional part of the joint event can be calculated as

$$p_{sky}^{(i)} = \int_{\mathcal{L}^{(i)}}^{\infty} P_{\text{BG}}(\mathcal{L}')\text{d}\mathcal{L}'. \tag{5.12}$$

We follow Fisher's method in combining the p-values into one joint test statistic:

$$X_i^2 = -2\ln\left[p_{sky}^{(i)} p_{\text{GW}}^{(i)} p_{cluster}(N) \prod_{\{j\}} p_{\text{HEN}}^{(j)}\right] \tag{5.13}$$

To ensure that possible correlations between the different p-values do not affect the outcome, we calculate the significance of X^2 by calculating its p-value from its background distribution $P_{\text{BG}}(X^2)$ in time-scrambled data (see section 5.2.3):

$$p_{\text{GWHEN}}^{(i)} = \int_{X_i^2}^{\infty} P_{\text{BG}}(X^{2'})\text{d}X^{2'}. \tag{5.14}$$

Note that, for a given joint event, we consider the single HEN or cluster of HENs with only one GW trigger at a time. If there are more GW triggers coincident with a given HEN trigger, we treat them as separate joint events (combined with the same neutrino).

To take into account possible sources outside of galaxies and in the Milky Way (or in galaxies not included in the used galaxy catalog), we perform an additional search without using the galaxy distribution. This is done simply by taking $\mathcal{F}_{gal}$ to be unity over the whole sky. This additional search without the galaxy catalog is represented by the on/off switch of the galaxy information in the flow diagram in Figure 5-2.

5.2.3 Background Trigger Generation

In order to calculate the significance of one or more joint signal candidates, we compare their test statistic X^2 to the test statistic distribution of background coincident triggers. The steps of the generation of the background distributions are described below, and are also shown in Figure 5-4.

For a set of GW and HEN detectors, we apply time shifts for background event generation. For GW detectors the time shifts between any two detector data streams are selected to be much greater than the maximum possible time shift for an astrophysical signal. For neutrino detectors the time of arrivals are scrambled between neutrinos, keeping each event's local

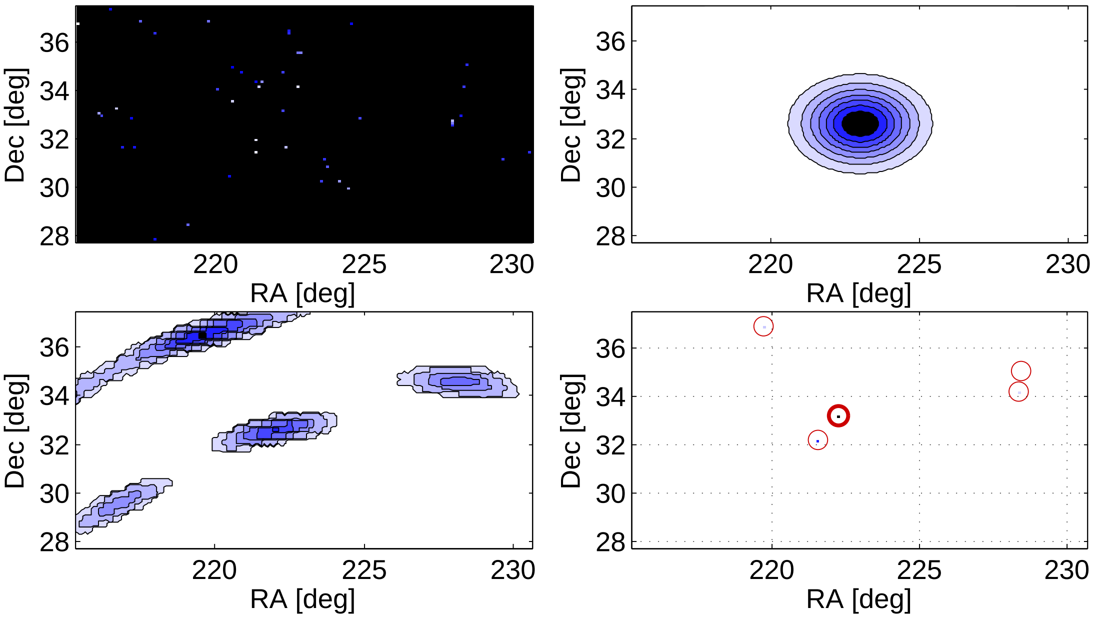

Figure 5-3: Example likelihood distributions as parts of the joint likelihood ratio: weighted galaxy distribution (upper left), HEN directional probability distribution function (PDF) (upper right), GW PDF (lower left) and joint PDF (lower right). The joint PDF is the product of the other three PDFs. The scales are in arbitrary units, and the color-scale for the galaxy distribution is inverted. On the joint PDF plot, every galaxy for which the joint PDF is non-zero is circled for visibility. The reconstructed source direction with the maximum significance is circled with bold line.

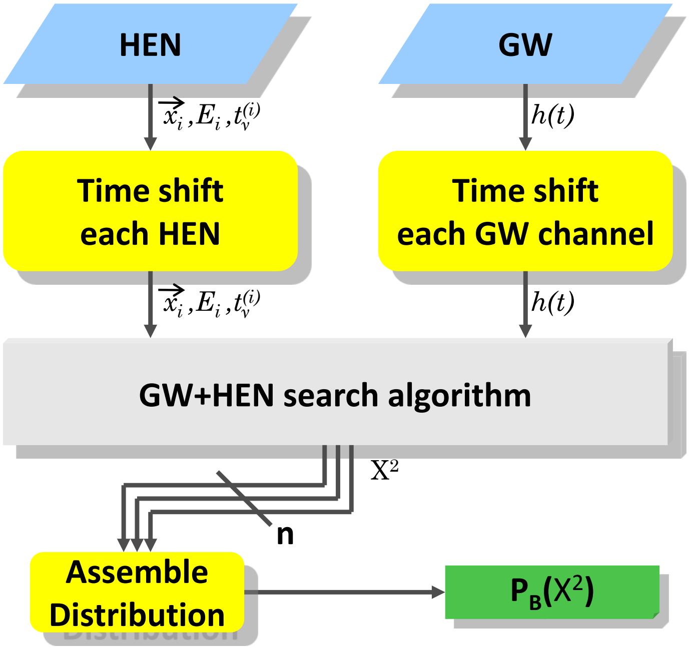

Figure 5-4: Flow diagram of the calculation of the background likelihood distribution $P_B(X^2)$.

coordinates (θ, ϕ) and energy fixed during the scrambling. This procedure reproduces fairly well the distribution of background neutrino parameters, and also preserves the geometric acceptances of the GW and HEN detectors which are fixed with respect to each other.

Using the background data described above, one can calculate the test-statistic distribution of background triggers similarly to how it is done for real data with no time shifts (see Eq. (5.14)).

5.2.4 Individual Detection

The loudest GW+HEN event in real data will be considered a joint detection if its probability of arising from the background during a one year long measurement period is less than 2.87×10^{-7} (one-sided 5σ).

We consider the joint GW+HEN to have discovery potential for a given GW+HEN flux measured at Earth from an astrophysical source if such a signal has 50% probability of resulting in a joint detection (as defined above).

We define the median upper limit of the joint GW+HEN search to be the joint GW+HEN flux at Earth, in terms of h_{rss} and $\langle n \rangle$, for which X^2 is greater, with 90% confidence, than the median of the loudest events among sets of N randomly generated joint background events.

To evaluate the statistical significance of a single GW+HEN event with X^2, we compare it to the background X^2 distribution $P_{\mathrm{BG}}(X^2)$ as described in section 5.2.3. The statistical significance of a X^2 value is given by its p-value (Eq. 5.14).

5.2.5 Statistical Detection of Multiple Sources

Besides detecting a single astrophysical GW+HEN joint event, one can try to indicate the presence of multiple astrophysical joint events statistically. For such statistical detection, we compare the distribution $P_{\mathrm{S}}(X^2)$ of the real data to the distribution $P_{\mathrm{BG}}(X^2)$ of joint background events. We use the realistic assumption that only a small fraction of the signal candidates can be due to actual astrophysical signals. The steps of statistical detection described below are also shown in Fig. 5-5. Two alternative statistical tests can be found, e.g. in [344].

If only a small fraction of the joint events in real data are from astrophysical sources, one has the best chance of detecting the presence of real astrophysical signals by looking at the highest X^2 values. We therefore select a X^2 threshold above which the real-data and background distributions are compared. We denote this threshold by X_t^2. This threshold is chosen based on the background neutrino event rate, and the estimated astrophysical neutrino event rate within the distance in which the GW+HEN search is sensitive.

We compare the distributions of real and time-shifted data above X_t^2 in the following manner. Let p_t be the p-value corresponding to X_t^2. We introduce the product $\mathfrak{p}$ for a set of p-values which are above threshold p_t. The value $\mathfrak{p}$ can be written as

$$\mathfrak{p} = \prod_{p_{\mathrm{GWHEN}}^{(i)} > p_t} p_{\mathrm{GWHEN}}^{(i)} \tag{5.15}$$

where $p_{\mathrm{GWHEN}}^{(i)}$ is the p-value of measurement i (see Eq. 5.14). Similarly to the use of p-values for the single detection case, we calculate the probability $p^{\mathfrak{p}}$ that the measured $\mathfrak{p}$ from real

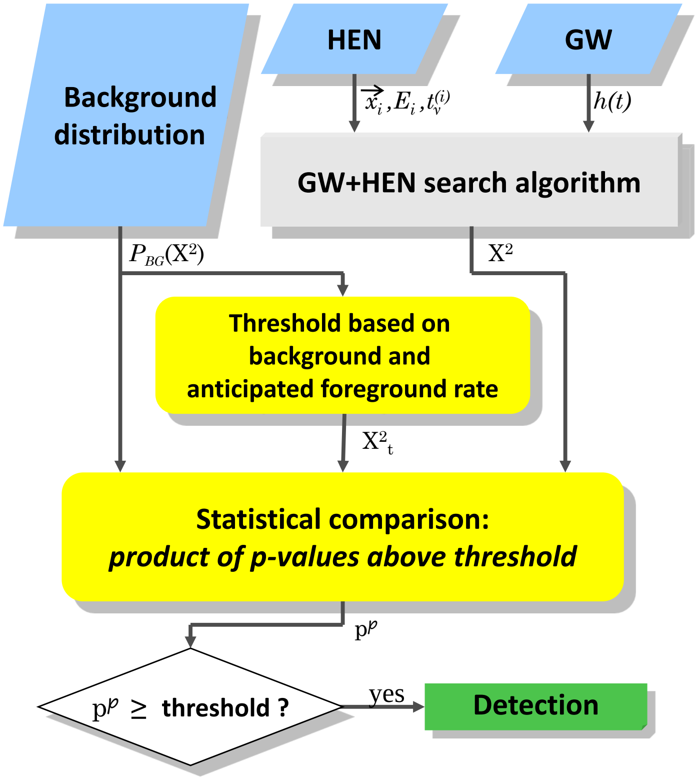

Figure 5-5: Flow diagram of the statistical detection of multiple GW+HEN sources.

data can arise from the background:

$$p^{\mathfrak{p}} = \int_0^{\mathfrak{p}} P_{\text{BG}}(\mathfrak{p}')\text{d}\mathfrak{p}', \tag{5.16}$$

where $P_{\text{BG}}(\mathfrak{p})$ is the probability distribution of $\mathfrak{p}$ on time-shifted data (of identical duration as real data). The value $p^{\mathfrak{p}}$ is therefore the probability that the product of the p-values smaller than p_t from real data arose from the background. We use $p^{\mathfrak{p}}$ to characterize the significance of statistical detection. We claim statistical detection if the probability that the real-data $p^{\mathfrak{p}}$ arose from the background during one year of measurement is less than 2.87×10^{-7} (one sided 5σ).

5.2.6 Simulation of Astrophysical Signals

We use simulated astrophysical signals to characterize the sensitivity of the GW+HEN search algorithm. The simulation is designed such that the results are scalable for different GW and HEN emission fluxes, therefore our results can be used to constrain the parameter space of GW and HEN emissions. We simulate standard GW+HEN sources with identical intrinsic GW+HEN emission (energy and spectrum). Upper limits for such standardized source populations are conservative estimates, taking the average emission, compared to taking a distribution of emission energies.

For the simulations we assume that zero or one HEN event is detected from each source. This is the likely situation for the part of the HEN parameter space that is not constrainable by a km^3 HEN detector alone.

The simulation of an astrophysical joint event consists of the following steps.

1. For a given direction, generate a simulated astrophysical HEN event coming from the source direction. We use Monte Carlo simulations to generate a random reconstructed energy and directional uncertainty for such a neutrino, using a source neutrino energy spectrum. We then generate a reconstructed source direction for the neutrino, drawn from a 2D Gaussian distribution centered around the real source direction, with standard deviation obtained from the Monte Carlo simulation.

2. Generate simulated astrophysical GW event coming from the source direction. We inject a GW signal with a given amplitude and waveform into real GW data into each GW detector used in the analysis, taking into account the direction of the source. The amplitude of the injected GW is chosen from a range that covers the amplitude region of interest for the joint search.

5.2.7 Population Estimation

We define <u>population upper limit</u> for the joint emitters of GWs and HENs as the lowest population which would produce – with $> 90\%$ probability, a joint event with higher significance than the loudest GW+HEN event in real data.

We obtain population estimates by calculating the probability of detection rate for every galaxy. We adopt the following notation: for an astrophysical source in galaxy i, the galaxy has blue luminosity $L_B^{(i)}$ and is at a distance r_i. Further, let $L_{\mathrm{B}}^{\mathrm{MW}}$ be the blue luminosity of the Milky Way, R the source rate [per year per MWE galaxy], T_m the measurement duration, and f_b the neutrino beaming factor of the source. The calculation is the following.

Given an astrophysical source in galaxy i, the probability that at least one HEN will be detected from this source is [13]

$$p(n \geq 1 | r, n_{\mathrm{HEN}}) = 1 - F_{poiss}\left(0 | (10\ \mathrm{Mpc}/r)^2 n_{\mathrm{HEN}}\right), \tag{5.17}$$

where F_{poiss} is the Poisson cumulative distribution function, and n is the number of detected neutrinos from the source. Therefore for galaxy i the average number $\widehat{N}_i$ of sources with at least one detected neutrinos during the measurement will be

$$\widehat{N}_i(R, T_m) = p(n \geq 1 | r_i, n_{\mathrm{HEN}}) \cdot R/f_b \cdot T \cdot L_{\mathrm{B}}^{(i)}/L_{\mathrm{B}}^{\mathrm{MW}}. \tag{5.18}$$

The population upper limit is obtained from $\widehat{N}_i(R, T_m)$ by requiring the total number of detected neutrinos within D^{GWHEN} to be 2.3 during a one year long measurement. This is done by summing $\widehat{N}_i(R, T_m)$ over all galaxies on the hemisphere in which the neutrino detector is sensitive. For IceCube this is $\delta_i \geq 0$ where δ_i is the declination of galaxy i. The population upper limit will be

$$R^{\mathrm{UL}}(E_{\mathrm{GW}}^{iso}, n_{\mathrm{HEN}}) = \frac{2.3 f_b L_{\mathrm{B}}^{\mathrm{MW}}}{T_m \sum_{\{r_i > D^{\mathrm{GWHEN}}, \delta_i \geq 0\}} \epsilon_{\mathrm{GW}}(r_i) p(n \geq 1 | r_i, n_{\mathrm{HEN}}) L_{\mathrm{B}}^{(i)}}, \tag{5.19}$$

where $\epsilon_{\mathrm{GW}}(r_i)$ is the detection efficiency of the GW detector network at distance r_i [6].

5.3 Science Reach

In this section we investigate the constraints one can introduce with the GW+HEN search on the population of astrophysical GW+HEN sources. Below we first estimate the expected population upper limits from the GW+HEN search as a function of source parameters, after which we interpret these constraints. The science reach analysis presented here follows the

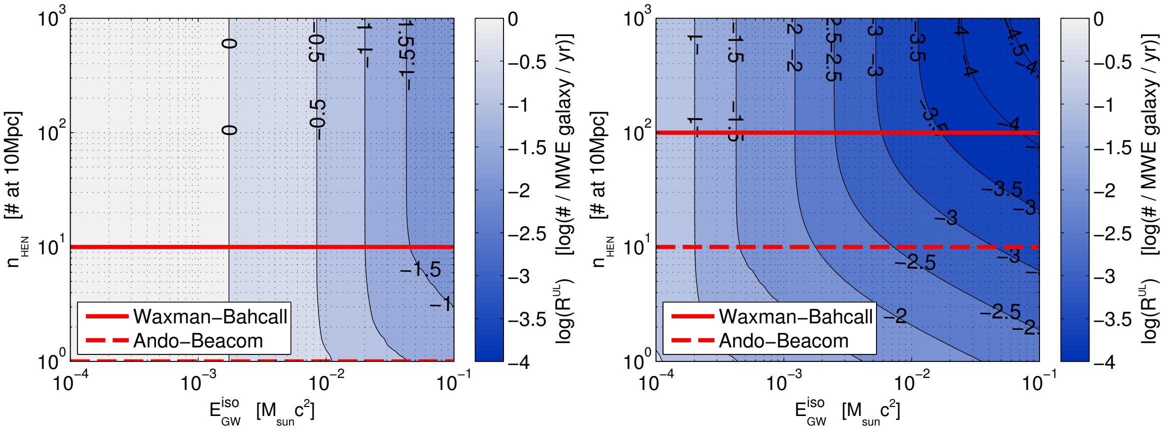

Figure 5-6: Expected GW+HEN source population upper limits for IceCube-22 coincident with initial LIGO-Virgo (left) and IceCube-86 coincident with advanced the LIGO-Virgo detectors (right; courtesy of [13]), with one year of coincident measurement time. The results take into account the blue-luminosity-weighted galaxy distribution. The x-axis represents the GW energy output of a standard source. The y-axis represents the number of detected neutrinos from a standard source at 10 Mpc. The color scale shows the obtained source rate upper limit R^{UL} in logarithmic units of number of sources per (Milky Way equivalent) galaxy per year. On both plots, the two horizontal lines (scaled for detector sensitivity) show the Waxman-Bahcall emission model [14] (higher) and the HEN emission model of Ando and Beacom [9] for reverse shocks in mildly relativistic supernova jets / choked GRBs (lower).

calculations in Section 3.2 (see also Ref. [13]), that we outline below.

In determining the GW+HEN population upper limit we assume standard GW+HEN sources with the same intrinsic emission. Limits based on a fixed average brightness are conservative compared to those using any other brightness distribution. We consider maximum one HEN detected for each source. This is a reasonable (and conservative) assumption given that there has been no discovery with neutrino detectors. We introduce the exclusion distance $D_{50\%}^{\rm GWHEN}$, which is the maximum distance that satisfies the following criterion: for an astrophysical GW+HEN burst at a distance $< D_{50\%}^{\rm GWHEN}$ in a typical direction and with one detected HEN, the probability that it is more significant (Eq. 5.14) than the loudest observed event of the GW+HEN search is $\geq 50\%$. This distance depends on the total (isotropic-equivalent) energy emitted in GWs (E_{GW}^{iso}) of a GW+HEN source. Using this distance, we calculate the minimum astrophysical GW+HEN source rate (i.e. population) that would have produced at least one detected astrophysical HEN signal with $\gtrsim 90\%$ probability. This source rate will be the rate upper limit.

To estimate the expected results with the GW+HEN search, we approximate the sensitivity of the GW+HEN algorithm with that of published externally triggered GW searches (e.g. [345, 427]). This is a reasonable (and conservative) approximation if one chooses the threshold for GW and HEN trigger selection such that there will be $O(1)$ spatially and temporally coincident GW and HEN signals for the duration of the measurement. In an externally triggered search for GW bursts in coincidence with GRBs, Abbott et al. [345] obtained a median upper bound of $h_{rss}^{ext} \approx 3.8 \times 10^{-22}$ strain root sum square using the initial LIGO-Virgo GW detector network (S5/VSR1 science run). They used a sine-Gaussian waveform with characteristic frequency of ~ 150 Hz, which is in the most sensitive frequency band of the GW detectors. This upper limit corresponds to the minimal GW signal amplitude that, with 90% confidence, produces larger significance than the loudest joint GW+HEN event in the real data measured in coincidence with an external trigger. To estimate the performance of advanced detectors (Advanced LIGO-Virgo), we estimate their median strain upper bound as 0.1 times that of initial detectors (i.e. 3.8×10^{-23}). We note here that with additional advanced detectors, such as LIGO-Australia [428] and LCGT [429], the sensitivity of the GW detector network will further increase. For comparison, we note that the upper bound obtained with the all-sky GW search of Abadie et al. [6] for sine-Gaussian signals at ~ 150 Hz with the initial LIGO-Virgo detector network is $h_{rss}^{all-sky} \approx 6 \times 10^{-22}$. The all-sky search corresponds to the lower limit for the sensitivity of GW searches as no additional information is used besides GW data.

For the GW+HEN search we introduce the upper bound h_{rss}^{GWHEN}, and estimate this upper bound to be $h_{rss}^{\mathrm{GWHEN}} \approx h_{rss}^{ext}$. We assume that a GW signal with $h_{rss} \geq h_{rss}^{\mathrm{GWHEN}}$ in coincidence with a detected astrophysical HEN would be detected by the joint GW+HEN search with $\geq 90\%$ probability. Given h_{rss}^{GWHEN} (i.e. the amplitude at the detector) and E_{GW}^{iso} (i.e. the amplitude at the source), we can calculate the radius within which there was likely ($P \geq 90\%$) no GW+HEN event from which a HEN was detected. This distance, averaged over all directions on the sky, is [345]

$$D^{\mathrm{GWHEN}} = 12 \text{ Mpc} \left(\frac{E_{GW}^{iso}}{10^{-2} \text{ M}_{\odot}\text{c}^2} \right)^{1/2} \left(\frac{h_{rss}^{ext}}{h_{rss}^{\mathrm{GWHEN}}} \right) \tag{5.20}$$

From the fact that no astrophysical HEN was detected from a GW+HEN source within D^{GWHEN}, we obtain a source rate upper limit as the highest source rate that would have produced at least one detected neutrino within D^{GWHEN} with $\lesssim 90\%$ probability. Assuming a Poissonian source number distribution, this corresponds to an average source rate of 2.3 over one year long measurement. We denote this source rate upper limit by R^{UL}. To obtain R^{UL}, we calculate the average number of sources within D^{GWHEN} over the duration of the measurement from which at least one neutrino has been detected. R^{UL} will be the rate that corresponds to 2.3 detected sources on average. The rate depends on the blue-luminosity-weighted galaxy distribution within D^{GWHEN} (see section 5.1.4), as well as the neutrino flux (n_{HEN}) from a standard source.

The estimated source rate upper limit is dependent on the beaming of HEN emission (beaming is less significant for GWs). The beaming of HEN emission is uncertain, but it is probably similar to the beaming of gamma rays, as the two emission mechanisms are connected. For this reason we use the gamma-ray beaming factor obtained for LL-GRBs, estimated to be less than 14 [227]. The obtained upper limits scale linearly with the beaming factor (since we only expect to see sources for which the beam points towards us).

We calculate population upper limits for a range of GW isotropic emission E_{GW}^{iso} and neutrino emission n_{HEN}. The results are shown in Figure 5-6, both for initial and advanced detectors.

To interpret the science reach of the expected GW+HEN population upper limits described above, we consider the source parameters from some existing emission models. In Figure 5-6 horizontal lines indicate the neutrino rate predictions of the Waxman-Bahcall emission model [8], as well as the emission model for mildly relativistic jets by Horiuchi and Ando [178]. The population upper limit estimates for these two models specifically, as functions of E_{GW}^{iso} down to $E_{\mathrm{GW}} = 10^{-4}\ \mathrm{M}_{\odot}\mathrm{c}^2$, are shown in Figure 5-7. For sources of weaker GWs than $10^{-4}\ \mathrm{M}_{\odot}\mathrm{c}^2$ as predicted by some CCSN simulations [365, 430, 431], observations will focus on galactic sources.

We note here that recent upper limits from the IceCube detector disfavor GRB fireball models with strong HEN emission associated with cosmic ray acceleration. However, milder HEN fluxes or alternative acceleration scenarios are not ruled out [196]. Moreover, the

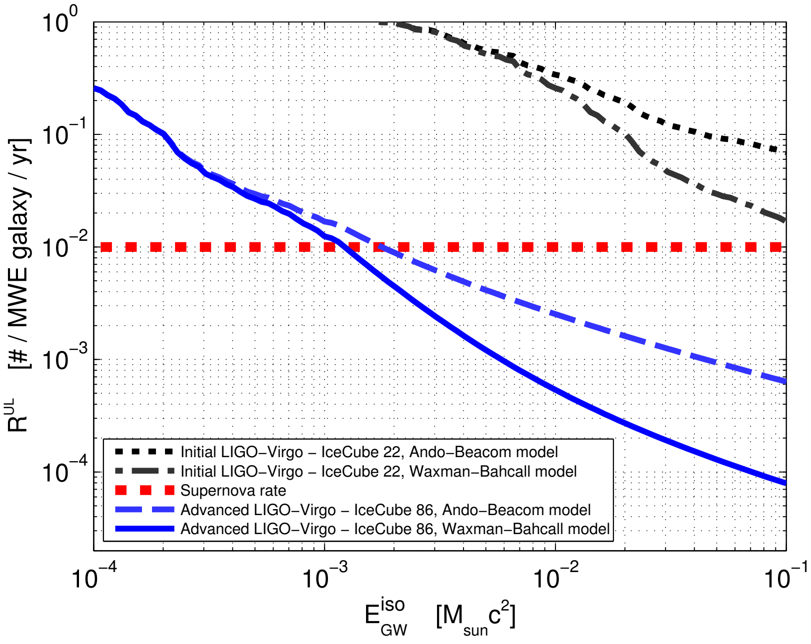

Figure 5-7: Expected GW+HEN source population upper limits for anticipated HEN emission from two emission models, as functions of isotropic-equivalent GW emission energy E_{GW}^{iso}. Results are shown both for measurements with the initial LIGO-Virgo detectors and the IceCube-22 detector (dashed line), as well as for the Advanced LIGO-Virgo detectors and the IceCube-86 detector (solid line), both with one year of coincident measurement time. For comparison, the galactic supernova rate is shown (dotted line). This Figure shows a subset of the results shown in Figure 5-6.

constraints weaken substantially when uncertainties in GRB astrophysics and inaccuracies in older calculations are taken into account, and the standard fireball picture remains viable [304, 305].

5.3.1 Estimated Sensitivity

In Section 5.3 we estimated the science reach of the baseline multimessenger analysis following the calculations presented in Section 3.2 (see also Ref. [13]). In estimating the science reach the single required parameter from the search algorithm was its exclusion distance $D_{50\%}^{\mathrm{GWHEN}}$. We approximated this parameter for the analysis by assuming that it will be comparable to the horizon distance of externally triggered GW searches. In the externally triggered GW search of Abbott et al. [345], the authors give the median horizon distance for single GW events coincident with electromagnetically observed GRBs. This horizon distance is related to the expected loudest GW background event from a given direction within a given time window of ~ 100 s. The approximation of $D_{50\%}^{\mathrm{GWHEN}}$ for the baseline multimessenger search is reasonable if, given the number of HENs, the GW triggers' significance threshold is chosen such that the expected number of spatially and temporally coincident GW+HEN events is $\lesssim 1$. For one coincident event the remaining difference between the GW-GRB externally triggered search and the GW+HEN multimessenger search is mainly due to the greater directional uncertainty of neutrinos ($\sim 1^\circ$) compared to the much better directional accuracy of electromagnetic GRB measurements. This difference, however, will not be significant, as the directional accuracy of GW measurements [$\mathrm{O}(10^\circ)$] is much worse that of the HEN directional accuracy (see e.g. [334, 332]). Further, the GW+HEN multimessenger analysis additionally takes into account the significance of HENs based on their reconstructed energy (see Section 5.1.2) as well as the expected source distribution (see Section 5.1.4). Both of these pieces of additional information further increase the sensitivity of the search, making the comparison to results from externally triggered GW searches conservative.

To estimate the validity of the approximation that one will have $\lesssim 1$ joint event in a measurement without significant constraints on the rate of GW triggers, we take the example of the initial LIGO-Virgo detectors during their S5/VSR1 science run and the partially completed IceCube detector in its 22-string configuration. The LIGO-Virgo-IceCube network ran in coincidence from May 31, 2007 until Sept. 30, 2007 (123 days). IceCube-22, during its full run of 275.7 days, collected a final sample of 5114 neutrino candidate events [432], of which ~ 1000 occur during the coincident livetime of the LIGO-Virgo-IceCube network. Considering a characteristic GW point spread function that spreads over 100 deg^2, the probability that temporally coincident GW and HEN triggers are also spatially coincident is $\sim 0.5\%$. To reach on average ≈ 1 spatially and temporally coincident joint event during the measurement, we need on average 1 GW trigger for every 5 HEN triggers, corresponding to a GW trigger frequency of 17 day^{-1}. This limit is far from limiting the sensitivity of the search. For comparison, ~ 1 GW trigger/day was used for electromagnetic follow-up observations for the latest LIGO-Virgo (S6/VSR2-3) science runs [248].

Comparing the expected population upper limit of the GW+HEN multimessenger search to an all-sky GW search, the multimessenger search is expected to give stricter constraints on source population if its increased horizon distance compensates for HEN beaming (GWs are only weakly beamed). An approximate comparison is given by the ratio of the number of sources above the expected loudest-event threshold in each of the searches:

$$\frac{(D_{50\%}^{\mathrm{GWHEN}})^3/f_b}{(D_{50\%}^{\mathrm{GW}})^3/f_{b,\mathrm{GW}}}, \tag{5.21}$$

where $D_{50\%}^{\mathrm{GW}}$ is the horizon distance of an all-sky GW search and $f_{b,\mathrm{GW}}$ is the GW beaming factor. Taking $D_{50\%}^{\mathrm{GWHEN}} \approx 12$ Mpc from externally triggered GW searches [345], $D_{50\%}^{\mathrm{GW}} \approx 7.8$ Mpc from GW all-sky searches [13], $f_b \approx 14$ (an observational estimate for low-luminosity GRBs; [227]) and $f_{b,\mathrm{GW}} \approx 1.5$ (estimated value for inspirals or accretion-type GW emission; e.g. [134]), the ratio of detectable GW+HEN and GW events is ≈ 0.4, indicating that the number of sources excluded with the joint search is comparable to the number of those excluded with GW all-sky searches. Further, the sources probed by a joint search are mostly complementary to sources probed by an all-sky GW search. As the joint analysis is looking farther, it can potentially see sources missed by GW all-sky searches.

5.4 Closed box results

In the joint analysis we used data from the initial LIGO-Virgo detectors[1] (joint S5-VSR1 science run; Nov 4 2005 Oct 1 2007), and the partially completed IceCube (22 strings). The IceCube data consisted of 5114 detected high energy neutrino candidates [432], among which ~ 1200 was detected during the time when the two 4-km long LIGO detectors, Virgo, and the IceCube detector were operating together (a total of 76 days). To generate GW triggers using the LIGO-Virgo strain data, we used the Coherent Waveburst (CWb) pipeline [419]. We used those GW triggers only which corresponded to a false alarm rate of $FAR \leq 1\,\mathrm{day}^{-1}$. To obtain sufficient background, we time shifted data[2], and generated background triggers using CWb on this time shifted dataset as well. We used GW injections of sine-Gaussian waveform with characteristic frequencies at $\sim 150\,\mathrm{Hz}$, i.e. in the most sensitive frequency band of the LIGO-Virgo detectors.

The time shifted, as well as the injected GW and HEN triggers were analyzed using the search algorithm and technique presented above (Chapter 5). Fig. 5-8 shows the distribution of significances obtained for the background and injected GW+HEN events, the latter for different GW injection amplitudes (note that the neutrino injection amplitude is fixed to 1 detected neutrino; only those events are shown in the histogram for which there is spatial overlap between the different messengers, thus $X^2 \neq 0$). The results on the left are shown for gravitational wave strain root sum square

$$h_{rss} = \sqrt{\int \left(|h_+(t)|^2 + |h_\times(t)|^2\right) dt}, \tag{5.22}$$

where $h_+(t)$ and $h_\times(t)$ are the time dependent GW strain amplitudes described in Chapter

---

[1] This section discusses results that were obtained using LIGO, Virgo and IceCube observational data. Hereby we note that the review of the presented results has not yet been finished, therefore the results are not yet approved by these collaborations for publication.

[2] The standard method to generate background data for a network of GW detectors is to apply a time shift separately for data from each detector. Time shifts are designed such that no transient astrophysical signal (with duration $\ll 1\,\mathrm{s}$) can appear in coincidence in any two detectors. Given the duration of light travel time between the observatories, a real astrophysical signal can appear in data from different detectors with a time difference $< 40\,\mathrm{ms}$, therefore the time shifts are chosen to be much greater than this value (for the present search they are the chosen to be multiples of $5\,\mathrm{s}$). For GW triggers identified on such time-shifted data from a network of detectors, the lack of coincident astrophysical events in at least two of the detectors ensures that background GW triggers are minimally impacted by potential astrophysical signals.

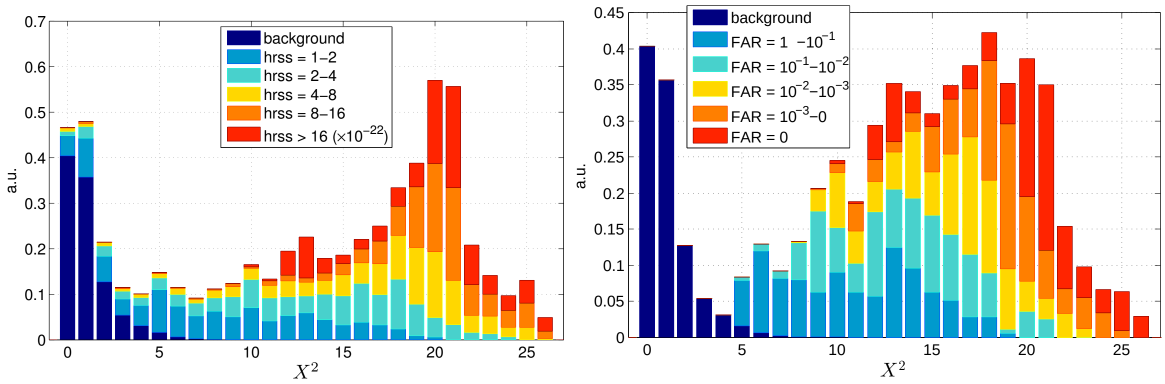

Figure 5-8: Histogram of the significance (X^2) of injected GW+HEN events as a function of the injected GW amplitude h_{rss} (left) and the false alarm rate (FAR) of the significance of the GW (right). FAR$<$ 0 corresponds to events with significances higher than the most significant background GW event. One can see, even for the smallest injection amplitudes considered here, injected events have a markedly shifted significance distribution, making them easier to distinguish from the background.

1.1. The figure shows that, as expected, events with greater injected GW amplitudes have increased significance. At the same time, as expected, the figure also shows that the FAR of the GW event is a better estimator than h_{rss} for the joint significance X^2 of the joint event.

To estimate the expected source rate upper limit of the analysis (given no detection), we calculated the probability of an injected signal with given h_{rss} value producing a greater X^2 significance than the maximum significance out of $\sim$ 100 temporally coincident simulated background events. The maximum of these $\sim$ 100 events is likely greater than what the maximum on-source event will be. The resulting probability is shown in Fig. 5-9. We note again that this plot solely estimates the expected source rate upper limit that can be derived from the open-box results (provided there is no detection). If we were to obtain, however, a similar $P(h_{rss})$ as shown in Fig. 5-9 from the on-source data, that would mean that our results are $\approx$ 50% better than the estimated sensitivity we used to project the obtainable upper limits in Section 5.3.

While the observational upper limits one can expect from the open box results are encouraging, here we point out that the main result of interest is the possibility of finding evidence to a joint GW-high energy neutrino signal. We refer the reader to our detection definition in Section 5.2.4. A major advantage of combining information from multiple messengers is that

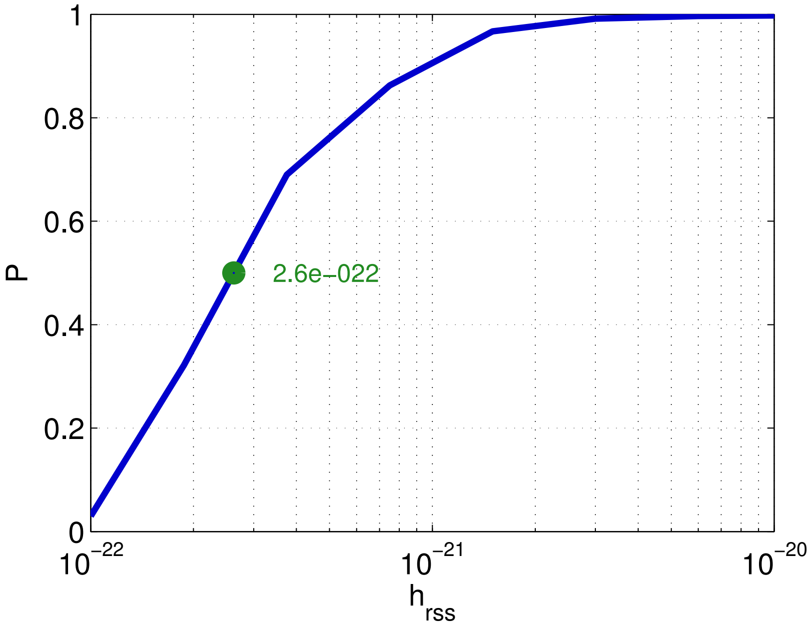

Figure 5-9: Probability of simulated GW+HEN events with significances X^2 greater than the greatest X^2 value out of 100 spatially and temporally coincident background events, as a function of injected GW signal amplitude (h_{rss}). The green dot represents the h_{rss} value for which the probability is 50%.

one can have significantly higher confidence in a detected event than if one only encountered a significant event from for a single messenger.

Conclusion & Outlook

We presented a variety of developments in gravitational wave astrophysics, from instrumentation to multimessenger searches, from a theoretical as well as an experimental perspective. On the instrumentation side, we presented the development, construction and testing of the Advanced LIGO Optical Timing Distribution System. This system is already installed as an integral part of the Advanced LIGO detectors, and will be implemented by other experiments, such as KAGRA, the Japanese gravitational wave interferometer currently under construction.

Our work on multimessenger astrophysics with gravitational waves, beyond aiming to improve search sensitivity, mainly focused on examining how multimessenger searches can add to our understanding of violent astrophysical processes. We studied mainly gamma ray bursts (GRBs), one of the most intriguing sources of gravitational waves. We outlined the different mechanisms that can drive GRBs from the perspective of their gravitational wave signature, and discussed how the observation of these engines via gravitational waves can complement our understanding of physics under extreme conditions. We further discussed multimessenger search strategies, as well as recent searches, aiming to observe GRBs via gravitational waves together with other messengers.

We further focused our attention on common sources of gravitational waves and high energy neutrinos. We derived the first observational constraints on their common sources, based on non-detection, with the initial LIGO/Virgo detectors and the partially completed IceCube neutrino detector. We compared our observational constraints to prevailing source models, and presented projected constraints for the upcoming advanced detector era.

To aid the work on the joint detection of gravitational waves and high energy neutrinos, we derived a model-motivated, observation-based upper limit on the coincidence time window for these two messengers from GRB progenitors. This work provided the basis for past and ongoing searches for common sources.

We examined how the detection of even a few high energy neutrinos can, under favorable conditions, add to our understanding of the progenitor structure that is responsible for emitting the neutrinos. Such understanding can be especially useful because we expect to see only a few neutrinos for the first detections, as well as for the majority of future detections.

We presented a multimessenger search algorithm designed to detect gravitational waves and high energy neutrinos from a common source. The analysis was designed to incorporate the probabilistic nature of the two messengers, given that the combined information can significantly increase our confidence in a detection, and given the weak nature of both messengers. Further, we incorporated information on the distribution of galaxies in the nearby universe, which is connected to the distribution of the source population. We point out that such a multimessenger search is especially interesting for source candidates that are difficult to detect through electromagnetic observations, such as the case of choked gamma ray bursts. We presented preliminary, closed box results from a joint search with the initial LIGO/Virgo and the partially completed IceCube detectors.

The presented work highlights some of the current directions of research in multimessenger astrophysics with gravitational waves. We demonstrated, under various circumstances, the utilization of information from joint searches in better understanding violent cosmic phenomena, such as gamma ray bursts. With the near completion of advanced gravitational wave observatories, the next few years shall be a very exciting period in our journey towards comprehending the Universe.

Bibliography

[1] K. Kiuchi, Y. Sekiguchi, M. Shibata, and K. Taniguchi, Physical Review Letters **104**, 141101 (2010), 1002.2689.

[2] T. Creighton, Classical Quantum Gravity **20**, 853 (2003).

[3] W. S. Paciesas and et al., Astrophys. J. Sup. **122**, 465 (1999).

[4] N. Gehrels, The Swift Gamma-Ray Burst Mission, in 5th INTEGRAL Workshop on the INTEGRAL Universe, edited by V. Schoenfelder, G. Lichti, and C. Winkler, , ESA Special Publication Vol. 552, p. 777, 2004.

[5] D. Burlon and et al., Astronomy and Astrophysics **505**, 569 (2009).

[6] J. Abadie et al., Phys. Rev. D **81**, 102001 (2010).

[7] R. Abbasi et al., ApJ, in press [arXiv1104.0075] (2011).

[8] E. Waxman and J. Bahcall, Physical Review Letters **78**, 2292 (1997), arXiv:astro-ph/9701231.

[9] S. Ando and J. F. Beacom, Phys. Rev. Lett. **95**, 061103 (2005).

[10] R. Gandhi, C. Quigg, M. H. Reno, and I. Sarcevic, Phys. Rev. D **58**, 093009 (1998).

[11] S. E. Woosley, A. Heger, and T. A. Weaver, Rev. Mod. Phys. **74**, 1015 (2002).

[12] A. Heger, S. E. Woosley, and H. C. Spruit, Astrophys. J. **626**, 350 (2005).

[13] I. Bartos, C. Finley, A. Corsi, and S. Márka, Phys. Rev. Lett.**107**, 251101 (2011).

[14] D. Guetta, D. Hooper, J. Alvarez-Mun˜Iz, F. Halzen, and E. Reuveni, Astropart. Phys. **20**, 429 (2004).

[15] A. Einstein and N. Rosen, Journal of The Franklin Institute **223**, 43 (1937).

[16] L. D. Landau and E. M. Lifshitz, The classical theory of fields (Pergamon Press, 1971).

[17] C. W. Misner, K. S. Thorne, and J. A. Wheeler, Gravitation (San Francisco: W.H. Freeman and Co., 1973).

[18] P. Hraskó, Theory of Relativity (in Hungarian) (Typotex, 2002).

[19] A. Einstein, Annalen der Physik **354**, 769 (1916).

[20] A. Einstein, Annalen der Physik **322**, 891 (1905).

[21] A. Einstein, Sitzungsberichte der Königlich Preußischen Akademie der Wissenschaften (Berlin), Seite 688-696. , 688 (1916).

[22] A. Einstein, Sitzungsberichte der Königlich Preußischen Akademie der Wissenschaften (Berlin), Seite 154-167. , 154 (1918).

[23] R. A. Hulse and J. H. Taylor, Astrophys. J. Lett. **195**, L51 (1975).

[24] I. H. Stairs et al., Astrophys. J. **505**, 352 (1998), arXiv:astro-ph/9712296.

[25] W. H. Lee and E. Ramirez-Ruiz, New Journal of Physics **9**, 17 (2007), arXiv:astro-ph/0701874.

[26] M. D. Duez, Classical and Quantum Gravity **27**, 114002 (2010), 0912.3529.

[27] B. Zhang, ArXiv e-prints (2012), 1204.4919.

[28] K. D. Kokkotas, ArXiv e-prints (2008), 0809.1602.

[29] J. M. Lattimer and M. Prakash, Phys. Rep.**442**, 109 (2007), arXiv:astro-ph/0612440.

[30] M. Shibata and K. Taniguchi, Living Reviews in Relativity **14** (2011).

[31] M. Anderson et al., Physical Review Letters **100**, 191101 (2008), 0801.4387.

[32] É. É. Flanagan and T. Hinderer, Phys. Rev. D**77**, 021502 (2008), 0709.1915.

[33] J. S. Read et al., Phys. Rev. D**79**, 124033 (2009), 0901.3258.

[34] K. Kiuchi, Y. Sekiguchi, M. Shibata, and K. Taniguchi, Phys. Rev. D**80**, 064037 (2009), 0904.4551.

[35] T. A. Apostolatos, C. Cutler, G. J. Sussman, and K. S. Thorne, Phys. Rev. D**49**, 6274 (1994).

[36] A. Vecchio, Phys. Rev. D**70**, 042001 (2004), arXiv:astro-ph/0304051.

[37] R. N. Lang and S. A. Hughes, Phys. Rev. D **74**, 122001 (2006), arXiv:gr-qc/0608062.

[38] M. Shibata, K. Kyutoku, T. Yamamoto, and K. Taniguchi, Phys. Rev. D**79**, 044030 (2009), 0902.0416.

[39] Z. B. Etienne, Y. T. Liu, S. L. Shapiro, and T. W. Baumgarte, Phys. Rev. D**79**, 044024 (2009), 0812.2245.

[40] J. Abadie et al., Classical Quantum Gravity **27**, 173001 (2010), 1003.2480.

[41] N. Andersson et al., General Relativity and Gravitation **43**, 409 (2011), 0912.0384.

[42] É. É. Flanagan and S. A. Hughes, Phys. Rev. D. **57**, 4535 (1998).

[43] R. Oechslin and H.-T. Janka, Physical Review Letters **99**, 121102 (2007), arXiv:astro-ph/0702228.

[44] M. Shibata and K. Taniguchi, Phys. Rev. D. **73**, 064027 (2006), arXiv:astro-ph/0603145.

[45] M. Shibata, Y.-I. Sekiguchi, and R. Takahashi, Progress of Theoretical Physics **118**, 257 (2007), 0709.1766.

[46] S. Chawla et al., Physical Review Letters **105**, 111101 (2010), 1006.2839.

[47] K. Hotokezaka, K. Kyutoku, H. Okawa, M. Shibata, and K. Kiuchi, Phys. Rev. D**83**, 124008 (2011), 1105.4370.

[48] M. Shibata and K. Taniguchi, Phys. Rev. D**77**, 084015 (2008), 0711.1410.

[49] F. Foucart, M. D. Duez, L. E. Kidder, and S. A. Teukolsky, Phys. Rev. D**83**, 024005 (2011), 1007.4203.

[50] Y. Sekiguchi, K. Kiuchi, K. Kyutoku, and M. Shibata, Physical Review Letters **107**, 051102 (2011), 1105.2125.

[51] L. Baiotti, B. Giacomazzo, and L. Rezzolla, Phys. Rev. D**78**, 084033 (2008), 0804.0594.

[52] L. Rezzolla et al., Astrophys. J. Lett.**732**, L6 (2011), 1101.4298.

[53] M. D. Duez, Y. T. Liu, S. L. Shapiro, M. Shibata, and B. C. Stephens, Physical Review Letters **96**, 031101 (2006), arXiv:astro-ph/0510653.

[54] M. Shibata, Y. T. Liu, S. L. Shapiro, and B. C. Stephens, Phys. Rev. D**74**, 104026 (2006), arXiv:astro-ph/0610840.

[55] S. Rosswog, T. Piran, and E. Nakar, ArXiv e-prints (2012), 1204.6240.

[56] M. Shibata, Physical Review Letters **94**, 201101 (2005), arXiv:gr-qc/0504082.

[57] K. Kiuchi, M. Shibata, P. J. Montero, and J. A. Font, Physical Review Letters **106**, 251102 (2011), 1105.5035.

[58] J. C. B. Papaloizou and J. E. Pringle, Phys. Rev. D**208**, 721 (1984).

[59] K. C. B. New, Living Reviews in Relativity **6**, 2 (2003), arXiv:gr-qc/0206041.

[60] C. D. Ott, Class. Quantum Grav. **26**, 063001 (2009), arXiv:0809.0695.

[61] K. Kotake, ArXiv e-prints (2011), 1110.5107.

[62] P. Mészáros, Reports on Progress in Physics, Volume 69, Issue 8, pp. 2259-2321 (2006). **69**, 2259 (2006), arXiv:astro-ph/0605208.

[63] N. Stergioulas, Living Reviews in Relativity **1**, 8 (1998), arXiv:gr-qc/9805012.

[64] C. L. Fryer, D. E. Holz, and S. A. Hughes, Astrophysical Journal **565**, 430 (2002).

[65] N. Andersson, Classical and Quantum Gravity **20**, 105 (2003), arXiv:astro-ph/0211057.

[66] L. Baiotti, R. de Pietri, G. M. Manca, and L. Rezzolla, Phys. Rev. D**75**, 044023 (2007), arXiv:astro-ph/0609473.

[67] J. L. Houser, J. M. Centrella, and S. C. Smith, Physical Review Letters **72**, 1314 (1994), arXiv:gr-qc/9409057.

[68] J. M. Lattimer and M. Prakash, Astrophys. J.**550**, 426 (2001), arXiv:astro-ph/0002232.

[69] M. Y. Fujimoto, Astrophys. J.**419**, 768 (1993).

[70] A. L. Watts, N. Andersson, and D. I. Jones, Astrophys. J. Lett.**618**, L37 (2005), arXiv:astro-ph/0309554.

[71] L. Bildsten, Astrophys. J. Lett.**501**, L89 (1998), arXiv:astro-ph/9804325.

[72] B. Abbott et al., Phys. Rev. D**76**, 082001 (2007), arXiv:gr-qc/0605028.

[73] S. Chandrasekhar, Ellipsoidal figures of equilibriumSilliman Foundati Lect. (Yale Univ. Press, New Haven, CT, 1969).

[74] M. Shibata and Y.-I. Sekiguchi, Phys. Rev. D**71**, 024014 (2005), arXiv:astro-ph/0412243.

[75] C. D. Ott et al., Physical Review Letters **98**, 261101 (2007), arXiv:astro-ph/0609819.

[76] C. D. Ott et al., Classical and Quantum Gravity **24**, 139 (2007), arXiv:astro-ph/0612638.

[77] S. Scheidegger, T. Fischer, S. C. Whitehouse, and M. Liebendörfer, A & A**490**, 231 (2008), 0709.0168.

[78] B. Abbott et al., Physical Review Letters **101**, 211102 (2008), 0808.2050.

[79] L. Lindblom, B. J. Owen, and S. M. Morsink, Physical Review Letters **80**, 4843 (1998), arXiv:gr-qc/9803053.

[80] S. Chandrasekhar, Physical Review Letters **24**, 611 (1970).

[81] J. L. Friedman and B. F. Schutz, Astrophys. J.**222**, 281 (1978).

[82] D. Lai and S. L. Shapiro, Astrophys. J.**442**, 259 (1995), arXiv:astro-ph/9408053.

[83] S. M. Morsink, N. Stergioulas, and S. R. Blattnig, Astrophys. J.**510**, 854 (1999), arXiv:gr-qc/9806008.

[84] M. Shibata and S. Karino, Phys. Rev. D**70**, 084022 (2004), arXiv:astro-ph/0408016.

[85] S. Ou, J. E. Tohline, and L. Lindblom, Astrophys. J.**617**, 490 (2004), arXiv:astro-ph/0406037.

[86] B. Zink, O. Korobkin, E. Schnetter, and N. Stergioulas, Phys. Rev. D**81**, 084055 (2010), 1003.0779.

[87] B. J. Owen and L. Lindblom, Classical and Quantum Gravity **19**, 1247 (2002), arXiv:gr-qc/0111024.

[88] R. Bondarescu, S. A. Teukolsky, and I. Wasserman, Phys. Rev. D**79**, 104003 (2009), 0809.3448.

[89] B. J. Owen, Physical Review Letters **95**, 211101 (2005), arXiv:astro-ph/0503399.

[90] N. Andersson, K. D. Kokkotas, and N. Stergioulas, Astrophys. J.**516**, 307 (1999), arXiv:astro-ph/9806089.

[91] S. E. Woosley, Astrophys. J.**405**, 273 (1993).

[92] S. Woosley and T. Janka, Nature Physics, Volume 1, Issue 3, pp. 147-154 (2005). **1**, 147 (2005), arXiv:astro-ph/0601261.

[93] C. Curry and R. E. Pudritz, Phys. Rev. D**281**, 119 (1996).

[94] O. Korobkin, E. B. Abdikamalov, E. Schnetter, N. Stergioulas, and B. Zink, Phys. Rev. D**83**, 043007 (2011), 1011.3010.

[95] W. Fu and D. Lai, Phys. Rev. D**410**, 1617 (2011), 1006.3824.

[96] J. W. Woodward, J. E. Tohline, and I. Hachisu, Astrophys. J.**420**, 247 (1994).

[97] A. L. Piro and E. Pfahl, Astrophys. J. **658**, 1173 (2007).

[98] M. D. Duez, S. L. Shapiro, and H.-J. Yo, Phys. Rev. D**69**, 104016 (2004), arXiv:gr-qc/0401076.

[99] C. F. Gammie, Astrophys. J.**553**, 174 (2001), arXiv:astro-ph/0101501.

[100] S. Kobayashi and P. Mészáros, Astrophys. Journal **589**, 861 (2003), arXiv:astro-ph/0210211.

[101] M. H. P. M. van Putten and E. C. Ostriker, Astrophys. J. Lett.**552**, L31 (2001), arXiv:astro-ph/0010440.

[102] M. H. P. M. van Putten and A. Levinson, Astrophys. J.**584**, 937 (2003), arXiv:astro-ph/0212297.

[103] I. A. Bonnell and J. E. Pringle, Phys. Rev. D**273**, L12 (1995).

[104] M. B. Davies, A. King, S. Rosswog, and G. Wynn, Astrophysical Journal **579**, L63 (2002), arXiv:astro-ph/0204358.

[105] B. Zink et al., Physical Review Letters **96**, 161101 (2006), arXiv:gr-qc/0501080.

[106] B. Zink et al., Phys. Rev. D**76**, 024019 (2007), arXiv:astro-ph/0611601.

[107] G. Rockefeller, C. L. Fryer, and H. Li, ArXiv Astrophysics e-prints (2006), arXiv:astro-ph/0608028.

[108] R. C. Duncan and C. Thompson, Astrophys. J. Lett.**392**, L9 (1992).

[109] C. Thompson and R. C. Duncan, Phys. Rev. D**275**, 255 (1995).

[110] C. Thompson and R. C. Duncan, Astrophys. J.**473**, 322 (1996).

[111] C. Kouveliotou et al., Astrophys. J. Lett.**510**, L115 (1999), arXiv:astro-ph/9809140.

[112] A. Corsi and B. J. Owen, Phys. Rev. D**83**, 104014 (2011), 1102.3421.

[113] N. Gehrels, E. Ramirez-Ruiz, and D. B. Fox, Annu. Rev. Astron. Astrophys.**47**, 567 (2009), 0909.1531.

[114] D. M. Palmer et al., Nature**434**, 1107 (2005), arXiv:astro-ph/0503030.

[115] The LIGO Scientific Collaboration, Astrophysical Journal **681**, 1419 (2008).

[116] E. O. Ofek et al., Astrophysical Journal **681**, 1464 (2008), arXiv:0712.3585.

[117] The LIGO Scientific Collaboration, Phys. Rev. D **76**, 062003 (2007), arXiv:astro-ph/0703419.

[118] J. Abadie et al., Astrophys. J. Lett.**734**, L35+ (2011), 1011.4079.

[119] B. Cheng, R. I. Epstein, R. A. Guyer, and A. C. Young, Nature**382**, 518 (1996).

[120] C. Barat et al., A & A**126**, 400 (1983).

[121] T. E. Strohmayer and A. L. Watts, Astrophys. J. Lett.**632**, L111 (2005), arXiv:astro-ph/0508206.

[122] T. E. Strohmayer and A. L. Watts, Astrophys. J.**653**, 593 (2006), arXiv:astro-ph/0608463.

[123] A. L. Watts and T. E. Strohmayer, Astrophys. J. Lett.**637**, L117 (2006), arXiv:astro-ph/0512630.

[124] G. L. Israel et al., Astrophys. J. Lett.**628**, L53 (2005), arXiv:astro-ph/0505255.

[125] Y. Levin, Phys. Rev. D**368**, L35 (2006), arXiv:astro-ph/0601020.

[126] M. van Hoven and Y. Levin, Phys. Rev. D**410**, 1036 (2011), 1006.0348.

[127] N. Andersson and K. D. Kokkotas, Phys. Rev. D**299**, 1059 (1998), arXiv:gr-qc/9711088.

[128] K. D. Kokkotas, T. A. Apostolatos, and N. Andersson, Phys. Rev. D**320**, 307 (2001), arXiv:gr-qc/9901072.

[129] K. Ioka, MNRAS **327**, 639 (2001), arXiv:astro-ph/0009327.

[130] B. P. Abbott et al., Astrophys. J. Lett.**701**, L68 (2009), 0905.0005.

[131] J. E. Horvath, Modern Physics Letters A **20**, 2799 (2005), arXiv:astro-ph/0508223.

[132] E. Berger et al., Astrophys. J.**664**, 1000 (2007), arXiv:astro-ph/0611128.

[133] S. Nissanke, D. E. Holz, S. A. Hughes, N. Dalal, and J. L. Sievers, Astrophys. J.**725**, 496 (2010), 0904.1017.

[134] S. Kobayashi and P. Mészáros, ApJ Lett. **585**, L89 (2003).

[135] J. G. Baker, J. Centrella, D.-I. Choi, M. Koppitz, and J. van Meter, Phys. Rev. D**73**, 104002 (2006), arXiv:gr-qc/0602026.

[136] D. J. Nice et al., Astrophys. J.**634**, 1242 (2005), arXiv:astro-ph/0508050.

[137] C. Cutler and É. E. Flanagan, Phys. Rev. D**49**, 2658 (1994), arXiv:gr-qc/9402014.

[138] M. Vallisneri, Physical Review Letters **84**, 3519 (2000), arXiv:gr-qc/9912026.

[139] J. M. Lattimer and M. Prakash, Phys. Rep.**442**, 109 (2007), arXiv:astro-ph/0612440.

[140] B. D. Lackey, K. Kyutoku, M. Shibata, P. R. Brady, and J. L. Friedman, Phys. Rev. D**85**, 044061 (2012), 1109.3402.

[141] J. A. Faber, P. Grandclément, F. A. Rasio, and K. Taniguchi, Physical Review Letters **89**, 231102 (2002), arXiv:astro-ph/0204397.

[142] N. Andersson, D. I. Jones, and K. D. Kokkotas, Phys. Rev. D**337**, 1224 (2002), arXiv:astro-ph/0111582.

[143] R. Oechslin, K. Uryū, G. Poghosyan, and F. K. Thielemann, Phys. Rev. D**349**, 1469 (2004), arXiv:astro-ph/0401083.

[144] F. Limousin, D. Gondek-Rosińska, and E. Gourgoulhon, Phys. Rev. D**71**, 064012 (2005), arXiv:gr-qc/0411127.

[145] D. J. Price and S. Rosswog, Science **312**, 719 (2006), arXiv:astro-ph/0603845.

[146] H. Sotani, K. Nakazato, K. Iida, and K. Oyamatsu, Physical Review Letters, vol. 108, Issue 20, id. 201101 **108**, 201101 (2012), 1202.6242.

[147] J. Weber, Physical Review **117**, 306 (1960).

[148] J. Weber, Physical Review Letters **22**, 1320 (1969).

[149] J. Weber, Physical Review Letters **25**, 180 (1970).

[150] A. Morse, W. O. Hamilton, W. W. Johnson, E. Mauceli, and M. P. McHugh, Phys. Rev. D **59**, 062002 (1999).

[151] R. Weiss, LIGO P720002 (1972).

[152] A. Abramovici et al., Science **256**, 325 (1992).

[153] B. C. Barish and R. Weiss, Physics Today **52**, 44 (1999).

[154] B. P. Abbott et al., Rep. Prog. Phys. **72**, 076901 (2009).

[155] G. M. Harry and the LIGO Scientific Collaboration, Classical Quantum Gravity **27**, 084006 (2010).

[156] M. A. A., Am. J. Sci. **34**, 333 (1887).

[157] P. R. Saulson, Fundamentals of interferometric gravitational wave detectors (World Scientific Publishers, 1994, xvi, 299 p. ISBN 9810218206, 1994).

[158] D. Sigg, Gravitational waves, LIGO-P980007, 1998.

[159] R. Adhikari, Dissertation (2004).

[160] R. Abbott et al., Classical Quantum Gravity **19**, 1591 (2002).

[161] K. Kuroda et al., International Journal of Modern Physics D **8**, 557 (1999).

[162] M. Punturo et al., Classical Quantum Gravity **27**, 194002 (2010).

[163] T. Uchiyama et al., Classical and Quantum Gravity **21**, 1161 (2004).

[164] Y. Aso, Dissertation (2006).

[165] B. Willke et al., Classical Quantum Gravity **19**, 1377 (2002).

[166] S. A. Hughes and K. S. Thorne, Phys. Rev. D **58**, 122002 (1998), arXiv:gr-qc/9806018.

[167] J. Harms, R. Desalvo, S. Dorsher, and V. Mandic, Phys. Rev. D **80**, 122001 (2009), 0909.3341.

[168] K. Yamamoto et al., Phys. Rev. D **78**, 022004 (2008), 0805.2387.

[169] B. Iyer et al., Ligo-india, proposal of the consortium for indian initiative in gravitational-wave observations (indigo), 2011.

[170] G. M. Harry and the LIGO Scientific Collaboration, Classical Quantum Gravity **27**, 084006 (2010).

[171] D. Shoemaker, LIGO Document (2010), LIGO-T0900288.

[172] the LIGO Scientific Collaboration et al., ArXiv e-prints (2012), 1202.2788.

[173] P. Fritschel, Second generation instruments for the Laser Interferometer Gravitational Wave Observatory (LIGO), in Society of Photo-Optical Instrumentation Engineers (SPIE) Conference Series, edited by M. Cruise and P. Saulson, , Society of Photo-Optical Instrumentation Engineers (SPIE) Conference Series Vol. 4856, pp. 282–291, 2003, arXiv:gr-qc/0308090.

[174] A. M. Beloborodov, Phys. Rev. D**407**, 1033 (2010), 0907.0732.

[175] A. Levinson, International Journal of Modern Physics A **21**, 6015 (2006), arXiv:astro-ph/0611521.

[176] B. Zhang, Comptes Rendus Physique **12**, 206 (2011), 1104.0932.

[177] P. Mészáros and E. Waxman, Physical Review Letters **87**, 171102 (2001), arXiv:astro-ph/0103275.

[178] S. Horiuchi and S. Ando, Phys. Rev. D **77**, 063007 (2008).

[179] S. Razzaque, P. Mészáros, and E. Waxman, Phys. Rev. Lett. **93**, 181101 (2004).

[180] E. Waxman and J. Bahcall, Physical Review Letters **78**, 2292 (1997).

[181] K. Murase, T. A. Thompson, B. C. Lacki, and J. F. Beacom, Phys.Rev. **D84**, 043003 (2011), 1012.2834.

[182] J. Arons, Astrophys.J. **589**, 871 (2003), astro-ph/0208444.

[183] N. Bucciantini, E. Quataert, J. Arons, B. Metzger, and T. A. Thompson, (2007), 0707.2100.

[184] K. Murase, P. Meszaros, and B. Zhang, Phys.Rev. **D79**, 103001 (2009), 0904.2509.

[185] S. Razzaque, P. Mészáros, and E. Waxman, Phys. Rev. D **68**, 083001 (2003).

[186] S. Razzaque and A. Y. Smirnov, ArXiv (2009), 0912.4028.

[187] G. C. Hill, Astropart. Phys. **6**, 215 (1997).

[188] J. A. Castro Pena, G. Parente, and E. Zas, Phys. Lett. B **507**, 231 (2001), arXiv:hep-ph/0011309.

[189] J. F. Beacom, N. F. Bell, D. Hooper, S. Pakvasa, and T. J. Weiler, Phys. Rev. D **68**, 093005 (2003).

[190] W. Winter, ArXiv e-prints (2012), 1201.5462.

[191] J. Braun et al., Astropart. Phys **29**, 299 (2008), 0801.1604.

[192] J. Ahrens et al., Astroparticle Physics **20**, 507 (2004), arXiv:astro-ph/0305196.

[193] P. Coyle, ArXiv (2010), 1002.0754.

[194] A. Avrorin et al., Nucl. Instrum. Methods Phys. Res., Sect. A **626-627**, S13 (2011).

[195] M. de Jong, Nucl. Instrum. Methods Phys. Res., Sect. A **623**, 445 (2010).

[196] R. Abbasi et al., Nature**484**, 351 (2012), 1204.4219.

[197] J. Ahrens and et al., Nucl. Instrum. Methods Phys. Res., Sect. A **524**, 169 (2004).

[198] A. Romeyer and et al., Muon Energy Reconstruction in ANTARES and Its Application to the Diffuse Neutrino Flux, in International Cosmic Ray Conference, , International Cosmic Ray Conference Vol. 3, pp. 1329–+, 2003, arXiv:hep-ex/0308074.

[199] R. Abbasi et al. (IceCube Collaboration), Phys. Rev. D **83**, 012001 (2011).

[200] A. Achterberg et al., Astroparticle Physics **26**, 155 (2006).

[201] S. R. Klein, IEEE Transactions on Nuclear Science **56**, 1141 (2009), 0807.0034.

[202] E. Waxman and J. N. Bahcall, Astrophys. Journal **541**, 707 (2000), arXiv:hep-ph/9909286.

[203] D. Guetta and J. Granot, Phys. Rev. Lett. **90**, 201103 (2003), arXiv:astro-ph/0212045.

[204] S. Razzaque, P. Mészáros, and E. Waxman, Physical Review Letters **90**, 241103 (2003), arXiv:astro-ph/0212536.

[205] C. D. Dermer and A. Atoyan, Phys. Rev. Lett. **91**, 071102 (2003), arXiv:astro-ph/0301030.

[206] K. Murase and S. Nagataki, Phys. Rev. Lett. **97**, 051101 (2006), arXiv:astro-ph/0604437.

[207] K. Murase, K. Ioka, S. Nagataki, and T. Nakamura, Astrophys. J. Lett. **651**, L5 (2006).

[208] K. Ioka, MNRAS **327**, 639 (2001).

[209] K. Ioka, S. Razzaque, S. Kobayashi, and P. Mészáros, Astrophys. J. **633**, 1013 (2005), arXiv:astro-ph/0503279.

[210] A. Achterberg et al., Physical Review Letters **97**, 221101 (2006), arXiv:astro-ph/0607233.

[211] E. Chassande-Mottin, M. Hendry, P. J. Sutton, and S. Márka, Gen. Relat. Gravit. **43**, 437 (2011).

[212] V. van Elewyck et al., Int. J. Mod. Phys. D **18**, 1655 (2009), 0906.4957.

[213] I. Bartos, B. Dasgupta, and S. Marka, ArXiv e-prints (2012), 1206.0764.

[214] T. J. Galama et al., Nature**395**, 670 (1998), arXiv:astro-ph/9806175.

[215] S. R. Kulkarni et al., Nature**395**, 663 (1998).

[216] D. Malesani et al., Astrophys. J. Lett. **609**, L5 (2004), arXiv:astro-ph/0405449.

[217] A. M. Soderberg et al., Nature **430**, 648 (2004), arXiv:astro-ph/0408096.

[218] B. E. Cobb, C. D. Bailyn, P. G. van Dokkum, and P. Natarajan, Astrophys. J. Lett. **645**, L113 (2006), arXiv:astro-ph/0603832.

[219] E. Pian et al., Nature**442**, 1011 (2006), arXiv:astro-ph/0603530.

[220] A. M. Soderberg et al., Nature**442**, 1014 (2006), arXiv:astro-ph/0604389.

[221] D. M. Coward, Phys. Rev. D**360**, L77 (2005), arXiv:astro-ph/0504493.

[222] O. Bromberg, E. Nakar, and T. Piran, ArXiv e-prints (2011), 1107.1346.

[223] N. Gupta and B. Zhang, Astroparticle Physics **27**, 386 (2007), arXiv:astro-ph/0606744.

[224] X.-Y. Wang, S. Razzaque, P. Mészáros, and Z.-G. Dai, Phys. Rev. D **76**, 083009 (2007), 0705.0027.

[225] W. Li et al., MNRAS **412**, 1473 (2011).

[226] A. M. Soderberg et al., Nature **463**, 513 (2010).

[227] E. Liang, B. Zhang, F. Virgili, and Z. G. Dai, Astrophys. J. **662**, 1111 (2007).

[228] E. Howell, T. Regimbau, A. Corsi, D. Coward, and R. Burman, MNRAS **410**, 2123 (2011), 1008.3941.

[229] F. Acernese et al., Classical Quantum Gravity **23**, S635 (2006).

[230] J. Abadie et al., Phys. Rev. D**81**, 102001 (2010), 1002.1036.

[231] J. Abadie et al., Phys. Rev. D**82**, 102001 (2010), 1005.4655.

[232] B. Abbott et al., Astrophys. J.**681**, 1419 (2008), 0711.1163.

[233] B. P. Abbott et al., Astrophys. J.**715**, 1438 (2010), 0908.3824.

[234] J. Abadie et al., Astrophys. J.**715**, 1453 (2010), 1001.0165.

[235] J. Piscionere et al., LOOC UP: Locating and Observing Optical Counterparts to Unmodeled Pulses in Gravitational Waves, in American Astronomical Society Meeting Abstracts, , Bulletin of the American Astronomical Society Vol. 38, pp. 910–+, 2007.

[236] J. Kanner et al., Classical Quantum Gravity **25**, 184034 (2008), 0803.0312.

[237] P. S. Shawhan, LIGO Scientific Collaboration, and Virgo Collaboration, LOOC-UP: Seeking Optical Counterparts to Gravitational-Wave Signal Candidates, in American Astronomical Society Meeting Abstracts #215, , Bulletin of the American Astronomical Society Vol. 42, pp. 406.06–+, 2010.

[238] B. Baret et al., Astropart. Phys. **35**, 1 (2011).

[239] the LIGO Scientific Collaboration et al., ArXiv e-prints (2011), 1111.7314.

[240] The LIGO Scientific Collaboration, Reports on Progress in Physics **72**, 076901 (2009).

[241] B. Abbott et al., Astrophys. J. **681**, 1419 (2008), 0711.1163.

[242] E. P. Mazets et al., Astrophys. J. **680**, 545 (2008), 0712.1502.

[243] The LIGO Scientific Collaboration et al., ArXiv e-prints (2012), 1201.4413.

[244] B. Abbott et al., Phys. Rev. D**72**, 042002 (2005), arXiv:gr-qc/0501068.

[245] M. S. Briggs et al., ArXiv e-prints (2012), 1205.2216.

[246] C. Meegan et al., Astrophys. J.**702**, 791 (2009), 0908.0450.

[247] J. Kanner et al., Classical and Quantum Gravity **25**, 184034 (2008).

[248] The LIGO Scientific Collaboration et al., ArXiv e-prints (2011), 1109.3498.

[249] P. A. Evans et al., ArXiv e-prints (2012), 1205.1124.

[250] D. J. White, E. J. Daw, and V. S. Dhillon, CQG **28**, 085016 (2011).

[251] P. Shawan, AMON Workshop (2011).

[252] Astrophysical Multimessenger Observatory Network (AMON), http://amon.gravity.psu.edu/.

[253] S. Basa et al., ArXiv e-prints (2012), 1201.6383.

[254] E. Nakar, Physics Reports **442**, 166 (2007), arXiv:astro-ph/0701748.

[255] N. Gehrels et al., Astrophysical Journal **611**, 1005 (2004), arXiv:astro-ph/0405233.

[256] N. M. Law et al., Publ. Astron. Soc. Pac. **121**, 1395 (2009), 0906.5350.

[257] L.-X. Li and B. Paczyński, Astrophys. J. **507**, L59 (1998), arXiv:astro-ph/9807272.

[258] S. Rosswog, Astrophys. J.**634**, 1202 (2005), arXiv:astro-ph/0508138.

[259] B. D. Metzger et al., Electromagnetic Counterparts of Compact Object Mergers Powered by the Radioactive Decay of R-process Nuclei, 2010, arXiv:1001.5029.

[260] L. F. Roberts, D. Kasen, W. H. Lee, and E. Ramirez-Ruiz, Astrophys. J. Lett.**736**, L21 (2011), 1104.5504.

[261] S. Goriely, A. Bauswein, and H.-T. Janka, Astrophys. J. Lett.**738**, L32 (2011), 1107.0899.

[262] S. R. Kulkarni, ArXiv Astrophysics e-prints (2005), arXiv:astro-ph/0510256.

[263] E. Nakar and T. Piran, Nature**478**, 82 (2011).

[264] K. Toma, K. Ioka, T. Sakamoto, and T. Nakamura, Astrophys. J.**659**, 1420 (2007), arXiv:astro-ph/0610867.

[265] P. A. Mazzali et al., Nature**442**, 1018 (2006), arXiv:astro-ph/0603567.

[266] A. Corsi and P. Mészáros, Astrophys. J.**702**, 1171 (2009), 0907.2290.

[267] W.-X. Chen and A. M. Beloborodov, The Astrophysical Journal **657**, 383 (2007).

[268] L. Dessart, C. D. Ott, A. Burrows, S. Rosswog, and E. Livne, The Astrophysical Journal **690**, 1681 (2009).

[269] K. P et al., LIGO Internal Document (LIGO-P1000062) (2010).

[270] K. Hirata et al., Phys. Rev. Lett. **58**, 1490 (1987).

[271] R. M. Bionta et al., Phys. Rev. Lett. **58**, 1494 (1987).

[272] B. Baret et al., Phys. Rev. D**85**, 103004 (2012), 1112.1140.

[273] H.-T. Janka, K. Langanke, A. Marek, G. Martínez-Pinedo, and B. Müller, Phys. Rep. **442**, 38 (2007), arXiv:astro-ph/0612072.

[274] T. Fischer, S. C. Whitehouse, A. Mezzacappa, F.-K. Thielemann, and M. Liebendörfer, Astronomy & Astrophysics **517**, A80 (2010).

[275] L. Hüdepohl, B. Müller, H.-T. Janka, A. Marek, and G. G. Raffelt, Phys. Rev. Lett. **104**, 251101 (2010).

[276] IceCube Collaboration et al., ArXiv e-prints (2011), 1108.0171.

[277] J. W. Murphy, C. D. Ott, and A. Burrows, The Astrophysical Journal **707**, 1173 (2009).

[278] A. Marek, H.-T. Janka, and E. Müller, A & A**496**, 475 (2009), 0808.4136.

[279] C. D. Ott, A. Burrows, L. Dessart, and E. Livne, The Astrophysical Journal **685**, 1069 (2008).

[280] I. Sagert et al., Phys. Rev. Lett. **102**, 081101 (2009).

[281] E. B. Abdikamalov, H. Dimmelmeier, L. Rezzolla, and J. C. Miller, Monthly Notices of the Royal Astronomical Society **392**, 52 (2009).

[282] Y. Sekiguchi and M. Shibata, Progress of Theoretical Physics **117**, 1029 (2007), 0706.4154.

[283] J. Hjorth and J. S. Bloom, To appear as Chapter 9 in "Gamma-Ray Bursts", eds. C. Kouveliotou, R. A. M. J. Wijers, S. E. Woosley, Cambridge University Press, 2011; arXiv:1104.2274 (2011).

[284] S. E. Woosley and J. S. Bloom, Annu. Rev. Astron. Astrophys.**44**, 507 (2006), arXiv:astro-ph/0609142.

[285] M. Modjaz, Ast. Nachr. **332**, 434 (2011).

[286] The Super-KAMIOKANDE Collaboration et al., Nuclear Instruments and Methods in Physics Research A **501**, 418 (2003).

[287] KamLAND, http://www.awa.tohoku.ac.jp/kamlande/.

[288] M. Aglietta et al., 13th International Conference on Particles and Nuclei, Perugia, Italy, 28 Jun - 2 Jul 1993, pp.743-746 (1994).

[289] G. Alimonti et al., Astroparticle Physics **16**, 205 (2002).

[290] R. V. Novoseltseva et al., ArXiv e-prints (2009), 0910.0738.

[291] J. Ahrens et al., Astroparticle Physics **20**, 507 (2004).

[292] P. Antonioli et al., New Journal of Physics **6**, 114 (2004), arXiv:astro-ph/0406214.

[293] F. Halzen and G. G. Raffelt, Phys. Rev. D**80**, 087301 (2009), 0908.2317.

[294] J. Maricic and the Lbne Dusel collaboration, Journal of Physics Conference Series **203**, 012109 (2010).

[295] K. Nakamura, Hyper-Kamiokande - a Next Generation Water Cherenkov Detector, in Neutrinos and Implications for Physics Beyond the Standard Model, edited by R. Shrock, p. 307, 2003.

[296] S. Ando, J. F. Beacom, and H. Yüksel, Physical Review Letters **95**, 171101 (2005), arXiv:astro-ph/0503321.

[297] I. Leonor et al., Classical and Quantum Gravity **27**, 084019 (2010), 1002.1511.

[298] P. Mészáros, S. Kobayashi, S. Razzaque, and B. Zhang, High Energy Photons, Neutrinos and Gravitational Waves from Gamma-Ray Bursts, in Beaming and Jets in Gamma Ray Bursts, edited by R. Ouyed, p. 30, 2002.

[299] S. Razzaque, P. Mészáros, and E. Waxman, Phys. Rev. D **68**, 083001 (2003), arXiv:astro-ph/0303505.

[300] S. Ando and J. F. Beacom, Physical Review Letters **95**, 061103 (2005), arXiv:astro-ph/0502521.

[301] S. Razzaque, P. Mészáros, and E. Waxman, Mod. Phys. Lett. A **20**, 2351 (2005), arXiv:astro-ph/0509729.

[302] B. Zhang, Z. G. Dai, P. Mészáros, E. Waxman, and A. K. Harding, Astrophys. Journal **595**, 346 (2003), arXiv:astro-ph/0210382.

[303] B. Zhang, Z. G. Dai, P. Mészáros, E. Waxman, and A. K. Harding, Astrophys. J. **595**, 346 (2003).

[304] S. Hümmer, P. Baerwald, and W. Winter, Phys. Rev. Lett. **108**, 231101 (2012).

[305] H.-N. He et al., Astrophys. J.**752**, 29 (2012), 1204.0857.

[306] J. S. Bloom, S. R. Kulkarni, and S. G. Djorgovski, Astron. J.**123**, 1111 (2002), arXiv:astro-ph/0010176.

[307] J. Sollerman et al., New Astronomy **11**, 103 (2005), arXiv:astro-ph/0506686.

[308] A. S. Fruchter et al., Nature**441**, 463 (2006), arXiv:astro-ph/0603537.

[309] S. Savaglio, K. Glazebrook, and D. Le Borgne, Astrophys. J.**691**, 182 (2009), 0803.2718.

[310] E. Berger, Astrophys. J.**690**, 231 (2009), 0805.0306.

[311] W. Fong, E. Berger, and D. B. Fox, Astrophys. J.**708**, 9 (2010), 0909.1804.

[312] S. F. Portegies Zwart and L. R. Yungelson, Astronomy and Astrophysics **332**, 173 (1998).

[313] C. Fryer, A. Burrows, and W. Benz, Astrophysical Journal **496**, 333 (1998).

[314] L. Z. Kelley, E. Ramirez-Ruiz, M. Zemp, J. Diemand, and I. Mandel, Astrophys. J. Lett.**725**, L91 (2010), 1011.1256.

[315] E. Berger, Astrophys. J.**722**, 1946 (2010), 1007.0003.

[316] K. Hurley, Advances in Space Research **47**, 1326 (2011).

[317] I. Bartos et al., Classical and Quantum Gravity **27**, 084025 (2010).

[318] I. Bartos et al., Technical Note LIGO-E090003 (2009), https://dcc.ligo.org/cgi-bin/private/DocDB/ShowDocument?docid=483.

[319] I. Bartos et al., Technical Note LIGO-E080541 (2008), https://dcc.ligo.org/cgi-bin/private/DocDB/ShowDocument?docid=485.

[320] M. Factourovich, Technical Note LIGO-T070218 (2007), http://www.ligo.caltech.edu/docs/T/T070218-00/T070218-00.pdf.

[321] I. Bartos and D. Sigg, Technical Note LIGO-E0900036 (2009), https://dcc.ligo.org/cgi-bin/private/DocDB/ShowDocument?docid=604.

[322] I. Bartos et al., Drawing and Components Information LIGO-D070011-B (2008), http://www.ligo.caltech.edu/docs/D/D070011-B/.

[323] I. Bartos et al., Drawing and Components Information LIGO-D080094-D (2008), http://www.ligo.caltech.edu/docs/D/D080094-D/.

[324] I. Bartos et al., Drawing LIGO-D080534 (2008), https://dcc.ligo.org/cgi-bin/private/DocDB/ShowDocument?docid=491.

[325] I. Bartos et al., Drawing and Components Information LIGO-D070071-B (2008), http://www.ligo.caltech.edu/docs/D/D070071-B/.

[326] I. Bartos et al., Engineering Document LIGO-E090002 (2008), https://dcc.ligo.org/cgi-bin/DocDB/ShowDocument?docid=492.

[327] I. Bartos et al., Engineering Document LIGO-E0900016 (2009), https://dcc.ligo.org/cgi-bin/DocDB/ShowDocument?docid=484.

[328] I. Bartos et al., Technical Note LIGO-T080083 (2009), https://dcc.ligo.org/cgi-bin/DocDB/ShowDocument?docid=490.

[329] I. Bartos et al., Engineering Document LIGO-E050262 (2008), https://dcc.ligo.org/cgi-bin/DocDB/ShowDocument?docid=486.

[330] I. Bartos et al., Engineering Document LIGO-E0900019 (2008), https://dcc.ligo.org/cgi-bin/DocDB/ShowDocument?docid=488.

[331] I. Bartos et al., Engineering Document LIGO-E90001 (2009), https://dcc.ligo.org/cgi-bin/DocDB/ShowDocument?docid=493.

[332] S. Fairhurst, New J. Phys. **11**, 123006 (2009).

[333] Y. Aso et al., Classical Quantum Gravity **25**, 114039 (2008).

[334] S. Klimenko et al., Phys. Rev. D **83**, 102001 (2011), 1101.5408.

[335] P. Fritschel, arXiv:gr-qc/0308090v1 **4856**, 282 (2003).

[336] D. Sigg, Technical Note LIGO-T970101-B-D (2003), http://www.ligo.caltech.edu/docs/T/T970101-B.pdf.

[337] F. Cavalier et al., Physical Review D (Particles, Fields, Gravitation, and Cosmology) **74**, 082004 (2006).

[338]

[339] S. Marka, Notes on s5 timing, LIGO-G080510, 2008.

[340] R. Abbasi et al., Astrophys. J. **710**, 346 (2010), 0907.2227.

[341] The IceCube Collaboration, Astrophys. J. **701**, 1721 (2009).

[342] IceCube Collaboration, R. Abbasi et al., Phys. Rev. Lett. **106**, 141101 (2011).

[343] B. Abbott and et al. (LIGO Scientific Collaboration), Phys. Rev. D **72**, 042002 (2005).

[344] B. Abbott et al., Phys. Rev. D **77**, 062004 (2008), 0709.0766.

[345] B. P. Abbott et al., Astrophys. J. **715**, 1438 (2010).

[346] P. Mészáros, Rep. Prog. Phys. **69**, 2259 (2006).

[347] LIGO Scientific Collaboration and Virgo Collaboration, Astrophys. J. **715**, 1453 (2010).

[348] W. B. Atwood and et al., Astrophys. J. **697**, 1071 (2009).

[349] P. Mészáros and et al., GRB 2010 Kyoto Conf. Proc. (2010).

[350] N. Omodei and for the Fermi LAT and Fermi GBM collaborations, ArXiv (2009), 0907.0715.

[351] B. L. Dingus, Astrophys. Space Sci. **231**, 187 (1995), 10.1007/BF00658613.

[352] G. J. Fishman and C. A. Meegan, Annu. Rev. Astron. Astrophys. **33**, 415 (1995).

[353] M. Sommer and et al., Astrophys. J. Lett. **422**, L63 (1994).

[354] A. A. Abdo and et al., Astrophys. J. Suppl. Ser. **188**, 405 (2010), 1002.2280.

[355] G. Ghisellini and et al., MNRAS **403**, 926 (2010), 0910.2459.

[356] Ghirlanda, G., Ghisellini, G., and Nava, L., A&A **510**, L7 (2010).

[357] M. D. Pasquale and et al., Astrophys. J. Lett. **709**, L146 (2010).

[358] A. Corsi, D. Guetta, and L. Piro, Astrophys. J. **720**, 1008 (2010).

[359] H. He and et al., ArXiv (2010), 1009.1432.

[360] K. Toma, X. Wu, and P. Mészáros, ArXiv (2010), 1002.2634.

[361] J. K. Becker and et al., Astrophys. J. **721**, 1891 (2010).

[362] K. Asano, S. Inoue, and P. Mészáros, Astrophys. J. **699**, 953 (2009).

[363] The Fermi LAT and Fermi GBM Collaborations, Science **323**, 1688 (2009), http://www.sciencemag.org/cgi/reprint/323/5922/1688.pdf.

[364] A. A. Abdo and et al., Astrophys. J. Lett. **706**, L138 (2009).

[365] C. D. Ott, Classical Quantum Gravity **26**, 063001 (48pp) (2009).

[366] E. O'Connor and C. D. Ott, ArXiv (2010), 1010.5550.

[367] R. Perna and et al., Astrophys. J. Lett. **636**, L29 (2006).

[368] C. L. Fryer, D. E. Holz, and S. A. Hughes, Astrophys. J.**565**, 430 (2002).

[369] M. B. Davies, A. King, S. Rosswog, and G. Wynn, Astrophys. J. Lett. **579**, L63 (2002).

[370] A. King et al., Astrophys. J. Lett. **630**, L113 (2005), arXiv:astro-ph/0508126.

[371] M. H. P. M. van Putten and A. Levinson, Science **295**, 1874 (2002), http://www.sciencemag.org/cgi/reprint/295/5561/1874.pdf.

[372] S. Kobayashi and P. Mészáros, Astrophys. J.**589**, 861 (2003).

[373] D. Guetta and L. Stella, A&A **498**, 329 (2009), 0811.0684.

[374] M. A. Scheel and et al., Phys. Rev. D **79**, 024003 (2009).

[375] C. Hopman and et al., Astrophys. J. Lett.**643**, L91 (2006).

[376] D. Guetta, M. Spada, and E. Waxman, Astrophys. J. **559**, 101 (2001).

[377] K. Murase and S. Nagataki, Phys. Rev. D **73**, 063002 (2006), arXiv:astro-ph/0512275.

[378] W. Zhang and A. MacFadyen, Astrophys. J. **698**, 1261 (2009).

[379] B. J. Morsony, D. Lazzati, and M. C. Begelman, Astrophys. J. **723**, 267 (2010).

[380] E. Waxman, Nucl. Phys. B-Proc Sup. **118**, 353 (2003), arXiv:astro-ph/0211358.

[381] S. Razzaque, P. Mészáros, and E. Waxman, Phys. Rev. Lett. **93**, 181101 (2004), Erratum: Phys. Rev. Lett. 94, 109903 (2005).

[382] M. Vietri, Nucl. Phys. B Proc. Suppl. **69**, 694 (1999).

[383] K. Murase, Phys. Rev. D **76**, 123001 (2007), 0707.1140.

[384] D. Lazzati, Mon. Not. R. Astron. Soc. **357**, 722 (2005), arXiv:astro-ph/0411753.

[385] D. Burlon and et al., Astrophys. J. Lett. **685**, L19 (2008).

[386] E. Troja, S. Rosswog, and N. Gehrels, ArXiv (2010), 1009.1385.

[387] X.-Y. Wang and P. Mészáros, Astrophys. J. **670**, 1247 (2007).

[388] D. Lazzati and M. C. Begelman, Astrophys. J. **629**, 903 (2005).

[389] L. Li, Monthly Notices of the Royal Astronomical Society **380**, 621 (2007), arXiv:astro-ph/0703144.

[390] U. Jacob and T. Piran, Nature Phys. **3**, 87 (2007), arXiv:hep-ph/0607145.

[391] E. Cappellaro et al., A&A **273**, 383 (1993).

[392] M. R. Blanton et al., Astrophys. J. **592**, 819 (2003).

[393] R. Abbasi et al., Astrophys. J. **732**, 18 (2011), 1012.2137.

[394] R. Abbasi et al., ArXiv[1106.3484] (2011).

[395] M. H. P. M. van Putten et al., Phys. Rev. D **69**, 044007 (2004).

[396] S. E. Woosley, Astrophys. J.**405**, 273 (1993).

[397] B. Paczynski, Astrophys.J. **494**, L45 (1998), astro-ph/9710086.

[398] A. I. MacFadyen, S. E. Woosley, and A. Heger, Astrophys. J.**550**, 410 (2001).

[399] B. D. Metzger, D. Giannios, T. A. Thompson, N. Bucciantini, and E. Quataert, Phys. Rev. D**413**, 2031 (2011).

[400] C. D. Matzner, Phys. Rev. D**345**, 575 (2003).

[401] S. E. Woosley and J. S. Bloom, Annu. Rev. Astron. Astrophys. **44**, 507 (2006).

[402] K. Z. Stanek et al., Acta Astron. **56**, 333 (2006), astro-ph/0604113.

[403] N. Langer, M. F. El Eid, and I. Baraffe, A&A **224**, L17 (1989).

[404] B. Paczynski, Astrophys. J. Lett.**494**, L45 (1998), arXiv:astro-ph/9710086.

[405] L. Dessart et al., Monthly Notices of the Royal Astronomical Society , no (2011).

[406] J. S. Vink and A. de Koter, A&A **442**, 587 (2005), arXiv:astro-ph/0507352.

[407] S. E. Woosley and A. Heger, Astrophys. J.**637**, 914 (2006).

[408] N. Smith, W. Li, A. V. Filippenko, and R. Chornock, Phys. Rev. D**412**, 1522 (2011).

[409] R. Blandford and C. McKee, Phys.Fluids **19**, 1130 (1976).

[410] R. Sari and T. Piran, Astrophys.J. **455**, L143 (1995), astro-ph/9508081.

[411] M. J. Rees and P. Mészáros, Astrophys. J.**628**, 847 (2005), arXiv:astro-ph/0412702.

[412] P. Mészáros and M. J. Rees, Astrophys. J. Lett.**733**, L40 (2011), 1104.5025.

[413] P. Mészáros and M. J. Rees, Astrophys. J. Lett.**556**, L37 (2001), arXiv:astro-ph/0104402.

[414] K. Ioka, S. Kobayashi, and B. Zhang, Astrophys. J.**631**, 429 (2005), arXiv:astro-ph/0409376.

[415] E. Waxman and J. N. Bahcall, Astrophys.J. **541**, 707 (2000), hep-ph/9909286.

[416] S. Toscano, Nuclear Instruments and Methods in Physics Research Section A: Accelerators, Spectrometers, Detectors and Associated Equipment , (2012).

[417] A. C. Searle, P. J. Sutton, and M. Tinto, Classical Quantum Gravity **26**, 155017 (2009).

[418] P. J. Sutton et al., New Journal of Physics **12**, 053034 (2010), 0908.3665.

[419] S. Klimenko, I. Yakushin, A. Mercer, and G. Mitselmakher, Classical Quantum Gravity **25**, 114029 (2008).

[420] R. Abbasi et al., Astrophys. J. Lett. **701**, L47 (2009), 0905.2253.

[421] E. S. Phinney, Astrophys. J. Lett. **380**, L17 (1991).

[422] D. J. White, E. J. Daw, and V. S. Dhillon, Classical and Quantum Gravity **28**, 085016 (2011), 1103.0695.

[423] J. A. de Freitas Pacheco and et al., Int. J. Mod. Phys. D **15**, 235 (2006), arXiv:astro-ph/0510727.

[424] R. O'Shaughnessy, V. Kalogera, and K. Belczynski, Astrophys. J.**716**, 615 (2010), 0908.3635.

[425] R. K. Kopparapu et al., Astrophys. J. **675**, 1459 (2008), 0706.1283.

[426] J. Braun et al., Astropart. Phys. **33**, 175 (2010), 0912.1572.

[427] B. Abbott et al., Phys. Rev. D **76**, 062003 (2007), arXiv:astro-ph/0703419.

[428] LIGO Scientific Collaboration, LIGO internal document T1000251 (2010).

[429] K. Kuroda and the LCGT Collaboration, Classical Quantum Gravity **27**, 084004 (2010).

[430] A. Burrows, E. Livne, L. Dessart, C. D. Ott, and J. Murphy, Astrophys. J. **655**, 416 (2007), arXiv:astro-ph/0610175.

[431] C. D. Ott et al., Phys. Rev. Lett. **106**, 161103 (2011), 1012.1853.

[432] R. Abbasi et al. (IceCube Collaboration), Astrophys. J. Lett. **701**, L47 (2009).

Appendix A

Glossary

1PPS 1 pulse per second.

ADC analog-to-digital converter.

AMON Astrophysical Multimessenger Observatory Network.

Antares high energy neutrino observatory, located at in the Mediterranean sea South of France.

AXP anomalous X-ray pulsars.

BATSE Burst and Transient Source Experiment. A gamma ray burst telescope on the Compton Gamma Ray Observatory (CGRO) satellite.

BH black hole.

CCSN core-collapse supernova.

CWb Coherent Waveburst - a gravitational wave search algorithm.

Einstein Telescope Planned third generation, earth-based gravitational wave telescope with projected sensitivity of $\sim 10\times$ that of advanced detectors.

EM electromagnetic.

EoS equation of state.

FAR false alarm rate.

Fermi gamma ray burst telescope on a satellite. Includes the Fermi Gamma-ray Burst Monitor (GBM) and LAT detectors.

FPGA Field Programmable Gate Array.

GEO 600-m graviational wave detector near Sarstedt, Germany.

GRB gamma ray burst.

GW gravitational wave.

GWGC Gravitational Wave Galaxy Catalog.

HEN high energy neutrino.

HL high luminosity [GRB].

HMNS hypermassive neutron star.

IceCube cubic-kilometer high energy neutrino observatory, located at the South Pole.

IRIG-B Inter-range Instrumentation Group B.

KAGRA Kamioka Gravitational-wave Detector (formerly Large-scale Cryogenic Gravitational-wave Telescope;LCGT).

LL low luminosity [GRB].

LAT Large Area Telescope. Detector on the Fermi satellite, sensitive to very high energy photons.

LIGO Laser Interferometer Gravitational-wave Observatory.

LMXB Low-Mass X-ray Binary.

M31 Andromeda galaxy.

MWE Milky Way equivalent (e.g., in blue luminosity).

NS neutron star.

OCXO Oven Controlled Crystal Oscillator.

QPO quasi-periodic oscillation.

PDF probability density function.

PLL phase locked loop.

PMT photomultiplier tube.

PNS protoneutron star.

PP Papaloizou-Pringle [instability].

RS422 technical standard for balanced voltage digital interface circuit.

S5/S6 official scientific data-taking periods of the LIGO observatories.

SGR soft gamma repeater.

SN supernova.

SNEWS Supernova Early Warning System.

SNR signal-to-noise ratio.

UTC Coordinated Universal Time (/Temps Universel Coordonné).

VCXO Voltage Controlled Crystal Oscillator.

Virgo 3-km name of gravitational wave detector, located in Cascina, Italy.

VSR1,2,3 official scientific data-taking periods of the Virgo observatory.

WR Wolf-Rayet [star].

XO Chrystal Oscillator.

ZAMS zero-age main sequence.